Seed-Mediated Growth of Anisotropic Au Nanostructures: Mechanistic Insights and Application Possibilities

A Thesis

Submitted in Partial Fulfillment of the Requirements

for the Degree of

Doctor of Philosophy

by

Debashree Roy

ID: 20173498

INDIAN INSTITUTE OF SCIENCE EDUCATION AND RESEARCH, PUNE

2021

Dedicated to

My Parents and Sister

भारतीय विज्ञान शिक्षा एवं अनुसंधान संस्थान पुणे
INDIAN INSTITUTE OF SCIENCE EDUCATION AND RESEARCH PUNE
डॉ. होमी भाभा मार्ग, पुणे 411008, महाराष्ट्र, भारत | Dr. Homi Bhabha Road, Pune 411008, Maharashtra, India
T +91 20 2590 8001 W www.iiserpune.ac.in
IISER PUNE

CERTIFICATE

Certified that the work incorporated in the thesis entitled "***Seed-Mediated Growth of Anisotropic Au Nanostructures: Mechanistic Insights and Application Possibilities***" submitted by ***Ms. Debashree Roy*** was carried out by the candidate, under my supervision. The work presented here or any part of it has not been included in any other thesis submitted previously for the award of any degree or diploma from any other university or institution.

Date: 6th Oct, 2021

Dr. Nirmalya Ballav
(Research Supervisor)

भारतीय विज्ञान शिक्षा एवं अनुसंधान संस्थान, पुणे
INDIAN INSTITUTE OF SCIENCE EDUCATION AND RESEARCH (IISER), PUNE
(An Autonomous Institution, Ministry of Human Resource Development, Govt. of India)

Date: 06-October-2021

Declaration

I ***Ms. Debashree Roy*** declare that, this written submission represents my ideas in my own words and where others' ideas have been included; I have adequately cited and referenced the original sources. I also declare that I have adhered to all principles of academic honesty and integrity and have not misrepresented or fabricated or falsified any idea/data/fact/source in my submission. I understand that violation of the above will be the cause for disciplinary action by the Institute and can also evoke penal action from the sources which have thus not been properly cited or from whom proper permission has not been taken when needed.

The work reported in this thesis is the original work done by me under the guidance of ***Dr. Nirmalya Ballav.***

Ms. Debashree Roy
(ID: 20173498)

nballav@iiserpune.ac.in Tel: +91 (020) 2590 8215 www.iiserpune.ac.in

Acknowledgment

I would take this opportunity to convey my deepest gratitude to my supervisor Dr. Nirmalya Ballav for the support, encouragement and unwavering faith that he has showered me with in the last five years. His mentoring has allowed me to grow into an independent researcher, pushing me beyond my limits so that I could excel in my work. His eye for detail, over-optimism and the ability to look beyond the ordinary is something that I hope to imbibe. I am also thankful to him for believing in me even when I did not have belief in myself.

I am also grateful to my Research Advisory Committee (RAC) members Dr. Pramod Pillai (IISER Pune) and Dr. Sreekumar Kurungot (NCL Pune) for their invaluable suggestions during the RAC meetings, and opening their doors to me for their instrumentation facilities, which not only improved my work but added new dimensions to them. I would also like to thank my collaborators, Dr. Shalini Tripathi for the extensive TEM analysis which constitutes a significant part of my thesis and reaching out to me beyond academics, Dr. Pranav K. Gangadharan for the electrochemical measurements, Prof. Ping Bai and his student Dr. Yi Xu for the theoretical calculations involved in one of the chapters.

I would like to thank the past and present Directors of IISER Pune for providing a research facility which is arguably among the best in the country. I also extend my gratefulness to the former and present Chair Chemistry and all the faculty members in the department.

I would like to acknowledge Mr. Anil Prathashetti, Mr. Yathish T. S., Mr. Prashant Badgujar, Mr. Sudhir Lone, Mr. Mahesh Jadhav, Mr. Sandeep Kanade, Mrs. Megha Paygude, Mr. Nilesh Dumbare, and Mr. Parveen Nasa, for technical support. I would like to thank Mr. Mayuresh Kulkarni, Mr. Sanjay Meena, Mr. Ganesh Dimbar, Mr. Prabhakar Anagare, Mr. Tushar Kurulkar, and Mrs Sayali Damle for administrative support.

I have been extremely fortunate to have interacted with the interesting bunch of people comprising of the former as well the current lab-members at Interfacial Materials Chemistry (Dr. Barun Dhara, Dr. Ranguwar Rajendra, Dr. Plawan K. Jha, Dr. Shammi Rana, Dr. Kriti Gupta, Vikash, Anupam, Dr. Syed, Ashwini, Pranay, Pooja, Manish, Sujit, Jai, Gopi, Ishan, Aswani, Nahid, Umashis, Vijay, Ajay and Sauvik). It was a privilege to have worked and learnt a great deal from all my seniors at lab: Dr. Barun Dhara and his never-ending enthusiasm and curiosity towards science, Dr. Plawan K. Jha for keeping the calm in the face of a storm and immaculate attention to detail, and Dr. Shammi Rana for showing how to make jugaad work in Indian research scene. I would forever be indebted to Dr. Ranguwar Rajendra for the taking

me under his wings in the initial phase of my journey and the endless scientific debates which fostered my understanding. I would like to express my admiration and appreciation for Dr. Kriti Gupta, my contemporary at the lab, for being an excellent team person and I could not have asked for a better lab-"mate" to have shared most of my PhD journey with. From her I learnt how to conduct oneself professionally and how to make the best of limited resources if you have the willingness to. I would like to mention that the last lap of my PhD journey has been made memorable, thanks to my juniors Pooja and Pranay who made the mundane interesting with their companionship. I would also like to thank Vikash and Anupam for showing how to keep the atmosphere at lab fun while working hard for your goals. Special mention to the lab trips which rejuvenated our minds and strengthened the inter-personal bonds.

The PhD journey at IISER Pune would have been incomplete without the overwhelming number of people who have become family over the years. Special mention to Kingshuk (for always having my back), Shabnum (for being a huge support system), Sumanta (for bearing with me through thick and thin), and Tariq (for being ever so patient while weighing gold salt for the entire course of my PhD) for nurturing and caring for me. It was a blessing to have friends like Aslam, Borish, Debashish, Jayashree, Neetu, Manzoor and Minhaj to whom I could turn to for any help or suggestion without any hesitation. I am also grateful to have crossed my paths with Sandip, Ankita, and Saikat for standing by me during my lows. I am also thankful to all those friends who despite chartering different paths have still managed to be an integral part of my PhD journey- Shampa, Samridhi, Mehali, Priyadarshini, Aritro, Anirban, Monisit, Sudeshna, Chandreyee, Sriparna, Manpreet, Antara, Debjani and Monalisa.

I am indebted to all my teachers who have directly or indirectly influenced my PhD journey, especially, S. K. C. Sir, R. D. Sir, H. S. Sir and Shobhen Sir. A special note of thanks to Sagar Da, whose journey has inspired me and who I look up to.

This acknowledgment would be incomplete without the mention of my parents and sister, who have been my strongest cheerleader and fiercest critic. I thank them for their perseverance into shaping me for who I am and never clipping my wings. A big shout out to my sister who knew I would pursue PhD, much before I embarked upon one. I also thank my extended family for being understanding of my PhD journey.

Last but not the least, I thank IISER Pune for timely disbursing the fellowship, DST and SERB for financial support.

Debashree Roy

Table of Contents

Table of Contents

A. Publications Included in Thesis

1. Facile Synthesis of Concave Cuboid Au NCs with Precisely Tunable Dimensions and Mechanistic Insight
   R. Rajendra[§], **D. Roy**[§], S. Tripathi, N. Ballav ([§] equal contribution)
   Langmuir **2019**, *35*, 9456

2. Controlling the Aspect Ratios of Au Nanocrystals with Ag^+ Addition Time in Seed-Mediated Synthesis: Implications for Surface-Enhanced Raman Scattering
   D. Roy, R. Rajendra, S. Tripathi, N. Ballav
   ACS Appl. Nano Mater. **2021**, *4*, 7426

3. Seed-Mediated Growth of Pt on High-Index Faceted Au Nanocrystals: The Ag Lining and Implications for Electro-Catalysis
   D. Roy, R. Rajendra, P. K.Gangadharan, A. Pandikassala, S. Kurungot, N. Ballav
   ACS Appl. Nano Mater. **2021**, *4*, 9155

4. Gold Nanoearbuds: Seed-Mediated Synthesis and the Emergence of Three Plasmonic Peaks
   D. Roy, Y. Xu, R. Rajendra, L. Wu, P. Bai, N Ballav
   J. Phys. Chem. Lett. **2020**, *11*, 3211

B. Other Publications

1. *In-situ* generated Mn_3O_4-reduced graphene oxide nanocomposite for oxygen reduction reaction and isolated reduced graphene oxide for supercapacitor applications
   P. K. Jha, V. Kashyap, K. Gupta, V. Kumar, A. K. Debnath, **D. Roy**, S. Rana, S. Kurungot, N. Ballav
   Carbon **2019**, *154*, 285

2. Achieving current rectification ratios ≥ 10^5 across thin films of coordination polymer
   A. Prasoon, B. Dhara, **D. Roy**, S. Rana, S. Bhand, N. Ballav
   Chem. Sci. **2019**, *10*, 10040

3. Direct Layer-by-Layer Growth of Crystalline Ag-TCNQ Thin Films on Functionalized Au Substrate: How Critical Is the pH of Ag(I) Solution?
   Lathika A. S., S. Rana, A. Prasoon, P. Sindhu, **D. Roy**, N. Ballav
   J. Phys. Chem. Lett. **2020**, *11*, 10548

NCs	Nanocrystals
SPR	Surface Plasmon Resonance
TSPR	Transverse Surface Plasmon Resonance
LSPR	Longitudinal Surface Plasmon Resonance
NR	Nanorod
CCB	Concave cuboid
CC	Concave cube
Oct	Octahedra
AH	Arrow-headed
ETHH	Elongated tetrahexahedra
THH	Tetrahexahedra
NEB	Nano-earbud
ND	Nano-dumbbell
HIF	High-index facet
1D	One Dimensional
3D	Three Dimensional
AR	Aspect ratio
SERS	Surface Enhanced Raman Scattering
NB	Nile Blue
EM	Electromagnetic
ORR	Oxygen Reduction Reaction
CV	Cyclic Voltammogram
LSV	Linear Sweep Voltammetry
ADT	Accelerated Durability Test
ECSA	Electrochemical active surface area
I_r	Ring current
I_d	Disc current
N	Collection efficiency
UV-vis	UV-visible spectroscopy
FE-SEM	Field emission Scanning Electron Microscopy

Glossary of Acronyms

TEM	Transmission Electron Microscopy
HRTEM	High Resolution Transmission Electron Microscopy
STEM	Scanning Transmission Electron Microscopy
SAED	Small Area Electron Diffraction
EDXS	Energy Dispersive X-ray Spectroscopy
PXRD	Powder X-Ray Diffraction
XPS	X-ray Photoelectron Spectroscopy
UPD	Underpotential deposition
GRR	Galvanic Replacement Reaction
CTAB	Cetyltrimethylammonium bromide
CTAC	Cetyltrimethylammonium chloride
CPC	Cetylpyridinium chloride
BDAC	Benzyldimethylhexadecylammonium chloride
AA	Ascorbic acid
TA	Tannic acid
FA	Formic acid
MQ	Millipore water
mg	Milligram
μg	Microgram
mM	Millimolar
^{o}C	Degree Celsius
min	Minutes
h	Hour

Introduction to Anisotropic Au Nanostructures

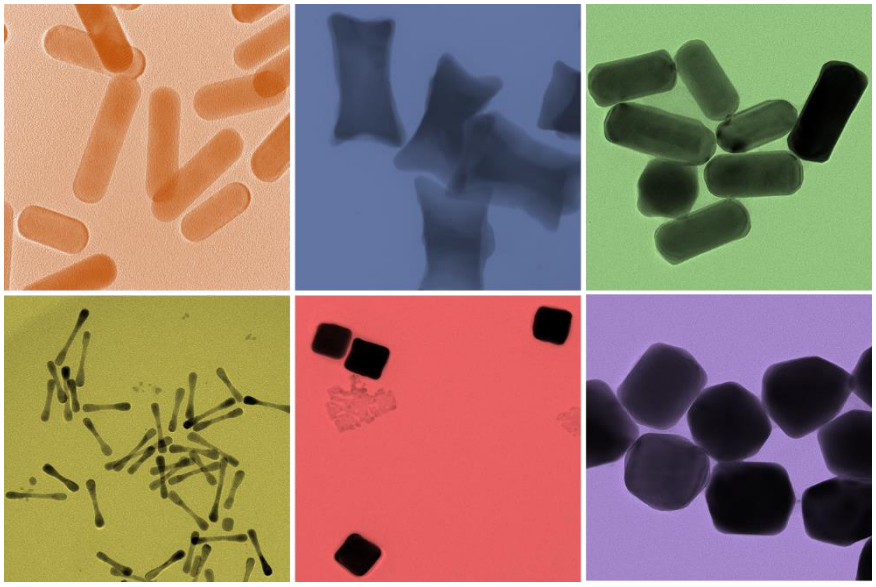

1.1 Introduction

Gold has attracted the attention of humankind since time immemorial and has often been equated as a symbol of wealth and power. This fascination has been primarily due to its brilliant lustre arising from the absence of stable oxides at ambient conditions resulting in exceptional chemical stability, and other properties like good conductor of heat and electricity, high ductile and tensile strength and inertness earning it the moniker of noble metal.[1] This has translated in their usage from art to jewellery to coinage. The appeal of gold does not end in its bulk state, but becomes even more interesting in its nanoscale regime where distinct optical, electronic, catalytic and electrocatalytic properties are exhibited. Although, the unique colours associated with finely divided gold were already known in ancient times, the last two decades have witnessed a renewed interest in the study of gold (Au NCs).[2-3] This emphasis has been mostly due to the shape and size dependent optical properties of Au NCs, originating due to a phenomenon known as surface plasmon resonance (SPR), and other structure-function relationships.[4] Among the numerous synthetic protocols available, the versatile seed-mediated growth method for the synthesis of anisotropic Au NCs is on the forefront.[5-6] A seed-mediated synthesis comprises of two steps, in which the seed particles grown in the first step are regrown in the second step in presence of metal precursors, surfactant, shape directing agent and a mild reducing agent.[7] The easy tailorability and high degree of shape control of Au NCs, a trademark of seed-mediated synthesis is usually achieved by manipulating external growth conditions like temperature or internal parameters which affect the nucleation and growth of the Au NCs. Mostly, two key chemical parameters, the Ag^+ and halide ions, the latter derived from quaternary ammonium halide based-surfactant, are known to play a crucial role in generating a myriad of anisotropic Au NCs. These two parameters have been isolated to have a better understanding of their role in the growth mechanism of various anisotropic Au NCs and forms the crux of this thesis. By doing so, we have also been able to introduce a new 1D Au nanostructure, Au nanoearbud, to the existing toolbox of anisotropic Au nanostructures.

1.2 Surface Plasmon Resonance

The optical properties of nanogold have been one of the primary reasons behind their popularity. They exhibit characteristic strong absorption band in the visible region, which is absent in its bulk counterpart.[2] The physical origin behind this light absorption lies in the

coherent oscillation of the conduction band electrons induced by the electromagnetic field of the interacting light. If collective oscillation is in resonance with the frequency of the incoming light, it gives rise to a phenomenon called surface plasmon resonance (SPR). The displacement of the electron cloud relative to the nuclei gives rise to a restoring force resulting in the oscillation of the electron cloud relative to the nuclear framework. The Coulomb attraction between electrons and nuclei results in the restoring force. The coherent collective electron oscillation observed most commonly is the dipole plasmon resonance, however, higher modes of plasmon excitations like quadrupole, sextupole or octupole resonances may also be observed.[8]

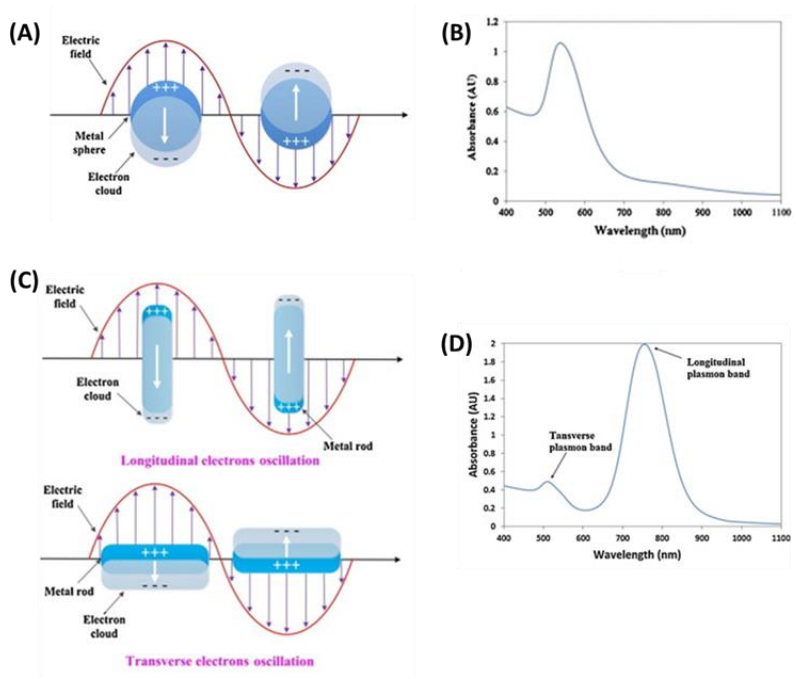

Figure 1.1: *(A) Schematic illustration of SPR excitation for spherical Au NCs and (B) their corresponding absorption spectrum; (C) Schematic illustration of SPR excitation for Au nanorods and (D) the absorption spectrum exhibiting two plasmon bands corresponding to the longitudinal and transverse electron oscillation. (adopted from Ref. 13 © Elsevier B. V.)*

The frequency of the oscillation depends on the density and the effective mass of electron as well as the shape and size of the NC and the dielectric medium surrounding it.[9-10] However, the size and shape of Au NCs exert marked effect on the width, position and number of SPR.[11-12] Thus, only one absorbance peak is discernible for spherical Au NCs which gets red-shifted on increasing the size. While two absorbance peaks are observed for Au nanorods (NRs),

corresponding to electron oscillation along the short (transverse SPR) and long (longitudinal SPR) axes of the NR appearing at lower and higher wavelength respectively.[13] The transverse SPR (TSPR) is mostly insensitive to changes in size and dielectric medium, whereas the position of longitudinal SPR (LSPR) can be easily tuned according to the length, aspect ratio and the surrounding refractive index.[10] A linear relationship was found to exist between the LSPR position and the mean aspect ratio of Au NRs. At a fixed NR aspect ratio, the LSPR showed a linear dependence to the medium dielectric constant.[14] Particularly, it has been studied that the refractive index sensitivity increased with increasing sharpness of the apexes of Au NCs. Au nanobipyramids, nanoprisms, concave cuboids have been found to exhibit three SPR peaks, the origin of which were different in all the cases.[10, 15-16] In general, reducing the symmetry of Au NCs is an effective way to modulate the number, position and intensity of SPR. Additionally, solvents and capping agents have also been realized to exert significant influence on the position of SPR for Au NCs.[17]

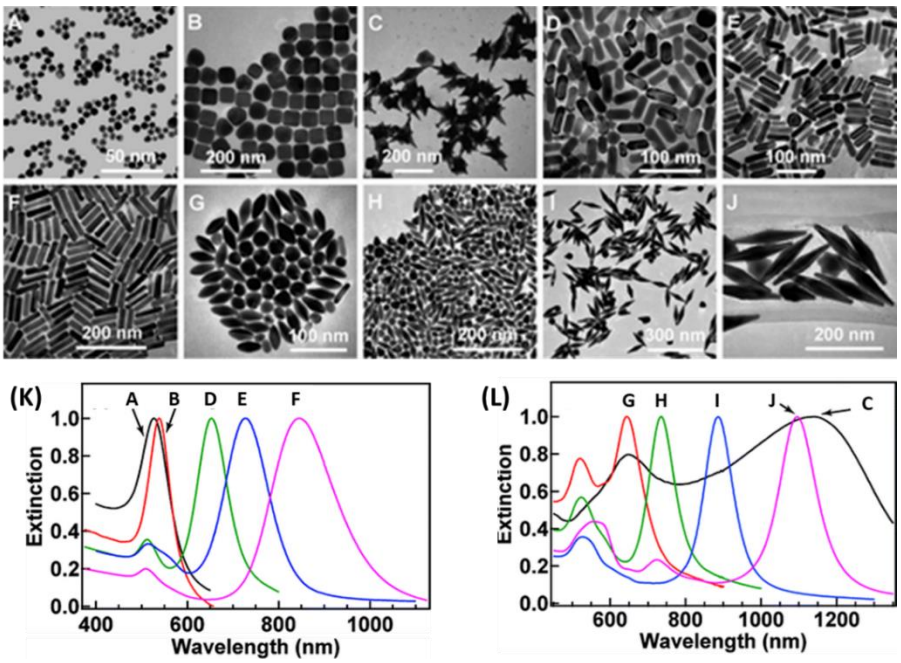

Figure 1.2: *TEM images of Au NCs of various shapes and sizes. (A) Nanospheres, (B) Nanocubes, (C) Nanobranches, (D) Nanorods (AR = 2.4), (E) Nanorods (AR = 3.4), (F) Nanorods (AR = 4.6), (G) Nanobipyramids (AR = 1.5), (H) Nanobipyramids (AR = 2.7), (I) Nanobipyramids (AR = 3.9), and (J) Nanobipyramids (AR = 4.7); (K) Normalized extinction spectra corresponding to A, B, D, E, F and (L) Normalized extinction spectra corresponding to C, G, H, I, J. (adopted from Ref. 10 © American Chemical Society)*

1.3 Anisotropic Au Nanostructures

Anisotropy in a material arises due to the difference in its properties along different directions and in the domain of Au NCs, broadly refers to morphological anisotropy, i.e., non-spherical NCs, or optical anisotropy, as in Au NCs exhibiting multiple SPR peaks.[18] Morphological anisotropy via solution-phase methods can be greatly enhanced in Au NCs by either introducing defects to the crystal structure of the seeds or inducing symmetry breaking event to the isotropic seeds; favouring a particular facet in the final Au nanostructure by using capping agent; and passivating the growth of selective facets by the use of certain additives; manipulating reaction conditions resulting in the interplay between kinetically controlled growth pathway and a thermodynamically controlled one.[19] Optical anisotropy, on the other hand, arises if the free electrons are polarized and distributed on the surface of Au NCs in more ways than one. These Au NCs have aroused the interest of scientists due to their morphological anisotropy dependent optical anisotropy making them promising candidates in avenues ranging from surface enhanced Raman scattering (SERS), optical sensing and imaging, photothermal therapy to photonics, giving rise to extensive research to develop chemical methods for preparing monodispersed Au NCs in high yield.[20] This has resulted in a library of anisotropic Au NCs exhibiting tunable SPR peaks.

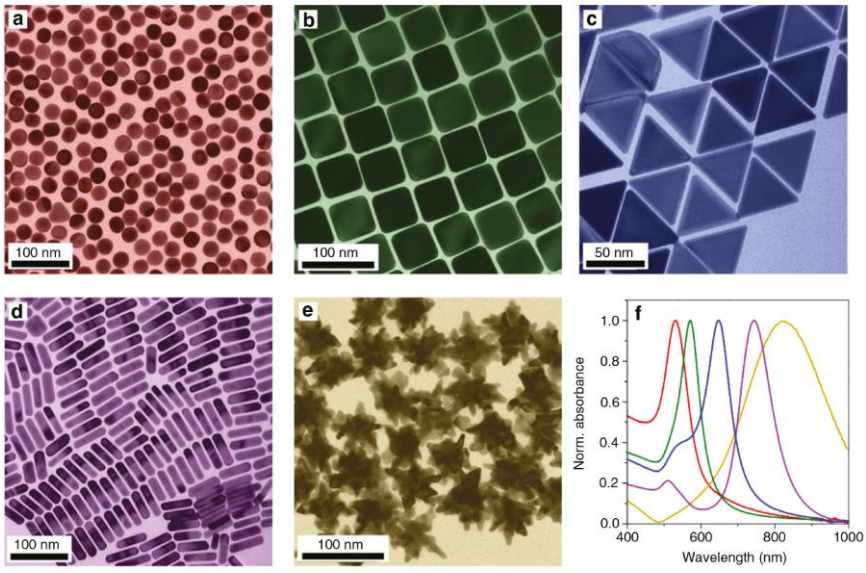

Figure 1.3: *Coloured TEM images of various anisotropic Au NCs: (a) nanospheres; (b) nanocubes; (c) nanotriangles; (d) nanorods; (e) nanobranches. (f) Corresponding UV-vis*

spectra exhibiting the shape dependent optical properties. (adopted from Ref. 20 © 2018 IUPAC & De Gruyter)

1.4 Seed-Mediated Growth Method

Achieving control over the synthesis of gold nanocrystals to generate anisotropic Au NCs has attracted a great deal of attention from the scientific community in recent years. In this regard, seed-mediated growth has been acknowledged as a powerful and versatile tool for the synthesis of colloidal metal nanocrystals.[5-6, 21] The considerable appeal of this approach mainly originates from the overwhelming extent of mastery one can wield over the size, shape, composition, and structure of nanocrystals.

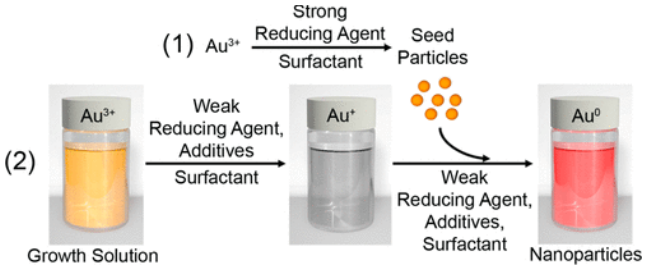

Figure 1.4: *Schematic illustration of seed-mediated method to generate Au nanoparticles. (adopted from Ref. 7 © American Chemical Society)*

Traditional colloidal synthesis of metal NCs comprises of a one-step synthesis, where simultaneous nucleation and growth takes place. One of the major disadvantages associated with this method is the lack of control over the size, shape, monodispersity and internal structure of the resultant NCs. Seed-mediated synthesis offers a way to alleviate this problem. The seed-mediated synthesis, a two-step method devised mainly to decouple nucleation from crystal growth, was first developed in a pioneering work by Murphy and co-workers for the generation of Au nanorods (NRs).[22] Later in another seminal work by El-Sayed, citrate was replaced with cetyltrimethylammonium bromide (CTAB) as a capping agent and $AgNO_3$ was introduced as a shape directing agent, resulting in almost 100% yield of Au NRs.[23] The seed-mediated method follows the heterogeneous nucleation process, where the nucleation process and the subsequent growth of Au NCs are delineated as two distinct synthetic steps. In the first step, i.e., the seed synthesis step, rapid reduction of Au^{3+} to Au^0 by strong reducing agent like $NaBH_4$ takes place in presence of a capping agent to generate highly monodispersed spherical Au NPs in the size range of 3-7 nm.[7] This step remains mostly similar for all the reported seed-

mediated methods. In the subsequent step known as the particle growth step, the pre-formed seed particles are introduced to the growth solution consisting of gold salt precursor, capping agent/surfactant, shape directing additive and a mild reducing agent. The choice of a mild reducing agent in this step is two-fold; it prevents further nucleation by enabling reduction of Au^{3+} to Au^{+} only, and promotes the deposition of Au^{0} atoms on the pre-existing seeds, in addition to slowing the particle growth to allow the shape control of the Au NCs. This makes the particle growth step much slower than the seed formation step.[24] The activation energy required for the reduction of Au on the pre-existing seeds being substantially reduced than that required for the homogeneous nucleation of seed particles in solution, autocatalytic growth of Au atoms on the pre-formed seeds is allowed. The use of $NaBH_4$, on the other hand, in the second step would further give rise to small seed particles instead of the formation of larger anisotropic NCs. The seed-mediated synthesis presents a series of variables, predominant among which are amounts of $AgNO_3$, type of surfactant, reaction temperature and pH, amount of mild reducing agent as well as the ratio between some key chemical parameters.[25] While having such an overwhelming number of parameters may result in complexities given their inter-dependence on one another, isolating them also paves the way for better insight into growth mechanisms. The underlying mechanisms governing the growth pathways in a seed-mediated synthesis- the kinetically controlled and selective surface passivated pathways are directed predominantly by Ag^{+} and halide ions and will be discussed at length in subsequent sections.[7] Rational design and judicious maneuvering of growth conditions integral to seed-mediated synthesis offer extensive promise for the advancement of understanding and designing of anisotropic Au NCs and opening the door to a world of possibilities.

1.5 Role of Seed

Achieving control over the crystallinity of seeds is essential for the generation of anisotropic Au NCs in high yield. A seed is a nucleus which has grown past a critical size such that its internal structure is unperturbed by thermal fluctuations.[26] Of the numerous crystalline forms in which Au NC seeds, with face-centered lattice, can exist, the most prevalent are single crystalline and singly, doubly, penta- and multiply twinned NCs.[5] Experimental studies have shown that the internal structure of the seed is regulated by both thermodynamic as well as kinetic parameters. In a thermodynamically controlled reaction condition, the most stable product will be the those which can reduce the total interfacial free energy. In this context,

single crystalline seeds will be produced in major proportion along with singly and multiply twinned seeds comprising the minor fraction. However, for seeds consisting of internal crystal defects, the strain energy increases with an increase in the size of the seed. It is more prominent for multiply twinned seeds, which are favoured at smaller sizes by thermodynamics. As such, a slower generation of atoms increases the proportion of multiply twinned seeds over the single crystalline seeds as their small sizes can be maintained for longer time periods. When the generation of atoms is fast (in presence of a strong reductant), single-crystal seed formation will dominate.[26] Depending on the reaction conditions employed, the internal crystal structure may or may not be preserved in the final morphology. Likewise, various shapes bound by different facets may evolve from seeds exhibiting the same internal crystal habit just like different morphology of Au NCs bound by different facets may result from subjecting seeds, differing in their crystal habits, to the same growth conditions.[27] The difference in internal crystal structure notwithstanding, several studies have shown that the yield of Au NRs decreases with the increase in the size of the respective seeds.[28-29] Additionally, the age of CTAB-capped seeds has been realized to be just as crucial in exerting tight control over the monodispersity of the resulting Au NRs. Aging the seeds between one to ten minutes was found to result in single crystalline Au NRs with highest shape yield.[30] It is common wisdom that while the use of citrate as a capping agent gives rise to multiply twinned seed particles, the use of CTAB results in the generation of single crystalline seed particles.[7] This proportion of citrate capped multiply twinned seed particles have in a recent study been increased by mild thermal treatment.[31] Thus, improving the yield of anisotropic twinned Au NCs such as penta-twinned Au NRs, decahedra, bipyramids and nanostars. On the contrary, oxidative etching has been used to remove seeds containing twin defects to increase the relative proportion of single-crystalline seeds. As such, the internal structure, which remains conserved during the growth stages of the Au NCs, is defined at the initial stages of seed synthesis and the surface structure becomes more pronounced during the final stages of seed synthesis.[26]

Symmetry breaking is another aspect in the synthesis of anisotropic Au NCs where the role of seed particles is crucial. Extensive studies have been carried out to study how isotropic seeds breaks its symmetry to grow anisotropically.[32-35] For penta-twinned nanorods, the inherent geometry associated with the penta-twinned seeds allows the growth via selective surface passivation of facets.[32] In contrast, for the single crystalline seed particles, the symmetry

breaking occurs in the size regime ~4-6 nm with the creation of truncations which mark the beginning of anisotropic growth into NRs. Seed particles grown beyond 6 nm in the absence of $AgNO_3$ has greater tendency of developing into twinned particles, no longer capable of generating NRs under the conditions employed.[33] The symmetry breaking is not just limited to small isotropic seed particles, but has been extended to rhombic dodecahedron Au NCs used as seeds and possessing O_h symmetry. They transform to tetrahedra Au NCs with reduced T_d symmetry via the kinetically driven growth process where tip/edge deposition is preferred leading to initial loss of inversion symmetry.[36]

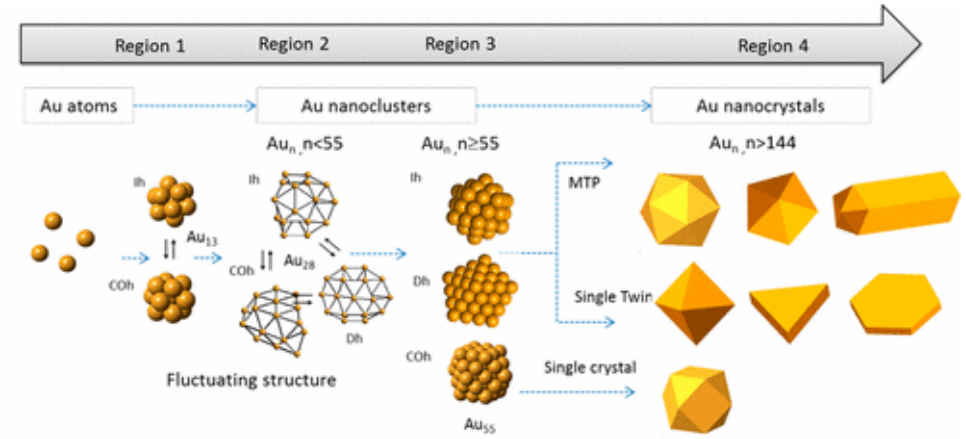

Figure 1.5: *Schematic illustrating the growth mechanism of seeds and how their internal crystal structure impacts the growth of Au NCs. (adopted from Ref. 30 © American Chemical Society)*

1.6 Role of Halide

The advent of aqueous seed-mediated synthesis as a powerful tool to achieve shape-controlled synthesis of anisotropic Au NCs has initiated studies on the role of halide anions in guiding the morphology. Quaternary ammonium halide-based surfactants, the major source of the halide anion, have been vital to the generation of anisotropic Au NCs. In particular, bromide-based surfactant, CTAB, has been found to be indispensable when it comes to the generation of monodisperse Au NRs. Various mechanisms have been put forward, ranging from soft template method to face-selective capping agent,[24, 37] to explain how bromide aids Au NR formation. However, none of them have been able to fully elucidate the picture. Furthermore, by changing the halide counter-ion in an otherwise identical reaction condition, a host of anisotropic Au NCs have been obtained. The deliberate introduction of KI as the source of iodide resulted in

the formation of prism and plate-like morphology.[38-39] In presence of CTAC however, Au NCs enclosed by high-index facets could be generated. This points at the crucial role played by halides in controlling the shape of Au NCs and their judicious choice can help in rational designing of anisotropic Au NCs.

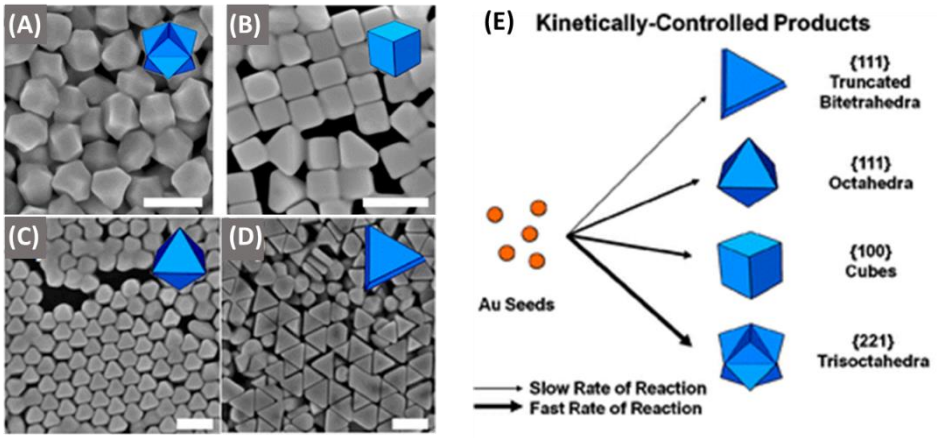

Figure 1.6: *SEM images of reaction products from growth solutions containing (A)50 mM CTA-Cl only; (B) 50 mM CTA-Cl and 5.0 mM NaBr; (C) 50 mM CTA-Cl and 10.0 μM NaI; and (D) 50 mM CTA-Cl and 75.0 μM NaI, resulting in the formation of high-index faceted trisoctahedra,{100-faceted cubes, {111}-faceted octahedra, and {111}-faceted truncated bitetrahedra respectively. Scale bar is 200 nm for all. (E) Scheme illustrating how halides in in the absence of silver ions lead to the formation of kinetically controlled products. (adopted from Ref. 40 © American Chemical Society)*

In the absence of halides, the order of specific surface free energies for Au increases as $\gamma_{(111)} = 3.36(\varepsilon/a^2) < \gamma_{(100)}\ 4(\varepsilon/a^2) < \gamma_{(110)}\ 4.24(\varepsilon/a^2)$, where ε is the bond strength and a is the lattice constant.[26] This however gets effectively modified in presence of halides due to their preference for certain facets, retarding the deposition of atoms on them, thereby preserving those facets in the final morphology. It has also been proposed that the presence of halides strongly influences the reduction potential of Au^+ and in turn the reduction rate. The reduction potential of Au^+ reduces in the order of $AuCl_2^-$ (1.154 V) > $AuBr_2^-$ (0.960 V) > AuI_2^- (0.578 V),[40] i.e., on increasing the size of the halide, it will increasingly become difficult to reduce Au-halide complexes. Thus, the progressively retarded rate of Au atom generation will result in Au NCs bound by low-energy surfaces, accounting for the formation of prism/plate-like morphology bound by {111} facets. In addition, the adsorption strength of the halides to Au

surface follows the order $Cl^- < Br^- < I^-$.[41] Thus, the desorption of halides from the Au surface will be more difficult for halides exhibiting a greater affinity towards Au surface, thereby lowering the Au surface area available to promote the reduction of Au^+. The reduction rate of Au^+ further depends on the effective availability of Au^+ which decreases with the decrease in the solubility of the Au-halide complexes as $[AuCl_2]^- > [AuBr_2]^- > [AuI_2]^-$.[7] The decrease in the solubility of the Au-halide complexes results in the lowering of equilibrium concentration of Au^+ in solution and consequently the reduction rate of Au^+. The complete understanding of the role of halides is however challenging as it is mired in several interactions working in tandem in directing the shape-controlled synthesis of Au NCs. The most prominent among them is its synergistic interaction with Ag^+, discussed in the upcoming section.

1.7 Role of Silver

The seed-mediated synthesis of Au NCs is associated with a large number of variables. While on one hand it allows more control over the reaction kinetics and hence the final morphology of the Au NCs, on the other hand it impedes the mechanistic study of the Au NCs due to the synergy or competition between various components. With the advent of Ag-assisted seed-mediated growth of Au NRs, Ag^+ has been widely employed as a shape directing agent in the seed-mediated synthesis of various anisotropic Au NCs.[23, 42-43] The introduction of Ag^+ to the growth of Au NR improved the yield and was later used to tune the aspect ratio of Au NRs.[33] The initial understanding of the role of Ag^+ was speculative, wherein $AgBr_2^-$ instead of Br^- was proposed to selectively passivate Au surface. However, the chemical inertness of $AgBr_2^-$ when compared to Br^- and the small fraction of Ag^+ when compared to the Br^-, ruled out such possibility. A new mechanism, underpotential deposition (UPD) of Ag on Au surface, was introduced which involves the deposition of a metal (here Ag) sub-monolayer or monolayer onto a different metal (Au) surface at a potential significantly less negative than for bulk deposition. Furthermore, theoretical calculations showed that work function difference between the adsorbate and adsorbent directed the underpotential shift. The work function of Ag being lower than Au by 0.5 eV, allows the UPD of Ag on Au surface. However, this value is not absolute and depends on the facet as observed from the work function differences of 0.57, 0.83, 0.85 eV between Au and Ag for their (111), (100) and (110) facets.[27] Thus, UPD of Ag on Au surface follows the order (110) > (100) > (111). Additionally, an UPD Ag atom on

(110) facet is stabilized by five nearest neighbours compared to four and three on (100) and (111) facets respectively.[44]

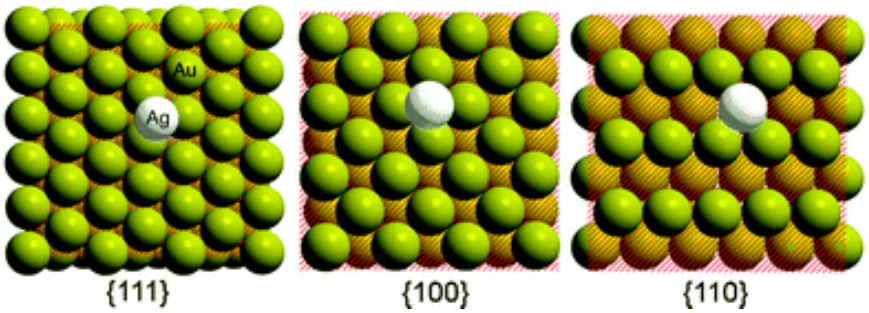

Figure 1.7: *Schematic illustration of binding of Ag onto different Au surfaces. (adopted from Ref. 44 © The Royal Society of Chemistry)*

This also explains the existence of the higher energy {110}facets in Au NRs whereby the compact Ag UPD monolayer restricts it from further growth. However, this restriction does not hold in those cases where the fraction of Ag^+ employed is quite high, leading to higher Ag coverage without any discrimination toward any particular facet.[45] UPD is also affected by the availability of Ag^+ in presence of halide ions. As the solubility of the Ag-X (X = Cl, Br, I) complexes decreases with increasing size of halide (k_{sp}(AgCl) ~ 10^{-10} > k_{sp}(AgBr) ~ 10^{-13} > k_{sp}(AgI) ~ 10^{-16} >), the availability of Ag^+ for reduction is decreased.[46] This reduces the rate of Ag deposition leading to lower Ag coverage on the Au surface, stabilizing the less open facets. Furthermore, the halide ions impact the binding of the Ag UPD layer to varying degrees. On account of similar binding strength of Cl^- to Ag and Au surfaces, it does not compete significantly with Ag for Au surface resulting in a Ag UPD layer with enhanced stability. Under such circumstances, increasing the Ag^+ concentration leads to the stabilization of surfaces with more open structures enabling the formation of Au nanostructures bound by high-index facets. Alternatively, at higher concentrations of halides (Br^-, I^-), due to the stronger binding affinity of both Br^- and I^- towards Au surfaces, a competition ensues between the halides and the Ag for Au surfaces, destabilizing the Ag UPD layer and blocking the Ag deposition. In presence of trace amounts of Br^- and I^-, although the Ag UPD layer is destabilized, Au NCs bound by more open facets can be generated due to higher Ag coverage via UPD at relatively lower Ag^+ concentration.[7] The co-reduction of Au^+ and Ag^+ may also take place to electrolessly deposit Ag-Au alloy on the Au NR seeds to give rise to Au-Ag electroless co-deposition, which

undergoes a pathway switch between Ag UPD arising due to the interplay of Ag^+, surfactants and reducing agent.[43]

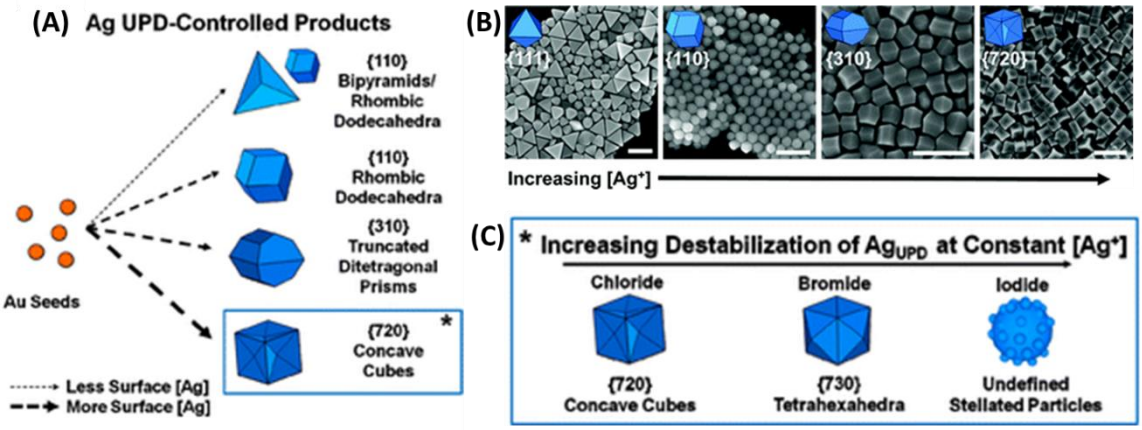

Figure 1.8: *(A) Schematic illustrating Ag UPD-controlled products where the interactions of silver with the particle surface dictates product shape; (B) SEM images of (left to right) octahedra, rhombic dodecahedra, truncated ditetragonal prisms, and concave cubes obtained by increasing the concentration of Ag^+ in reaction solution; (C) Effect of varying the stability of the Ag UPD layer with high concentrations of chloride, bromide, or iodide in the growth solution, yielding concave cubes, tetrahexahedra, and stellated particles, respectively. (adopted from Ref. 40 & 42 © American Chemical Society)*

While the UPD mechanism accounts for the final morphology, it could not account why an isotropic cuboctahedral seed particle undergoes symmetry breaking in presence of Ag^+ to induce anisotropic growth to a NR. It was proposed that there is an initial formation of new {011} surfaces formed stochastically as truncations, to remove high-energy edge atoms at the intersection of existing {111} facets, stabilized by Ag deposition and thus preserving the facet in the nascent NRs, signally the symmetry breaking event.[34] Furthermore, the $[HAuCl_4]$:$[AgNO_3]$ ratio coupled with the reduction potential of the system dictates the deposition of Ag on the atomically more open surfaces instead of the lower-index facets in existence. The $[HAuCl_4]$:$[AgNO_3]$ ratio also decides the size at which symmetry breaking can take place which in turn determines the final width and aspect ratio of the Au NR.[33] With further progress in reaction, Ag surface coverage is diminished due to its diffusion into the layers below the surface of NR.[47] This also slows the growth rate of the length of the NR which depends on the amount of Ag present on surface. However, if allowed to grow for extended

time period, a reduction in the Au NR aspect ratio indicates a lowered control of Ag on the aspect ratio thereby emphasizing the crucial role exerted in the initial stages of the reaction.[48]

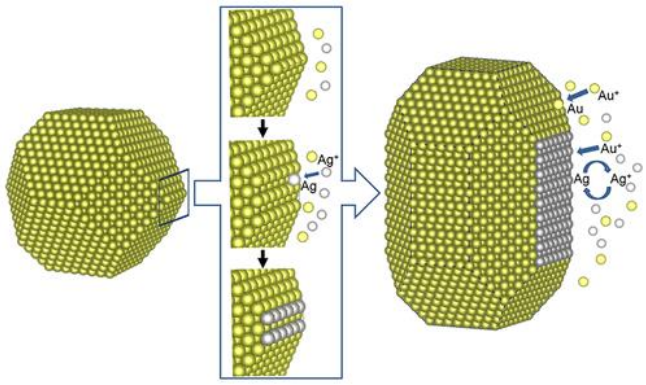

Figure 1.9: *Schematic illustrating the symmetry breaking event of symmetric cuboctahedral Au seeds: Formation of truncating surface and subsequent stabilization by Ag UPD. (adopted from Ref. 34 © American Chemical Society)*

1.8 Role of Reducing Agent

Understanding the role of key chemical parameters involved in the seed-mediated synthesis offers a route to rationally design Au NCs. To that effect, the role of reducing agent employed in a seed-mediated synthesis have also been studied by various research groups.[49] The two-step seed-mediated method involves the usage of two reducing agents: a strong reducing agent in the seed synthesis step and a mild reducing agent in the growth step. The use of $NaBH_4$ as the strong reducing agent in the first step is common across all aqueous seed-mediated methods. However, a variety of compounds have been exploited as the mild reducing agent. The reduction kinetics of the metal salt precursor can most easily be tailored with the choice of a reducing agent. While the reduction of Au^{3+} to Au^0 which takes place in the presence of $NaBH_4$ is a rapid process, ensuring seed particles are monodisperse and small, the reduction that takes place in the growth step in presence of a secondary mild reducing agent is slow allowing the shape control of Au NCs associated with the seed-mediated growth. By far, ascorbic acid (AA) has been the ubiquitous choice as the secondary reductant for synthesizing anisotropic Au NCs. It functions as a weak reducing agent under acidic conditions, reducing Au^{3+} to Au^+, followed by catalysing the conversion of Au^+ to Au^0 on the pre-formed seeds, thereby averting self-nucleation of the metal atoms to generate new seeds. The concentration of AA has also been modulated to generate Au NCs of varying morphology, where increasing its concentration has

been found to accelerate gold ion reduction and hence particle growth leading to the formation of kinetically more favoured particles bound by high energy surfaces.[50]

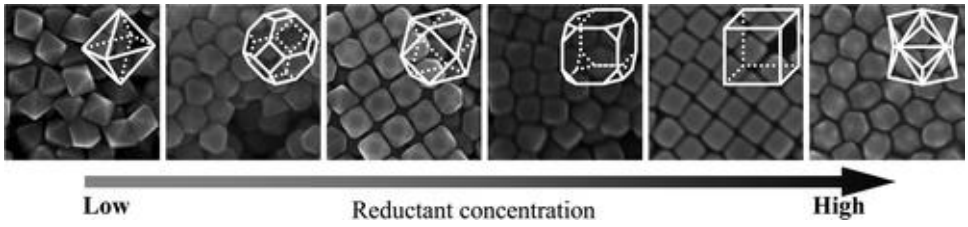

Figure 1.10: *SEM images of various polyhedral Au NCs: (a) octahedra; (b) truncated octahedra; (c) cuboctahedra; (d) truncated cube (e) cube and (f) trisoctahedra obtained by increasing the concentration of the reductant in the growth solution. (adopted from Ref. 50 © American Chemical Society)*

But this has not deterred researchers from exploring other compounds as possible alternatives to precisely control the reaction kinetics. Notable among them have been the use of aromatic alcohols like hydroquinone, catechol, resorcinol to generate Au NRs with LSPR tuned beyond 1200 nm or lengths tunable up to 1-3 μm.[51-52] Prereduction with curcumin and 5-bromosalicylic acid in the absence and presence of ascorbic acid respectively, has been carried out for the synthesis of Au NRs to investigate the formation and to improve the monodispersity and yield of gold reduction.[53-54] The efficacy of tannic acid (TA), a polyphenolic compound, as a milder alternative to ascorbic acid has not only been limited to the generation of Au NRs, but extended to other anisotropic Au NCs as well, demonstrating superior control over reaction kinetics.[55] The phenolic groups present in tannic acid undergo redox reactions to release electrons to reduce the metal ion and themselves oxidized to the quinone form.[56] The reducing ability of all these mild reducing agents can be easily modulated by adjusting the pH of the solution and a study has shown the generation of various penta-twinned Au NCs with tunable sizes simply by altering the initial pH of the system.[57]

$$C_6H_6O_6 + 2e^- + 2H^+ \longrightarrow C_6H_8O_6 \qquad (1)$$

$$E_h = E_0 + 0.05916/2 \{\log [C_6H_6O_6]/[C_6H_8O_6] - 2\ pH\} \qquad (2)$$

The Nernst equation derived from the half-cell equation of AA oxidation (Equation 2) consists of the pH term where E_0 refers to the standard reduction potential reaction of equation 1, and the actual half-cell reduction potential at a given reaction condition is E_h. It can therefore be

observed that the effect of pH of the reducing agent on E_h is more pronounced than its concentration. A higher pH value of the growth solution translates to a more negative reduction potential of the reducing agent and hence a more facile reduction reaction. Taken together, the reaction conditions such as solution pH and temperature are also of paramount importance in regulating the activity of the reducing agent and understanding their role in the chemical synthesis of Au NCs.

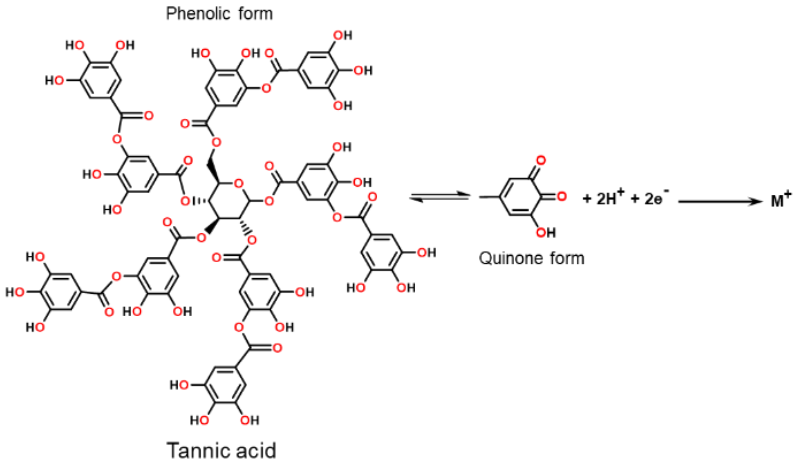

Figure 1.11: *Schematic outlining the reaction mechanism of tannic acid mediated reduction of metal salts.*

1.9 Application Possibilities

The ability to tailor the morphology of Au NCs has paved the way to not only tune their physicochemical properties, but also optimize them for a wide range of applications. The optical properties of Au NCs have been engineered due to their innate bio-inertness for various biomedical applications like sensing, drug delivery, imaging, cancer treatment and photodynamic therapy among the others.[1] The shape-controlled Au NCs have particularly attracted the attention of researchers to explore them towards catalytic and electrocatalytic applications as their bulk counterpart have been known for being an inert catalyst.[58] Better control over the shape dependent surface structures of Au NCs has also improved the understanding of the activity of the catalysts. Apart from the superiority of shapes enclosed with more corners and edges over simple structures towards catalysis, the facets enclosing the Au NCs have also been found to play a crucial role. Facet-dependent catalytic studies have further emphasized the rational engineering of Au surfaces towards heterogeneous catalysis.[59]

Au NCs bound by high-index facets have been realized to exhibit remarkable electrocatalytic behaviour in comparison to those Au NCs bound by low-index facets. In particular, the electro-oxidation of formic acid (FA), considered an important prototype reaction for small organic oxidation,[60] showed the superior performance of tetrahexahedra (THH) Au NCs over bulk gold and a (111) bound conventional polycrystalline Au electrode. The superiority was attributed to the enhanced adsorption, activation and oxidation of FA on the high density of under-coordinated surface atoms present in THH Au NCs.[61] Another prominent avenue where anisotropic Au NCs have found success due to their enhanced optical properties is surface enhanced Raman scattering (SERS). A vast majority of anisotropic Au NCs have been explored as possible substrates towards SERS with varying degrees of enhancement. Apart from the morphological parameters of NCs such as curved edges, protruded corners and highly reactive facets, other key factors that positively impact SERS performance include minimally damped plasmon oscillation and on-resonance conditions. In an electromagnetic mechanism, the enhancement factor can be simplified to approximate the fourth power of the local electromagnetic (EM) field enhancement at the surface of the NC. A modest enhancement by a factor 10 of the EM field can result in an increased intensity by 10^4.[62] In fact, Au concave cubes exhibiting red-shifted plasmon resonances in comparison to its non-concave counterpart are expected to show better SERS signals. Indeed, higher EM field enhancement was observed in those cases where the excitation wavelength and LSPR were in resonance with each other. Additionally, the more concave structures produced higher enhancements.[63] Thus, optimizing the properties of the SERS substrates (Au NCs in this case) holds promise for the use SERS technique as a detection tool for diverse analytes.

1.10 Objective of Thesis

In this thesis titled **"Seed-Mediated Growth of Anisotropic Au Nanostructures: Mechanistic Insights and Application Possibilities"**, two chemical parameters, quaternary ammonium halide-based surfactants and Ag^+, considered instrumental in the seed-mediated synthesis of Au nanostructures have been extensively studied to expand their understanding, offering new mechanistic insights into the growth of anisotropic Au NCs. Briefly, the role of the quaternary ammonium halide-based surfactants, the primary source of halide, during the growth of Au CCB NCs have been discussed at length wherein Cl^- ion has been found to regulate the formation of concave structure. Additionally, modification of the well-established

Au NR synthetic protocol by using quaternary ammonium chloride-based binary surfactant mixtures instead of CTAB, a bromide-based surfactant, led to the generation of a novel 1-D Au nanostructure, Au nano-earbud (NEB). As opposed to conventional wisdom, the chloride-based binary surfactant mixture could also generate Au NRs. Furthermore, investigation into the growth of both these anisotropic Au NCs (CCB and NEB) has shed light on their evolution mechanism. After studying the role of halide, the role of Ag has been explored for the first time in the growth of CCB Au NCs, from the perspective of time. The aspect ratios of CCB Au NCs have been modulated by adding same amount of Ag^+ but at different time intervals which could not be compensated by adding excess Ag^+. This brings to light the importance of Ag addition time in the generation of anisotropic Au NCs. These Au CCB NCs bound by high-index facets (HIFs) have further been subjected to Pt deposition in presence of Ag^+. By developing a fast and facile synthetic route, we were able to bypass the tediousness associated with the generation of Au@Pt nanostructures. An unusual behaviour of Ag^+, unlike those reported in literature, in directing the Pt deposition has been observed and duly investigated.

Au CCB NCs, by virtue of their sharp corners and edges and under-coordinated surface atoms, have been realized as excellent candidates as SERS substrates and electrocatalysts respectively. With selective Pt deposition on the edges and corners of Au CCB NCs, impressive electro-catalytic performance toward the oxygen reduction reaction was observed. Such performance at a relatively low Pt loading bypasses the need of monometallic Pt NCs. Additionally, we anticipate that Au NEB NCs with sub-100 nm dimension and SPR peak in the NIR-II region are promising for in-vivo biological application and detailed studies are highly desirable.

This thesis is further composed of the following chapters,

Chapter 2. Mechanistic Insight into the Evolution of Au Nanorod to Concave Cuboid Au NCs

In this chapter, the role of the cationic as well as the anionic counterpart of a quaternary ammonium halide surfactant which constitutes as a key chemical parameter in the seed-mediated synthesis of anisotropic gold nanocrystals (Au NCs) has been duly studied for the generation of concave cuboid (CCB) Au NCs. Insight into the growth mechanism in the transformation of Au nanorods (NRs) to CCB Au NCs, the latter belonging to the family of HIF NCs, has been performed. The Au CCB NCs were in turn exploited as electro-catalysts for the oxidation of formic acid due to the presence of under-coordinated surface atoms.

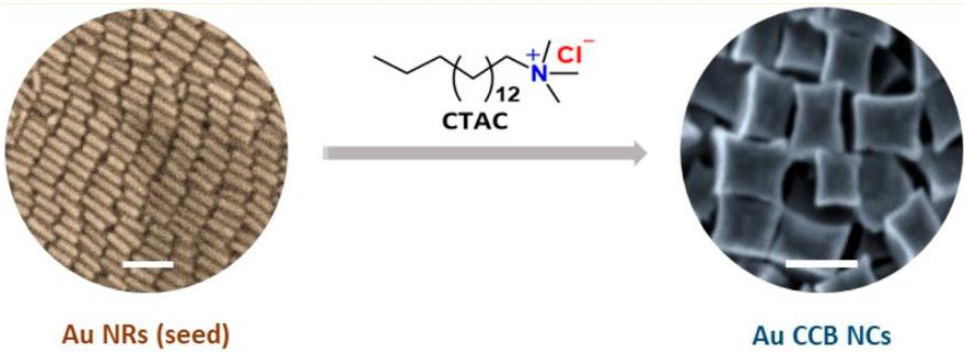

Publication from this chapter:

Facile Synthesis of Concave Cuboid Au NCs with Precisely Tunable Dimensions and Mechanistic Insight

R. Rajendra[§], **D. Roy**[§], S. Tripathi, N. Ballav ([§] equal contribution)

Langmuir **2019**, *35*, 9456

Chapter 3. Controlling the Aspect Ratios of Au NCs with Ag^+ Addition Time in Seed-Mediated Synthesis

In this chapter, the role of another key chemical parameter, $AgNO_3$, has been investigated from the perspective of time in the seed-mediated synthesis of Au CCB NCs. By doing so, we were able to generate CCB Au NCs with tunable aspect ratios (ARs). We further show that the addition time of Ag^+ is just as crucial as the concentration in regulating the AR of the final Au NCs and cannot be compensated by adding excess Ag^+ at a later reaction point. The findings were extended to another anisotropic Au NC system, elongated tetrahexahedra (ETHH) where similar observations were made, lending credibility to our earlier findings.

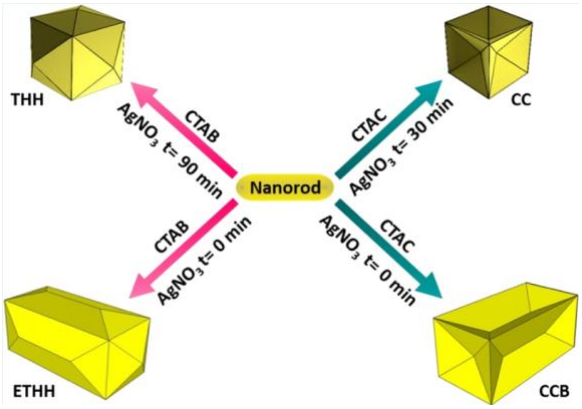

Publication from this chapter:

Controlling the Aspect Ratios of Au Nanocrystals with Ag^+ Addition Time in Seed-Mediated Synthesis: Implications for Surface-Enhanced Raman Scattering

D. Roy, R. Rajendra, S. Tripathi, N. Ballav

ACS Appl. Nano Mater. **2021**, *4*, 7426

Chapter 4. Wet-Chemical Deposition of Pt on Au NCs: The Ag Lining

In this chapter, a facile and robust wet-chemical method has been devised for the deposition of Pt within 7 minutes at 65 ºC onto CCB Au NCs. Ag^+ exhibited an unusual behaviour, wherein Pt deposition was retarded in the absence and in the presence of higher Ag^+ concentration. Analogous observations were also made for Pt deposition on ETHH Au NCs, another class of HIF Au NCs. The electro-catalytic behaviour of these HIF Au NCs with variable Pt loading towards oxygen reduction reaction (ORR) was studied where they showed impressive performance.

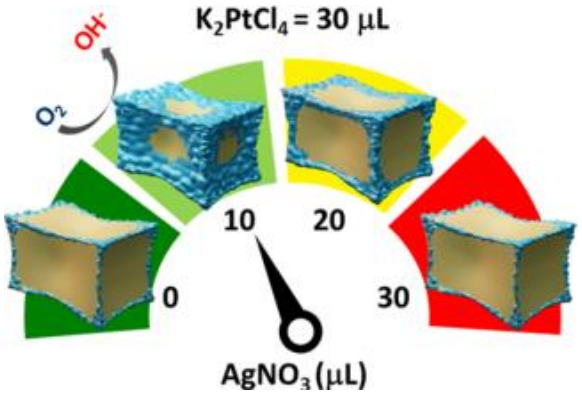

Publication from this chapter:

Seed-Mediated Growth of Pt on High-Index Faceted Au Nanocrystals: The Ag Lining and Implications for Electro-Catalysis

D. Roy, R. Rajendra, P. K.Gangadharan, A. Pandikassala, S. Kurungot, N. Ballav

ACS Appl. Nano Mater. **2021**, *4*, 9155

Chapter 5. Gold Nano-Earbuds: Seed-Mediated Synthesis and the Emergence of Three Plasmonic Peaks

In this chapter, by manipulating a chloride based binary surfactant mixture and modulating the $AgNO_3$ amount, we were able to introduce a new morphology to the existing library of anisotropic 1D Au nanostructures, Au nano-earbud (NEB). Au NEBs exhibit three plasmonic peaks, analysed theoretically where the new resonance peak was found to be a longitudinal sextupole mode, arising because of the bulbous ends of the NEB structure and intensified by the high AR. The longitudinal surface plasmon resonance (SPR) could be tuned beyond 1200 nm, while maintaining the dimension well below 100 nm, a challenging accomplishment in the realm of one-dimensional (1D) Au nanostructures.

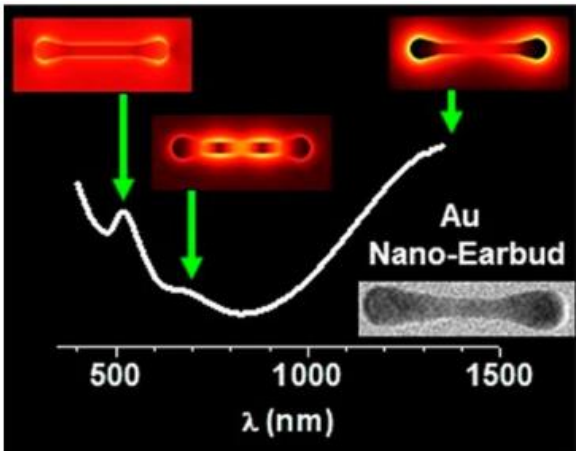

Publication from this chapter:

Gold Nanoearbuds: Seed-Mediated Synthesis and the Emergence of Three Plasmonic Peaks

D. Roy, Y. Xu, R. Rajendra, L. Wu, P. Bai, N Ballav

J. Phys. Chem. Lett. **2020**, *11*, 3211

1.11 References

1. Eustis, S.; El-Sayed, M. A., Why Gold Nanoparticles Are More Precious Than Pretty Gold: Noble Metal Surface Plasmon Resonance and Its Enhancement of the Radiative and Nonradiative Properties of Nanocrystals of Different Shapes. *Chem. Soc. Rev.* **2006**, *35*, 209-217.

2. Amendola, V.; Pilot, R.; Frasconi, M.; Marago, O. M.; Iatì, M. A., Surface Plasmon Resonance in Gold Nanoparticles: A Review. *J. Phys.: Condens. Matter* **2017**, *29*, 203002.

3. Daniel, M.-C.; Astruc, D., Gold Nanoparticles: Assembly, Supramolecular Chemistry, Quantum-Size-Related Properties, and Applications toward Biology, Catalysis, and Nanotechnology. *Chem. Rev.* **2004**, *104*, 293-346.

4. Li, N.; Zhao, P.; Astruc, D., Anisotropic Gold Nanoparticles: Synthesis, Properties, Applications, and Toxicity. *Angew. Chem. Int. Ed.* **2014**, *53*, 1756-1789.

5. Niu, W.; Zhang, L.; Xu, G., Seed-Mediated Growth of Noble Metal Nanocrystals: Crystal Growth and Shape Control. *Nanoscale* **2013**, *5*, 3172-3181.

6. Xia, Y.; Gilroy, K. D.; Peng, H. C.; Xia, X., Seed-Mediated Growth of Colloidal Metal Nanocrystals. *Angew. Chem. Int. Ed.* **2017**, *56*, 60-95.

7. Personick, M. L.; Mirkin, C. A., Making Sense of the Mayhem Behind Shape Control in the Synthesis of Gold Nanoparticles. *J. Am. Chem. Soc.* **2013**, *135*, 18238-18247.

8. Ghosh, S. K.; Pal, T., Interparticle Coupling Effect on the Surface Plasmon Resonance of Gold Nanoparticles: From Theory to Applications. *Chem. Rev.* **2007**, *107*, 4797-4862.

9. Kelly, K. L.; Coronado, E.; Zhao, L. L.; Schatz, G. C., The Optical Properties of Metal Nanoparticles: The Influence of Size, Shape, and Dielectric Environment. *J. Phys. Chem. B* **2003**.

10. Chen, H.; Kou, X.; Yang, Z.; Ni, W.; Wang, J., Shape-and Size-Dependent Refractive Index Sensitivity of Gold Nanoparticles. *Langmuir* **2008**, *24*, 5233-5237.

11. Xia, Y.; Halas, N. J., Shape-Controlled Synthesis and Surface Plasmonic Properties of Metallic Nanostructures. *MRS Bull.* **2005**, *30*, 338-348.

12. Lu, X.; Rycenga, M.; Skrabalak, S. E.; Wiley, B.; Xia, Y., Chemical Synthesis of Novel Plasmonic Nanoparticles. *Annu. Rev. Phys. Chem.* **2009**, *60*, 167-192.

13. Cao, J.; Sun, T.; Grattan, K. T., Gold Nanorod-Based Localized Surface Plasmon Resonance Biosensors: A Review. *Sens. Actuators B Chem.* **2014**, *195*, 332-351.

14. Link, S.; Mohamed, M. B.; El-Sayed, M., Simulation of the Optical Absorption Spectra of Gold Nanorods as a Function of Their Aspect Ratio and the Effect of the Medium Dielectric Constant. *J. Phys. Chem. B* **1999**, *103*, 3073-3077.

15. Millstone, J. E.; Métraux, G. S.; Mirkin, C. A., Controlling the Edge Length of Gold Nanoprisms Via a Seed-Mediated Approach. *Adv. Funct. Mater* **2006**, *16*, 1209-1214.

16. Huang, Y.; Wu, L.; Chen, X.; Bai, P.; Kim, D.-H., Synthesis of Anisotropic Concave Gold Nanocuboids with Distinctive Plasmonic Properties. *Chem. Mater.* **2013**, *25*, 2470-2475.

17. Ghosh, S. K.; Nath, S.; Kundu, S.; Esumi, K.; Pal, T., Solvent and Ligand Effects on the Localized Surface Plasmon Resonance (Lspr) of Gold Colloids. *J. Phys. Chem. B* **2004**, *108*, 13963-13971.

18. Burrows, N. D.; Vartanian, A. M.; Abadeer, N. S.; Grzincic, E. M.; Jacob, L. M.; Lin, W.; Li, J.; Dennison, J. M.; Hinman, J. G.; Murphy, C. J., Anisotropic Nanoparticles and Anisotropic Surface Chemistry. *J. Phys. Chem. Lett.* **2016**, *7*, 632-641.

19. Xia, Y., Concluding Remarks: Anisotropy: The Good, the "Bad" and…. *Faraday Discuss.* **2016**, *191*, 597-604.

20. Scarabelli, L., Recent Advances in the Rational Synthesis and Self-Assembly of Anisotropic Plasmonic Nanoparticles *Pure Appl. Chem.* **2018**, *90*, 1393-1407.

21. Tao, A. R.; Habas, S.; Yang, P., Shape Control of Colloidal Metal Nanocrystals. *Small* **2008**, *4*, 310-325.

22. Jana, N. R.; Gearheart, L.; Murphy, C. J., Wet Chemical Synthesis of High Aspect Ratio Cylindrical Gold Nanorods. *J. Phys. Chem. B* **2001**, *105*, 4065-4067.

23. Nikoobakht, B.; El-Sayed, M. A., Preparation and Growth Mechanism of Gold Nanorods (Nrs) Using Seed-Mediated Growth Method. *Chem. Mater.* **2003**, *15*, 1957-1962.

24. Jana, N. R.; Gearheart, L.; Murphy, C. J., Seed-Mediated Growth Approach for Shape-Controlled Synthesis of Spheroidal and Rod-Like Gold Nanoparticles Using a Surfactant Template. *Adv. Mater.* **2001**, *13*, 1389-1393.

25. Burrows, N. D.; Harvey, S.; Idesis, F. A.; Murphy, C. J., Understanding the Seed-Mediated Growth of Gold Nanorods through a Fractional Factorial Design of Experiments. *Langmuir* **2017**, *33*, 1891-1907.

26. Xia, Y.; Xiong, Y.; Lim, B.; Skrabalak, S. E., Shape-Controlled Synthesis of Metal Nanocrystals: Simple Chemistry Meets Complex Physics? *Angew. Chem. Int. Ed.* **2009**, *48*, 60-103.

27. Liu, M.; Guyot-Sionnest, P., Mechanism of Silver (I)-Assisted Growth of Gold Nanorods and Bipyramids. *J. Phys. Chem. B* **2005**, *109*, 22192-22200.

28. Gole, A.; Murphy, C. J., Seed-Mediated Synthesis of Gold Nanorods: Role of the Size and Nature of the Seed. *Chem. Mater.* **2004**, *16*, 3633-3640.

29. Watt, J.; Hance, B. G.; Anderson, R. S.; Huber, D. L., Effect of Seed Age on Gold Nanorod Formation: A Microfluidic, Real-Time Investigation. *Chem. Mater.* **2015**, *27*, 6442-6449.

30. Park, K.; Hsiao, M.-S.; Koerner, H.; Jawaid, A.; Che, J.; Vaia, R. A., Optimizing Seed Aging for Single Crystal Gold Nanorod Growth: The Critical Role of Gold Nanocluster Crystal Structure. *J. Phys. Chem. C* **2016**, *120*, 28235-28245.

31. Sánchez-Iglesias, A.; Winckelmans, N.; Altantzis, T.; Bals, S.; Grzelczak, M.; Liz-Marzán, L. M., High-Yield Seeded Growth of Monodisperse Pentatwinned Gold Nanoparticles through Thermally Induced Seed Twinning. *J. Am. Chem. Soc.* **2017**, *139*, 107-110.

32. Walsh, M. J.; Barrow, S. J.; Tong, W.; Funston, A. M.; Etheridge, J., Symmetry Breaking and Silver in Gold Nanorod Growth. *ACS Nano* **2015**, *9*, 715-724.

33. Tong, W.; Walsh, M. J.; Mulvaney, P.; Etheridge, J.; Funston, A. M., Control of Symmetry Breaking Size and Aspect Ratio in Gold Nanorods: Underlying Role of Silver Nitrate. *J. Phys. Chem. C* **2017**, *121*, 3549-3559.

34. Walsh, M. J.; Tong, W.; Katz-Boon, H.; Mulvaney, P.; Etheridge, J.; Funston, A. M., A Mechanism for Symmetry Breaking and Shape Control in Single-Crystal Gold Nanorods. *Acc. Chem. Res.* **2017**, *50*, 2925-2935.

35. González-Rubio, G.; Kumar, V.; Llombart, P.; Díaz-Núñez, P.; Bladt, E.; Altantzis, T.; Bals, S.; Peña-Rodríguez, O.; Noya, E. G.; MacDowell, L. G., Disconnecting Symmetry Breaking from Seeded Growth for the Reproducible Synthesis of High Quality Gold Nanorods. *ACS Nano* **2019**, *13*, 4424-4435.

36. Sun, M.; Cheng, Z.; Chen, W.; Jones, M., Understanding Symmetry Breaking at the Single-Particle Level Via the Growth of Tetrahedron-Shaped Nanocrystals from Higher-Symmetry Precursors. *ACS Nano* **2021**.

37. Hubert, F.; Testard, F.; Spalla, O., Cetyltrimethylammonium Bromide Silver Bromide Complex as the Capping Agent of Gold Nanorods. *Langmuir* **2008**, *24*, 9219-9222.

38. Ha, T. H.; Koo, H.-J.; Chung, B. H., Shape-Controlled Syntheses of Gold Nanoprisms and Nanorods Influenced by Specific Adsorption of Halide Ions. *J. Phys. Chem. C* **2007**, *111*, 1123-1130.

39. Fan, X.; Guo, Z.; Hong, J.; Zhang, Y.; Zhang, J.; Gu, N., Size-Controlled Growth of Colloidal Gold Nanoplates and Their High-Purity Acquisition. *Nanotechnology* **2010**, *21*, 105602.

40. Langille, M. R.; Personick, M. L.; Zhang, J.; Mirkin, C. A., Defining Rules for the Shape Evolution of Gold Nanoparticles. *J. Am. Chem. Soc.* **2012**, *134*, 14542-14554.

41. Magnussen, O. M., Ordered Anion Adlayers on Metal Electrode Surfaces. *Chem. Rev.* **2002**, *102*, 679-726.

42. Personick, M. L.; Langille, M. R.; Zhang, J.; Mirkin, C. A., Shape Control of Gold Nanoparticles by Silver Underpotential Deposition. *Nano Lett.* **2011**, *11*, 3394-3398.

43. Zhang, Q.; Jing, H.; Li, G. G.; Lin, Y.; Blom, D. A.; Wang, H., Intertwining Roles of Silver Ions, Surfactants, and Reducing Agents in Gold Nanorod Overgrowth: Pathway Switch between Silver Underpotential Deposition and Gold–Silver Codeposition. *Chem. Mater.* **2016**, *28*, 2728-2741.

44. Grzelczak, M.; Pérez-Juste, J.; Mulvaney, P.; Liz-Marzán, L. M., Shape Control in Gold Nanoparticle Synthesis. *Chem. Soc. Rev.* **2008**, *37*, 1783-1791.

45. Xiang, Y.; Wu, X.; Liu, D.; Feng, L.; Zhang, K.; Chu, W.; Zhou, W.; Xie, S., Tuning the Morphology of Gold Nanocrystals by Switching the Growth of {110} Facets from Restriction to Preference. *J. Phys. Chem. C* **2008**, *112*, 3203-3208.

46. Brown, L.; Holme, T., *Chemistry for Engineering Students; Brooks/Cole: Belmont, 2011*, 2011.

47. Moreau, L. M.; Jones, M. R.; Roth, E. W.; Wu, J.; Kewalramani, S.; O'Brien, M. N.; Chen, B.-R.; Mirkin, C. A.; Bedzyk, M. J., The Role of Trace Ag in the Synthesis of Au Nanorods. *Nanoscale* **2019**, *11*, 11744-11754.

48. Tong, W.; Katz-Boon, H.; Walsh, M. J.; Weyland, M.; Etheridge, J.; Funston, A. M., The Evolution of Size, Shape, and Surface Morphology of Gold Nanorods. *Chem. Commun.* **2018**, *54*, 3022-3025.

49. Rodrigues, T. S.; Zhao, M.; Yang, T. H.; Gilroy, K. D.; da Silva, A. G.; Camargo, P. H.; Xia, Y., Synthesis of Colloidal Metal Nanocrystals: A Comprehensive Review on the Reductants. *Chem. Eur. J* **2018**, *24*, 16944-16963.

50. Eguchi, M.; Mitsui, D.; Wu, H.-L.; Sato, R.; Teranishi, T., Simple Reductant Concentration-Dependent Shape Control of Polyhedral Gold Nanoparticles and Their Plasmonic Properties. *Langmuir* **2012**, *28*, 9021-9026.

51. Vigderman, L.; Zubarev, E. R., High-Yield Synthesis of Gold Nanorods with Longitudinal Spr Peak Greater Than 1200 Nm Using Hydroquinone as a Reducing Agent. *Chem. Mater.* **2013**, *25*, 1450-1457.

52. Zhang, L.; Xia, K.; Lu, Z.; Li, G.; Chen, J.; Deng, Y.; Li, S.; Zhou, F.; He, N., Efficient and Facile Synthesis of Gold Nanorods with Finely Tunable Plasmonic Peaks from Visible to near-Ir Range. *Chem. Mater.* **2014**, *26*, 1794-1798.

53. Scarabelli, L.; Grzelczak, M.; Liz-Marzán, L. M., Tuning Gold Nanorod Synthesis through Prereduction with Salicylic Acid. *Chem. Mater.* **2013**, *25*, 4232-4238.

54. Moussawi, R. N.; Patra, D., Synthesis of Au Nanorods through Prereduction with Curcumin: Preferential Enhancement of Au Nanorod Formation Prepared from Ctab-Capped over Citrate-Capped Au Seeds. *J. Phys. Chem. C* **2015**, *119*, 19458-19468.

55. Rajendra, R.; Gangadharan, P. K.; Tripathi, S.; Kurungot, S.; Ballav, N., High-Index Faceted Au Nanocrystals with Highly Controllable Optical Properties and Electro-Catalytic Activity. *Nanoscale* **2016**, *8*, 19224-19228.

56. Ahmad, T., Reviewing the Tannic Acid Mediated Synthesis of Metal Nanoparticles. *J. Nanotechnol.* **2014**, *2014*.

57. Zhang, X.; Gallagher, R.; He, D.; Chen, G., Ph Regulated Synthesis of Monodisperse Penta-Twinned Gold Nanoparticles with High Yield. *Chem. Mater.* **2020**, *32*, 5626-5633.

58. Shi, Y.; Lyu, Z.; Zhao, M.; Chen, R.; Nguyen, Q. N.; Xia, Y., Noble-Metal Nanocrystals with Controlled Shapes for Catalytic and Electrocatalytic Applications. *Chem. Rev.* **2020**, *121*, 649-735.

59. Zhang, Q.; Wang, H., Facet-Dependent Catalytic Activities of Au Nanoparticles Enclosed by High-Index Facets. *ACS Catal.* **2014**, *4*, 4027-4033.

60. Gao, W.; Song, E. H.; Jiang, Q.; Jacob, T., Revealing the Active Intermediates in the Oxidation of Formic Acid on Au and Pt (111). *Chem. Eur. J* **2014**, *20*, 11005-11012.

61. Li, J.; Wang, L.; Liu, L.; Guo, L.; Han, X.; Zhang, Z., Synthesis of Tetrahexahedral Au Nanocrystals with Exposed High-Index Surfaces. *Chem. Commun.* **2010**, *46*, 5109-5111.

62. Reguera, J.; Langer, J.; de Aberasturi, D. J.; Liz-Marzán, L. M., Anisotropic Metal Nanoparticles for Surface-Enhanced Raman Scattering. *Chem. Soc. Rev.* **2020**, 3866-3885.

63. Romo-Herrera, J.; González, A.; Guerrini, L.; Castiello, F.; Alonso-Nuñez, G.; Contreras, O.; Alvarez-Puebla, R., A Study of the Depth and Size of Concave Cube Au Nanoparticles as Highly Sensitive Sers Probes. *Nanoscale* **2016**, *8*, 7326-7333.

Mechanistic Insight into the Evolution of Au Nanorod to Concave Cuboid Au NCs

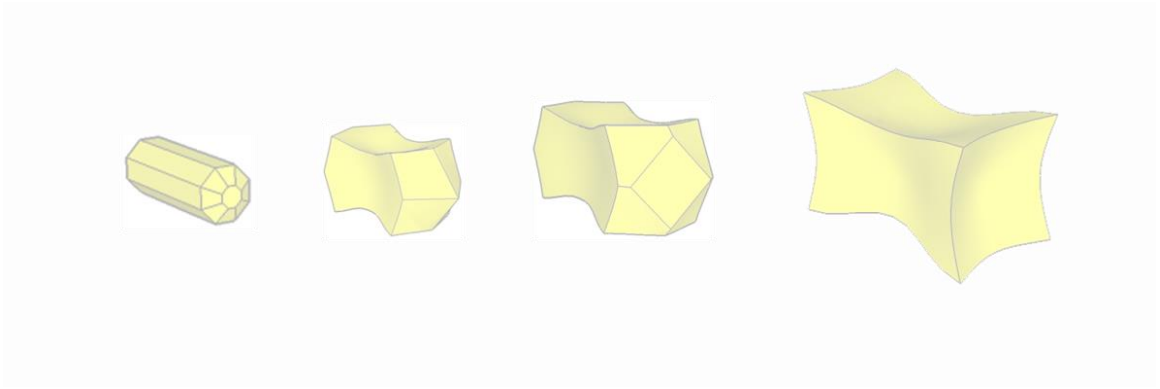

2.1 Introduction

The exceptional chemical stability, catalytic activity, processability, and unique surface plasmon resonance (SPR) property associated with anisotropic Au NCs have attracted a great deal of attention from the scientific community.[1] However, to exploit Au nanocrystals (NCs) to their full potential for various applications demand synthetic techniques that can judiciously tune their size and morphology.[2-5] Among various synthetic routes available, the seed-mediated growth method, because of its versatility, has been the most popular choice giving rise to a myriad of nanostructures with distinct optical and catalytic properties.[6-10] Furthermore, based on the atomic arrangement on the surface of the metal, nanoparticles have been classified into two domains, low and high index facet (HIF) nanocrystals.[9,11-13] HIF NCs possess high surface energy due to the presence of loosely packed atomic arrangements at steps, kinks, and ledges on the surface which render them promising materials in catalysis.[14] In the past decade, efforts from various research groups have yielded a series of HIF NCs via seed-mediated synthesis, which are enclosed by either convex or concave surfaces.[3,15-19] However, concave nanostructures hold some interesting structural features over convex counterparts, such as indented faces, sharp corners, and edges making them captivating materials in fundamental and application studies.[17,20,21] Since the formation of the concave nanostructure is not thermodynamically favourable and requires relatively more energy than that for a convex counterpart, the synthesis of such structures remains challenging.[5,18] In 2010, Mirkin and co-workers devised a new methodology for the synthesis of concave cubic Au NCs where CTAC was used as a surfactant to access the dimensions in the range of 40-270 nm and it was anticipated that the presence of excess amounts of Cl^- was favouring the formation of concave morphology.[3,22] It was not until 2013 when CCB Au NCs were synthesized for the first time exhibiting interesting optical properties, i.e., three plasmon oscillation modes, which were assigned as transverse edge mode (T1), transverse hybrid mode (T2), and longitudinal corner mode (L3).[23] This was shortly followed by few synthetic protocols to obtain decent yield of CCB Au NCs. All the existing reports utilized Br^- ion containing surfactant as shape directing agent (either as a stand-alone or in conjunction with another surfactant)[19,24-27] which contradicted earlier predictions that Br^- does not favour the concave structure formation.[22,28] This might be the reason that caused the poor yield and dimension controllability in the existing

reports to date and thereby limited the exploration of concave Au NCs in a wide application range despite holding good promise.

Herein, we have investigated the role of Cl^- ions in the synthetic protocol devised in our lab to generate Au CCB NCs. It was revealed that the presence of Cl^- ions is indeed playing a determining role despite the cationic counterpart of surfactant (BDAC and CPC here). Further, it has been demonstrated that the presence of Br^- (replacing CTAC with CTAB) would not favour the concave structure formation, which contradicts the earlier reports.[23-25,27] Additionally, we have also shined light on the evolution of such particles. Furthermore, Au CCB NCs of varying sizes have been exploited for their electrocatalytic behaviour towards formic acid oxidation.

2.2 Materials/Methods

Gold(III) chloride trihydrate ($HAuCl_4.3H_2O$), silver nitrate ($AgNO_3$), cetyltrimethylammonium bromide (CTAB), cetyltrimethylammonium chloride (CTAC), cetylpyridinium chloride (CPC), benzyldimethylhexadecylammonium chloride (BDAC), sodium borohydride ($NaBH_4$) and tannic acid (TA) were purchased from Sigma-Aldrich. Sodium hydroxide (NaOH; analytical reagent) was bought from Rankem. All chemicals were used as such. Milli-Q water (18.2 MΩ-cm) was used for all experiments.

Investigation of Growth Mechanism. The synthesis of Au NRs seed was performed following the reported protocol.[29] Excess surfactant (CTAB) was removed by performing centrifugation (9000 rpm, 7 min) twice with Milli-Q water and finally redispersed in 0.1 M CTAC aqueous solution. To investigate the role of the cationic part of surfactant, growth solution containing appropriate amount of water (in order to make a total volume of 2 mL), NaOH (20 μL, 0.1 M), $HAuCl_4$ (0.25 mL, 4 mM), $AgNO_3$ (50 μL, 4 mM) and 100 μL seed were maintained with only CTAC (1 mL, 0.2 M) being replaced by CPC (1 mL, 0.2 M) and BDAC (1 mL, 0.2 M) individually, to maintain the $HAuCl_4$:surfactant ratio 1:200 in the growth solution. To study the role of anionic part of the surfactant, CTAC was completely/partially (1/19 or 1/2 of CTAC) replaced with CTAB. The evolution studies were done for the case, 100 μL seed and 50 μL $AgNO_3$, by extracting the aliquots from the growth solution at different time points, i.e., 10 s, 15 min, 30 min, 60 min, 120 min, 240 min, 360 min, and 24 h as the reaction progressed.

Electrocatalytic Activity of CCB Au NCs. This experiment was performed as follows, CCB Au NCs were washed twice with water by centrifugation and then loaded the amount of 85 μg on a glassy carbon electrode; this electrode was used as working electrode. Graphite rod and Ag/AgCl were used as counter and reference electrodes, respectively. Electrocatalysis of formic acid (1 M) was performed in H_2SO_4 (0.5 M) solution by applying the voltage scan rate of 50 mVs^{-1}. Nitrogen gas purging was allowed throughout the experiment. The first two measurement cycles were discarded to avoid the interference of absorbed gases in the solution.
Characterization. UV-vis spectra were recorded from Chemito SPECTRASCAN UV 2600. Field-emission scanning electron microscopy (FE-SEM) images were captured through ZEISS Ultra Plus and transmission electron microscopy (TEM) images were captured through TITAN 80-300 Image Cs corrector and Tecnai F30, both operated at 300 kV.

2.3 Results and Discussion

As all the previously reported synthetic protocols were carried out in the presence of Br^- containing surfactant, we wanted to gain insights into the role of the halide counter anion in the surfactant as well as the cationic part of it. Control experiments were performed in which Br^- was deliberately introduced into the growth solution in the form of CTAB. CCB Au NCs exhibit three characteristic SPR peaks; however, the UV-vis spectra of the Br^- induced growth solutions were starkly different from that of CCB Au NCs synthesized in the presence of CTAC only (Figure 2.2a). It was found that such solutions consistently lead to irregularly shaped Au NCs, thus affecting the morphology and the product yield when compared to only CTAC (Figure 2.2b). Another remarkable observation was made when the same amount (5% or 19:1 of CTAC: CTAB) of Br^- was added to the overgrowth solutions with varying concentrations of seed. The disruption to the formation of the CCB structure was more marked as the concentration of seed in the growth solution was decreased (Figure 2.1b-e). When the overgrowth of NR was performed in a 1:1 ratio of CTAC and CTAB binary surfactant mixture, it led to the formation of irregularly shaped bars with convex surfaces coming into prominence as the concentration of seed was decreased (Figure 2.1g-j). The formation of convex surfaces in the presence of Br^- containing surfactant has been observed earlier,[15,29] and it shows clearly that even in a 1:1 mixture, Br^- anions dictates the final morphology, aiding the creation of a convex surface.

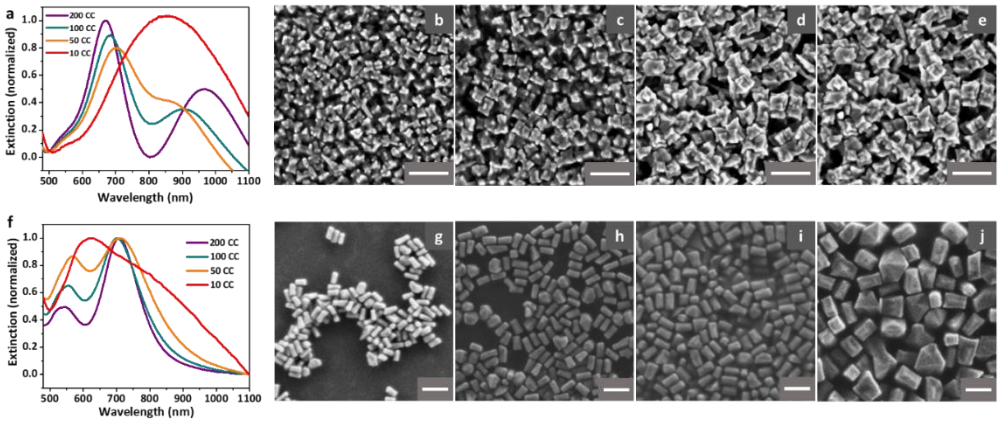

Figure 2.1: (a) UV-vis spectra of CCB Au NCs synthesized with varying the amount of seed in the growth solution as 200, 100, 50, 10 µL in a 19:1 CTAC:CTAB growth solution. (b-e) FE-SEM images were captured for the corresponding samples; (f) UV-vis spectra of CCB Au NCs synthesized with varying the amount of seed in the growth solution as 200, 100, 50, 10 µL in a 1:1 CTAC:CTAB growth solution. (g-j) FE-SEM images were captured for the corresponding samples; the scale bar is 200 nm for all.

To further test the role of Cl^- ions, the overgrowth of NR was carried out in the presence of other C_{16}TAC analogues keeping the length of the hydrocarbon tail and counter-anion constant and varying only the headgroup, (CPC and BDAC), in an otherwise identical reaction condition. Though CCB Au NCs were obtained in decent yield, the concavity appeared to be much less prominent and the corners were somewhat obtuse when compared to CCB Au NCs from a CTAC assisted reaction (Figure 2.2a-d). Another interesting trend that comes to notice is that an improvement in the yield, as well as morphology is observed in the 1:1 binary mixture of a Cl^- containing surfactant (BDAC or CPC) and CTAC, thus underlying the importance of CTAC yet again in the generation of uniform CCBs and that Cl^- containing surfactant is indispensable when it comes to the generation and stabilization of concave surfaces (Figure 2.2f-h).

This may be attributed to various factors acting synergistically to generate and stabilize a thermodynamically unfavourable site. The reduction potential of Au^{3+} ion in the presence of Cl^- ions (CTAC) is greater than that of Br^- ions (CTAB) which means that the rate of conversion from Au^{3+} to Au^0 is higher in the presence of CTAC than in the presence of CTAB. Thus, when the atoms are supplied at a faster rate, the tendency of the atoms to migrate is considerably low. However, a significantly reduced rate of atom production gives them enough time to migrate

to other sites. This is how the experimental conditions related to reaction kinetics get affected in the presence of the capping agents differing only in the anionic part.[5] Compiled with it is the fact that the binding strength of Cl^- to Au surface closely resembles that of Ag surface. A consequence of the above behaviour is that Cl^- does not compete considerably with Ag for Au surface. This boosts the underpotential deposition (UPD) of Ag on the Au surface, which is extremely difficult to remove or rearrange, again paving the way for the incoming Au atoms to be deposited along the free edges and corners. Br^- on the other hand by virtue of its greater binding strength and affinity for Au surface not only competes with Ag for Au surface but also destabilizes the Ag (UPD) layer resulting in a dynamic Ag layer, that is, increase the diffusion rate of surface atoms.[22] Therefore, as-deposited Au atoms along the edges and corners would diffuse toward the faces, and this is why the addition of Br^- changes the morphology as well as makes the concavity disappear. However, the existing literature on Au CCB NCs seems to contradict this well-established theory. Thus, the CTA^+ backbone is also important but not essential, observed from the experiments performed using CPC and BDAC to form the concave structure.

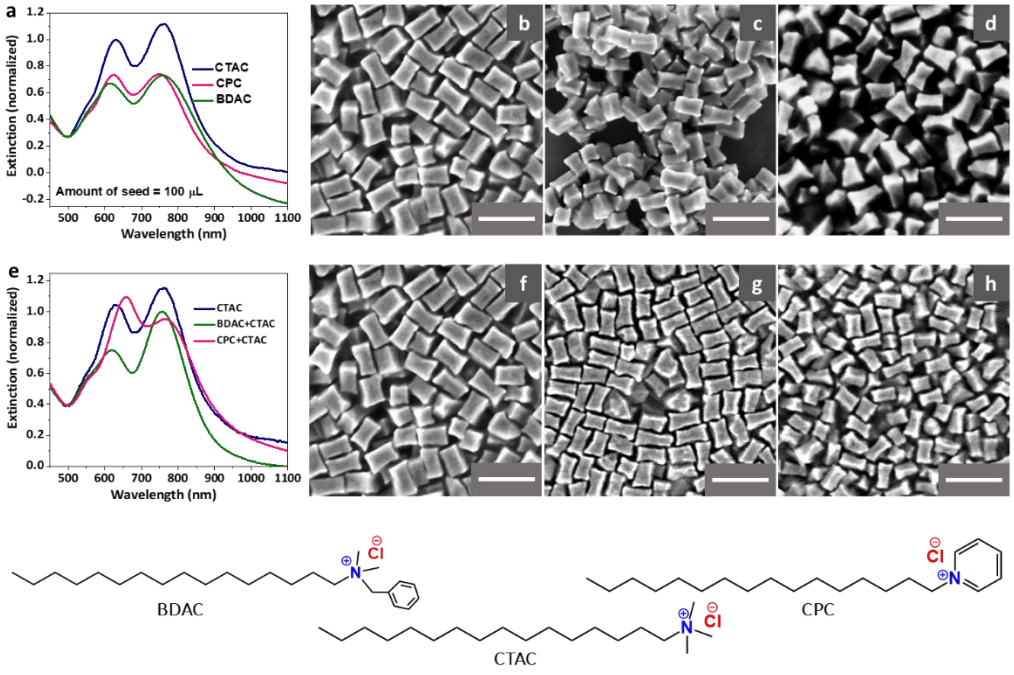

Figure 2.2: (a) UV-vis spectra recorded for the CCB Au NCs synthesized in the presence of various Cl^- containing surfactants, CTAC, CPC, BDAC; and (b-d) FE-SEM images for the corresponding samples respectively; (f) UV-vis spectra of CCBs synthesized in the presence of CTAC, 1:1 CTAC:CPC and 1:1 CTAC:BDAC binary surfactant mixture. (e-h) FE-SEM images were captured for the

corresponding samples; the scale bar is 200 nm for all FE-SEM images. Below: Structure of the chloride-based surfactants.

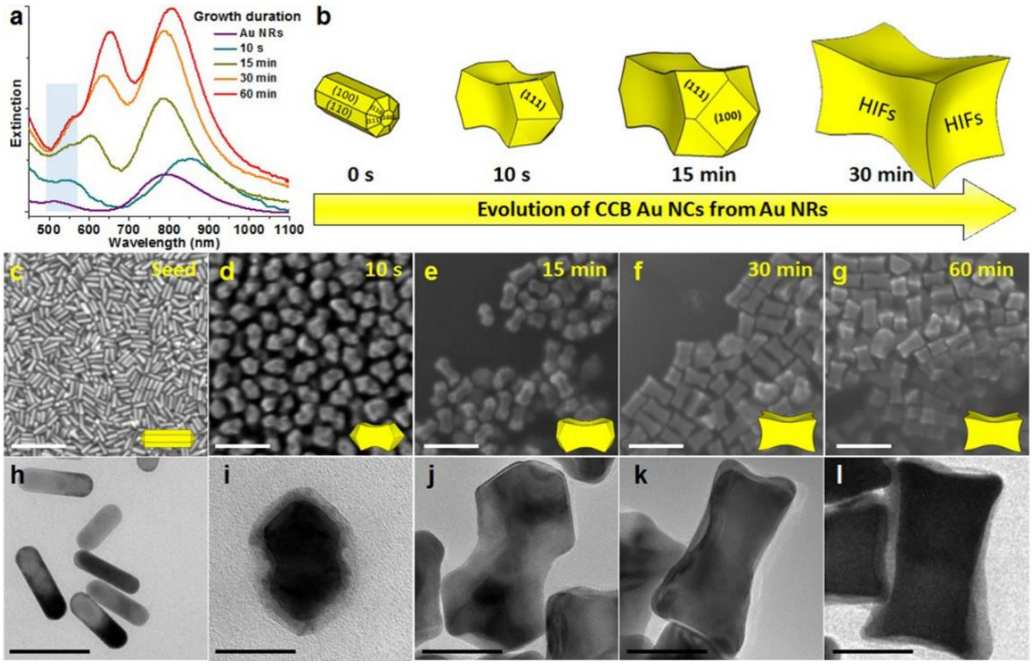

Figure 2.3: (a) UV-vis spectra recorded at different time points from the addition of Au NRs seed, 10 s, 15, 30, and 60 min during the evolution of CCB Au NCs; Au NRs seed spectrum (purple color) is included as a reference. (b) Schematic representation for the evolution of CCB Au NCs from Au NR seed. (c-g) FE-SEM images showing the morphological evolution of nanoparticles from (c) rods (seed), to (d) AH Au NRs, to (e) truncated CCB, to (f, g) CCB shape with an increase in time as few 10 s, 15, 30, and 60 min, respectively; scale bar is 100 nm for all. (h-l) TEM images corresponding to the FE-SEM images right above; scale bar is 50 nm for all.

To study the morphological transformation of the CCBs from NRs, the evolution process was monitored by UV-vis spectroscopy, FE-SEM and TEM measurements (Figure 2.3). For this, aliquots were taken out from the growth solution at certain time intervals followed by measuring the UV-vis spectra of the sample (Figure 2.3a). Figure 2.3b shows our proposed models illustrating the evolution from NR to CCB Au NCs; and FE-SEM (Figure 2.3c-g) and TEM (Figure 2.3h-l) images of the NRs (seed) and intermediates sampled at 10 s, 15, 30, and 60 min, respectively. Au NRs are proposed to be single crystalline- enclosed with, {100}, {110}, and {111} planes (Figure 2.3b) with their associated energy order being {110} > {100} > {111}.[30] Therefore, the presence of the higher energy surfaces and low packing density of CTAC at the Au NR ends facilitate the relatively more deposition of Au^0 at ends rather than

lateral facets. In addition to this, growth/deposition rate is very high at the initial stage, owing to the presence of a higher concentration of $AuCl_4^-$ and smaller size of seed (Au NRs) in the growth solution during which the less stable surfaces grow out very rapidly leading to their disappearance. The first aliquot was taken out from the solution after few seconds (10 s) of the Au NRs seed addition; the LSPR and TSPR bands in the UV-vis spectra (Figure 2.3a) were red-shifted, indicating the increment in length (with sharp ends) and breadth due to the transformation of cylindrical Au NRs into arrow-headed (AH) Au NRs (Figure 2.3d). The ends of AH Au NRs enclosed with {111} planes that resulted from the preferential growth of {110} and {100} planes on the ends of cylindrical Au NRs (Figure 2.3b).[31] After 15 min, the UV-vis spectra showed the splitting of the TSPR band (Figure 2.3a) into two, that is, edge (T1) and hybrid (T2; edge + corner) modes, a signature of surface indentation or protrusion of lateral edges.[23] This is complimented by the FE-SEM/TEM images (Figure 2.3e and j), which shows structures that can be called as truncated CCB Au NCs structures with surface concavity. These intermediates consisting of planes at truncated region (Figure 2.3b), seem to result from further deposition of Au^0 on planes of ends and, lateral edges of AH Au NRs. Complete formation of CCB Au NCs was noticed after 30 min. This morphology remained intact with only the sharpening of the corners as the reaction progressed until 24 h. By the time the reaction progressed to 30 min, due to considerable consumption of the $AuCl_4^-$ in the initial stages of the reaction, the growth had slowed down. In the latter stages no significant change in morphology was observed.

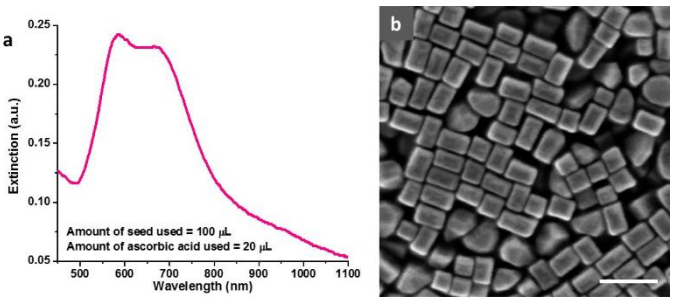

Figure 2.4: (a) UV-vis spectra of Au NCs synthesized in the presence of ascorbic acid (AA). (b) Corresponding FE-SEM image showing cuboids with concave faces; scale bar is 200 nm.

It was shown in the earlier report that at higher growth rate (by increasing the ratio of AA/Au^{3+} or Au^{3+}/CTAB) or presence of $Ag/Au^{3+} > 1:2$ (at $AA/Au^{3+} = 10:1$ and 0.1 M CTAB) Au NRs transform into AH Au NRs whereas at lower growth rate or $Ag/Au^{3+} < 1:2$ led to bowtie like

nanostructures.[31] Based on an earlier report we anticipate that at the initial stage of growth (<10 s; the growth rate is very high) silver assisted the evolution of seed via electroless co-deposition and generated arrow-headed intermediate whereas on the later stages (>15 min; lower growth rate) it acted through UPD and led to truncated and then CCB structures.[32]

When it comes to a mild reducing agent in Au NPs synthesis, AA has been the front runner, however, the narrow pH window of its operation is becoming a detrimental factor.[33] In our earlier work,[29] we have successfully implemented TA for the synthesis of convex Au NCs with HIF (elongated tetrahexahedra, ETHH). In this work, we have duly used TA for the dimension-controlled synthesis of CCB Au NCs. As a matter of fact, synthesis carried out in the presence of AA resulted in CCB Au NCs with poor morphological yield, wherein, the concavity was restricted only to the faces and not edges, reflected in the UV-vis spectra as well where two instead of three characteristic SPR peaks were observed (Figure 2.4). Thus, TA appears to be a more robust alternative to AA for the seed-mediated synthesis of various anisotropic Au NCs.

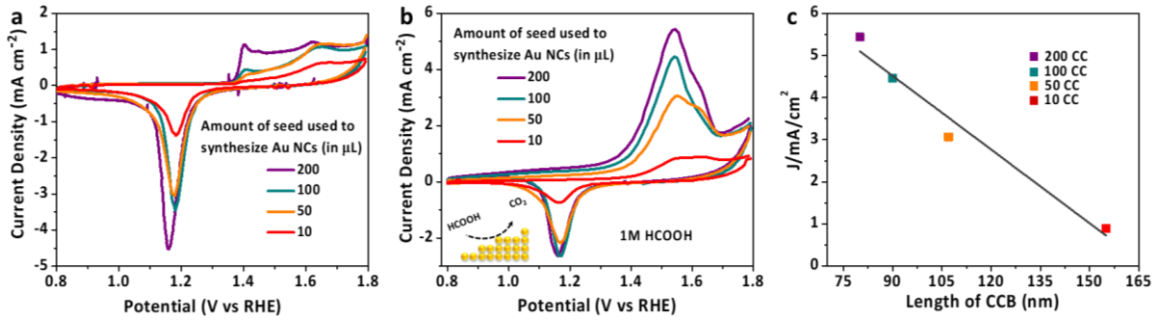

Figure 2.5: (a) CV traces recorded for CCB Au NCs with different sizes in the presence of 0.5 M H_2SO_4. (b) CV traces for the oxidation of 1 M HCOOH by CCB Au NCs with different sizes. (c) Plot of maximum current density vs length of CCB Au NCs showing a linear relationship.

Since cyclic-voltammetry (CV) can be used to assess the various surface structures of metal nanoparticles as shown recently for the high-index faceted Au NCs,[15,29] CV traces for CCB Au NCs with different sizes were recorded in 0.5 M H_2SO_4 solution (Figure 2.5a). CV traces of the CCB Au NCs exhibited an oxidation peak around 1.4 V with a prominent reduction peak around 1.18 V in line with earlier observations, where other Au NCs bound by high-index facets were studied [15, 29, 34] indicating that the surface atoms of nanostructures are easier to oxidize. Also, the current value consistently decreased with increasing the size (Figure 2.5a). Further, to check the chemical activity of surface atoms of the as-synthesized CCB Au NCs,

different concave particles were tested for their electrocatalytic oxidation of Formic acid (HCOOH) by CV. CV traces of CCB Au NCs with different sizes exhibited an oxidation peak at $1.3 < V < 1.7$, which showed that single formate was the active intermediate via which the oxidation took place (Figure 2.5b). This oxidation peak comprises of direct formate electro-oxidation and Au surface oxidation.[35] Additionally, the peak current density value decreased with increasing the size of CCB Au NCs, showing a close to linear relationship similar to those observed in the case of ETHH Au NCs[29] (Figure 2.5c). Thus, the Cl^- directed overgrowth of Au NRs gives rise to CCB Au NCs with precise control over dimension, resulting in controllable electro-catalytic activity.

2.4 Summary and Conclusions

We have successfully shown how Cl^- plays a determining role in the formation of CCB Au NCs rather than the headgroup of counter cationic part of the surfactant (BDAC and CPC). In addition, it has also been proven that Br^- does not favour the formation of concave morphology by partially or completely replacing the CTAC with CTAB in the growth media under similar experimental conditions. Therefore, we predict that the absence of size tunability and decent yield of CCB Au NCs in the existing reports may be due to the utilization of Br^- containing surfactants. Moreover, isolation of the two prominent intermediates, arrow-headed and truncated CCB, throws some light on the mechanistic pathway followed. Finally, such well-defined CCB Au NCs with desired dimensions provided access to the controllable and reproducible electro-catalytic activity.

2.5 References

(1) Eustis, S.; El-Sayed, M. A. Why Gold Nanoparticles Are More Precious Than Pretty Gold: Noble Metal Surface Plasmon Resonance and Its Enhancement of the Radiative and Nonradiative Properties of Nanocrystals of Different Shapes. *Chem. Soc. Rev.* **2006**, *35*, 209.

(2) Xia, Y.; Xiong, Y.; Lim, B.; Skrabalak, S. E. Shape-Controlled Synthesis of Metal Nanocrystals: Simple Chemistry Meets Complex Physics? *Angew. Chem., Int. Ed.* **2009**, *48*, 60.

(3) Zhang, J.; Langille, M. R.; Personick, M. L.; Zhang, K.; Li, S.; Mirkin, C. A. Concave Cubic Gold Nanocrystals with High-Index Facets. *J. Am. Chem. Soc.* **2010**, *132*, 14012.

(4) Hong, J. W.; Lee, S.-U.; Lee, Y. W.; Han, S. W. Hexoctahedral Au Nanocrystals with High-Index Facets and Their Optical and Surface-Enhanced Raman Scattering Properties. *J. Am. Chem. Soc.* **2012**, *134*, 4565.

(5) Zhang, H.; Jin, M.; Xia, Y. Noble-Metal Nanocrystals with Concave Surfaces: Synthesis and Applications. *Angew. Chem., Int. Ed.* **2012**, *51*, 7656.

(6) Jana, N. R.; Gearheart, L.; Murphy, C. J. Wet Chemical Synthesis of High Aspect Ratio Cylindrical Gold Nanorods. *J. Phys. Chem. B* **2001**, *105*, 4065.

(7) Nikoobakht, B.; El-Sayed, M. A. Preparation and Growth Mechanism of Gold Nanorods (NRs) Using Seed-Mediated Growth Method. *Chem. Mater.* **2003**, *15*, 1957.

(8) Wu, H.-L.; Chen, C.-H.; Huang, M. H. Seed-Mediated Synthesis of Branched Gold Nanocrystals Derived from the Side Growth of Pentagonal Bipyramids and the Formation of Gold Nanostars. *Chem. Mater.* **2009**, *21*, 110.

(9) Wu, H.-L.; Kuo, C.-H.; Huang, M. H. Seed-Mediated Synthesis of Gold Nanocrystals with Systematic Shape Evolution from Cubic to Trisoctahedral and Rhombic Dodecahedral Structures. *Langmuir* **2010**, *26*, 12307.

(10) Yu, Y.; Zhang, Q.; Lu, X.; Lee, J. Y. Seed-Mediated Synthesis of Monodisperse Concave Trisoctahedral Gold Nanocrystals with Controllable Sizes. *J. Phys. Chem. C* **2010**, *114*, 11119.

(11) Niu, W.; Zheng, S.; Wang, D.; Liu, X.; Li, H.; Han, S.; Chen, J.; Tang, Z.; Xu, G. Selective Synthesis of Single-Crystalline Rhombic Dodecahedral, Octahedral, and Cubic Gold Nanocrystals. *J. Am. Chem. Soc.* **2009**, *131*, 697.

(12) Zhang, L.; Niu, W.; Xu, G. Synthesis and Applications of Noble Metal Nanocrystals with High-Energy Facets. *Nano Today* **2012**, *7*, 586.

(13) Quan, Z.; Wang, Y.; Fang, J. High-Index Faceted Noble Metal Nanocrystals. *Acc. Chem. Res.* **2013**, *46*, 191.

(14) Zhang, Q.; Wang, H. Facet-Dependent Catalytic Activities of Au Nanoparticles Enclosed by High-Index Facets. *ACS Catal.* **2014**, *4*, 4027.

(15) Ming, T.; Feng, W.; Tang, Q.; Wang, F.; Sun, L.; Wang, J.; Yan, C. Growth of Tetrahexahedral Gold Nanocrystals with High-Index Facets. *J. Am. Chem. Soc.* **2009**, *131*, 16350.

(16) Tran, T. T.; Lu, X. Synergistic Effect of Ag and Pd Ions on Shape-Selective Growth of Polyhedral Au Nanocrystals with High Index Facets. *J. Phys. Chem. C* **2011**, *115*, 3638.

(17) Lee, H.-E.; Yang, K. D.; Yoon, S. M.; Ahn, H.-Y.; Lee, Y. Y.; Chang, H.; Jeong, D. H.; Lee, Y.-S.; Kim, M. Y.; Nam, K. T. Concave Rhombic Dodecahedral Au Nanocatalyst with Multiple High-Index Facets for CO_2 Reduction. *ACS Nano* **2015**, *9*, 8384.

(18) Xia, Y.; Xia, X.; Peng, H.-C. Shape-Controlled Synthesis of Colloidal Metal Nanocrystals: Thermodynamic Versus Kinetic Products. *J. Am. Chem. Soc.* **2015**, *137*, 7947.

(19) Zhang, Q.; Zhou, Y.; Villarreal, E.; Lin, Y.; Zou, S.; Wang, H. Faceted Gold Nanorods: Nanocuboids, Convex Nanocuboids, and Concave Nanocuboids. *Nano Lett.* **2015**, *15*, 4161.

(20) Rycenga, M.; Langille, M. R.; Personick, M. L.; Ozel, T.; Mirkin, C. A. Chemically Isolating Hot Spots on Concave Nanocubes. *Nano Lett.* **2012**, *12*, 6218.

(21) Matteini, P.; de Angelis, M.; Ulivi, L.; Centi, S.; Pini, R. Concave Gold Nanocube Assemblies as Nanotraps for SurfaceEnhanced Raman Scattering-Based Detection of Proteins. *Nanoscale* **2015**, *7*, 3474.

(22) Langille, M. R.; Personick, M. L.; Zhang, J.; Mirkin, C. A. Defining Rules for the Shape Evolution of Gold Nanoparticles. *J. Am. Chem. Soc.* **2012**, *134*, 14542.

(23) Huang, Y.; Wu, L.; Chen, X.; Bai, P.; Kim, D.-H. Synthesis of Anisotropic Concave Gold Nanocuboids with Distinctive Plasmonic Properties. *Chem. Mater.* **2013**, *25*, 2470.

(24) Zhang, L. F.; Zhang, C. Y. Controlled Growth of Concave Gold Nanobars with High Surface-Enhanced Raman-Scattering and Excellent Catalytic Activities. *Nanoscale* **2013**, *5*, 5794.

(25) Li, L.; Peng, Y.; Yue, Y.; Hu, Y.; Liang, X.; Yin, P.; Guo, L. Synthesis of Concave Gold Nanocuboids with High-Index Facets and Their Enhanced Catalytic Activity. *Chem. Commun.* **2015**, *51*, 11591.

(26) Zhang, Q.; Han, L.; Jing, H.; Blom, D. A.; Lin, Y.; Xin, H. L.; Wang, H. Facet Control of Gold Nanorods. *ACS Nano* **2016**, *10*, 2960.

(27) Xie, X.; Gao, G.; Kang, S.; Lei, Y.; Pan, Z.; Shibayama, T.; Cai, L. Toward Hybrid Au Nanorods @ M (Au, Ag, Pd and Pt) Core-Shell Heterostructures for Ultrasensitive Sers Probes. *Nanotechnology* **2017**, *28*, 245602.

(28) Personick, M. L.; Mirkin, C. A. Making Sense of the Mayhem Behind Shape Control in the Synthesis of Gold Nanoparticles. *J. Am. Chem. Soc.* **2013**, *135*, 18238.

(29) Rajendra, R.; Gangadharan, P. K.; Tripathi, S.; Kurungot, S.; Ballav, N. High-Index Faceted Au Nanocrystals with Highly Controllable Optical Properties and Electro-Catalytic Activity. *Nanoscale* **2016**, *8*, 19224.

(30) Liu, M.; Guyot-Sionnest, P. Mechanism of Silver(I)-Assisted Growth of Gold Nanorods and Bipyramids. *J. Phys. Chem. B* **2005**, *109*, 22192.

(31) Xiang, Y.; Wu, X.; Liu, D.; Feng, L.; Zhang, K.; Chu, W.; Zhou, W.; Xie, S. Tuning the Morphology of Gold Nanocrystals by Switching the Growth of {110} Facets from Restriction to Preference. *J. Phys. Chem. C* **2008**, *112*, 3203.

(32) Zhang, Q.; Jing, H.; Li, G. G.; Lin, Y.; Blom, D. A.; Wang, H. Intertwining Roles of Silver Ions, Surfactants, and Reducing Agents in Gold Nanorod Overgrowth: Pathway Switch between Silver Underpotential Deposition and Gold-Silver Codeposition. *Chem. Mater.* **2016**, *28*, 2728.

(33) Borsook, H.; Keighley, G. Oxidation-Reduction Potential of Ascorbic Acid (Vitamin C). *Proc. Natl. Acad. Sci. U. S. A.* **1933**, *19*, 875.

(34) Concave Gold Nanoparticle-based Highly Sensitive Electrochemical IgG Immunobiosensor for the Detection of AntibodyAntigen Interactions. *RSC Adv.* **2015**, *5*, 58478.

(35) Besenhard, J.O.; Parsons, R.; Reeves, R.M. The Role of Surface Oxides in Formic Acid Oxidation on Au. *J. Electroanal.Chem.* **1979**, *96*, 57.

Controlling the Aspect Ratios of Au NCs with Ag^+ Addition Time in Seed-Mediated Synthesis

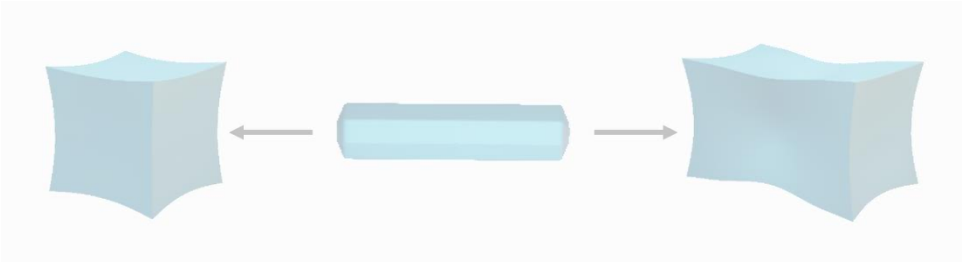

3.1 Introduction

Over the past two decades, seed-mediated growth of noble metal nanocrystals (NCs) have emerged as an elegant wet chemical synthetic procedure producing myriads of nanostructures with highly controllable dimensions.[1-5] One of the essential chemical additives in the seed-mediated synthesis of Au NCs is $AgNO_3$ (Ag^+), widely regarded as a shape directing agent, regulating the structural evolution of Au NCs.[6-10] Recent studies have shown a correlation of the concentration of Ag^+ with the shape and index of the facets of Au NCs.[11,12] Several other studies have attributed the shape directing effect to an under potential deposition (UPD) of Ag onto the surface of the Au nanoparticles.[13-15] It has also been outlined how $AgNO_3$ controls the size of NCs at which an isotropic structure breaks the symmetry and anisotropic growth begins, again from the perspective of the concentration of $AgNO_3$.[7,16] Furthermore, increasing the concentration of $AgNO_3$ in the growth solution has been observed to increase the aspect ratio (AR) of Au nanorods (NRs), which is perhaps the most widely studied anisotropic Au NC system.[2,17] In the latter study,[17] the timing of Ag^+ addition was used as a tool to underpin the stage, where symmetry breaking begins and the critical size of the NCs is associated with the event, not specifically to tune the ARs of the resultant NCs. Herein, we present for the first time, the critical role of timing of Ag^+ addition into the growth solution leading to Au NCs with varying ARs, while keeping the amount of Ag^+ (also other reagents) same. Specifically, we have studied the effect of delaying the addition of $AgNO_3$ in the overgrowth of Au NRs in the presence of cetyltrimethylammonium chloride (CTAC).

We illustrate that Au NCs with tunable ARs can be generated in one system simply by regulating the time of addition of Ag^+ in the growth solution. A concomitant decrease in the ARs of the concave cuboid (CCB) Au NCs with delay in the time of addition of $AgNO_3$ to the growth solution was observed with the formation of the concave cube (CC, AR = 1) Au NCs instead of CCB Au NCs upon delayed addition of Ag^+. We further demonstrated the generality of this method by successfully preparing tetrahexahedra (THH, AR = 1) Au NCs in place of elongated tetrahexahedra (ETHH) Au NCs upon timed addition of $AgNO_3$ during overgrowth of Au NRs in the presence of cetyltrimethylammonium bromide (CTAB). Notably, till now, spherical Au NCs have been used as seeds to generate the isotropic high-index faceted CC and THH Au NCs. Thus, apart from providing new mechanistic insights, a major highlight of the

current work is the generation of isotropic CC and THH Au NCs from anisotropic Au NR seeds-a hitherto unreported finding in the field.[18-20] Surface enhanced Raman scattering (SERS) studies carried out on the resultant Au NCs on the two extreme spectra of the current study, viz, CCB and CC Au NCs exhibit significantly enhanced SERS performance in the order of 10^5 for Nile blue (NB) used as the probe molecule. SERS efficiency for the abovementioned Au NCs used as substrates varied only marginally, with CC Au NCs exhibiting a better efficiency than CCB Au NCs.

3.2 Materials/Methods

Gold(III) chloride trihydrate ($HAuCl_4 \cdot 3H_2O$), silver nitrate ($AgNO_3$), CTAB, CTAC, TA and sodium borohydride ($NaBH_4$) were purchased from Sigma-Aldrich. Sodium hydroxide (NaOH; analytical reagent) was bought from Rankem. All chemicals were used as received. Milli-Q water (18.2 MΩ·cm) was used for all experiments.

Synthesis of CCB and CC Au NCs. Briefly, growth solution was first prepared by the addition of 1 mL of 0.2 M CTAC, 20 μL of 100 mM NaOH, 250 μL of 4 mM $HAuCl_4$, and 10 μL 100 mM TA followed by the addition of 50 μL of Au NR seeds to initiate the reaction. The solution was gently mixed, and 50 μL of 4 mM $AgNO_3$ was added at time intervals of 1.5, 5, 15, and 30 min from the addition of the seed (which signals the initiation of the reaction) to four different growth solutions and allowed to grow for ~4 h at room temperature. A control experiment was also performed alongside where Ag^+ was added into the growth solution before the addition of the seed particles (referred to as 0 min sample, cf. Scheme 1).

Synthesis of ETHH and THH Au NCs. To synthesize Au ETHH NCs of varied ARs, identical synthetic conditions were maintained except for the substitution of CTAC with CTAB and delaying the addition of $AgNO_3$ to 1.5, 5, 10, 15, 30, 60, and 90 min as well as performing a control experiment (referred to as 0 min sample) and allowed to grow for ~12 h at room temperature.

SERS Measurements. SERS measurements were carried out using a HoribaJobinYvon LabRAM HR with a 50× objective lens. The excitation wavelength for all the SERS experiments was 633 nm. The excitation was maintained at 0.01% of the maximum power, and the accumulation time for each spectrum was 5 s. 50 μL of an aqueous dispersion of Au NCs obtained after repetitive centrifugation was treated with 50 μL of Nile Blue (NB) (10 μM, in

ethanol) and kept in incubation overnight. The resultant concentration of NB was 5 μM. Subsequently, the samples were drop-cast on glass slides and dried under an incandescent lamp (200 W) for 30 min. Raman spectra were recorded for these samples along with NB (10 mM).

Characterization. UV-vis spectra were recorded from Chemito SPECTRASCAN UV 2600. FE-SEM images were captured through ZEISS Ultra Plus, and TEM images were captured using a JEOL JEM- 2200FS instruments. Average length, width, and ARs of Au NCs of varying sizes were determined using ImageJ software. Additionally, detailed TEM studies were performed using monochromatic TITAN Themis operated at 300 kV (energy resolution ~ 0.3 eV at 300 kV) equipped with a CEOS probe corrector for Cs aberration-corrected STEM at AFMM, IISc Bangalore, and at Radiological Processing Lab, at Pacific Northwest National laboratory (PNNL) using a JEOL grandARM 300 CF scanning transmission electron microscope operated at 300 kV (63 pm spatial resolution) equipped with dual JEOL Centurio energy-dispersive X-ray spectrometers. The XPS data were collected using Thermo Fisher Scientific ESCALAB Xi+. Powder X-ray diffraction (PXRD) patterns were recorded at room temperature from a Bruker D8 ADVANCE diffractometer using Cu Kα radiation (λ = 1.5406 Å). Raman spectra (λ_{exc} = 633 nm) were recorded at a Raman microscope (LabRAM HR, HoribaJobinYvon) with a 50× objective lens.

3.3 Results and Discussion

CCB Au NCs of different ARs were synthesized by the seed-mediated method.[21] It is worth mentioning that concentrations of all the precursors ($HAuCl_4$, CTAC, NaOH, tannic acid (TA), Au NR seed, and $AgNO_3$) are kept identical in each of the systems, the only variable being the time of addition of $AgNO_3$. UV-vis spectra of the Au NCs recorded upon addition of the same amount of $AgNO_3$ at different time intervals during the overgrowth of Au NRs in the presence of CTAC are shown in Figure 3.1a. The extinction spectrum (purple) of CCB Au NCs is characterized by three distinct surface plasmon resonance (SPR) peaks[22] with the longitudinal SPR (LSPR) centered at 751 nm, T2 transverse SPR (TSPR) peak at 653 nm, and T1 TSPR at 563 nm.

Noticeably, upon gradual delay in addition of Ag^+, a continuous blue shift of LSPR peaks finally merging into a single peak centered at 580 nm (red) was indicated the formation of isotropic Au NCs. Figure 3.1c-g demonstrates the final products obtained in the overgrowth of

Au NRs in the presence of CTAC on introducing Ag^+ at different time intervals and a shape yield >90% can be observed. As the delay in introducing Ag^+ increased, the final products become shortened along the long axis with a simultaneous decrease in the AR. When Ag^+ is introduced into the growth solution 30 min after the initiation of the reaction, isotropic concave cube-shaped products with the AR of 1.0 ± 0.1 are formed (Figure 3.1g). If the introduction of Ag^+ into the growth solution is further delayed, irregular-shaped products are formed. TEM images of individual CCB and CC Au NCs provided in Figure 3.1 insets supported the respective UV-vis and FE-SEM data.

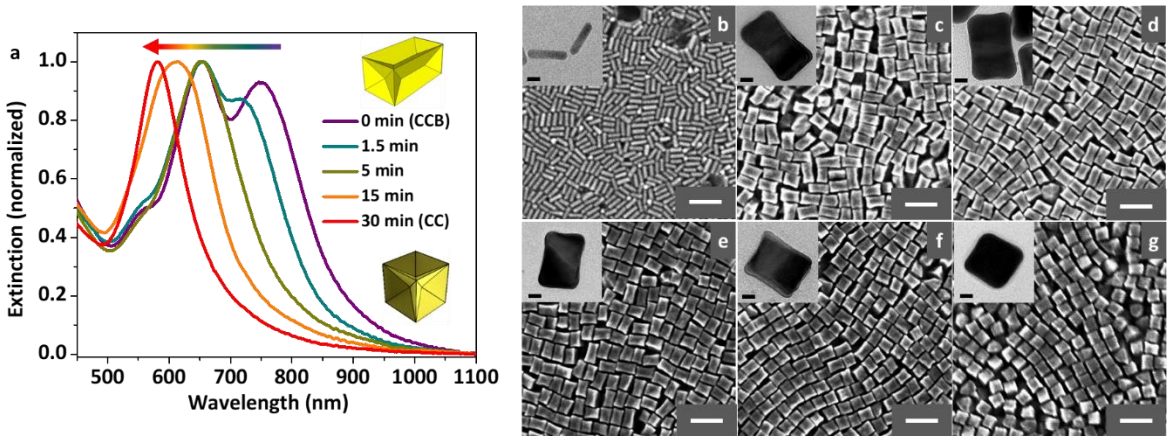

Figure 3.1: (a) UV-vis spectra of Au NRs overgrown in the presence of CTAC under delayed addition of Ag^+ in growth solution leading to a gradual blue shift of the spectra as indicated by the arrow. FE-SEM images of (b) Au NRs used as seeds and (b-f) the final products obtained at different delayed addition of Ag^+ in the overgrowth of Au NRs in the presence of CTAC as 0 min (CCB control), 1.5, 5, 15 and 30 min respectively. Scale bar is 200 nm for all. Inset (b-g): corresponding TEM images; scale bar is 20 nm.

Field-emission scanning electron microscopy (FE-SEM) and transmission electron microscopy (TEM) images showed the monodispersity of the resulting Au CCB NCs (Figure 3.2b, c) when $AgNO_3$ was added before the initiation of the reaction as outlined schematically in Figure 3.2a. The selected area electron diffraction (SAED) pattern on individual NCs reveals that each NC is single crystalline (Figure 3.2d). Additionally, the high-resolution transmission electron microscopy (HRTEM) images reveal the high index facet and curvature associated with such morphology (Figure 3.2e, f). The high-angle annular dark-field scanning transmission electron microscopy (HAADF-STEM) and the corresponding energy-dispersive X-ray spectroscopy

(EDXS) elemental mapping analysis display a complete overlap of Au (green) and Ag (red) elements (Figure 3.2g-j).

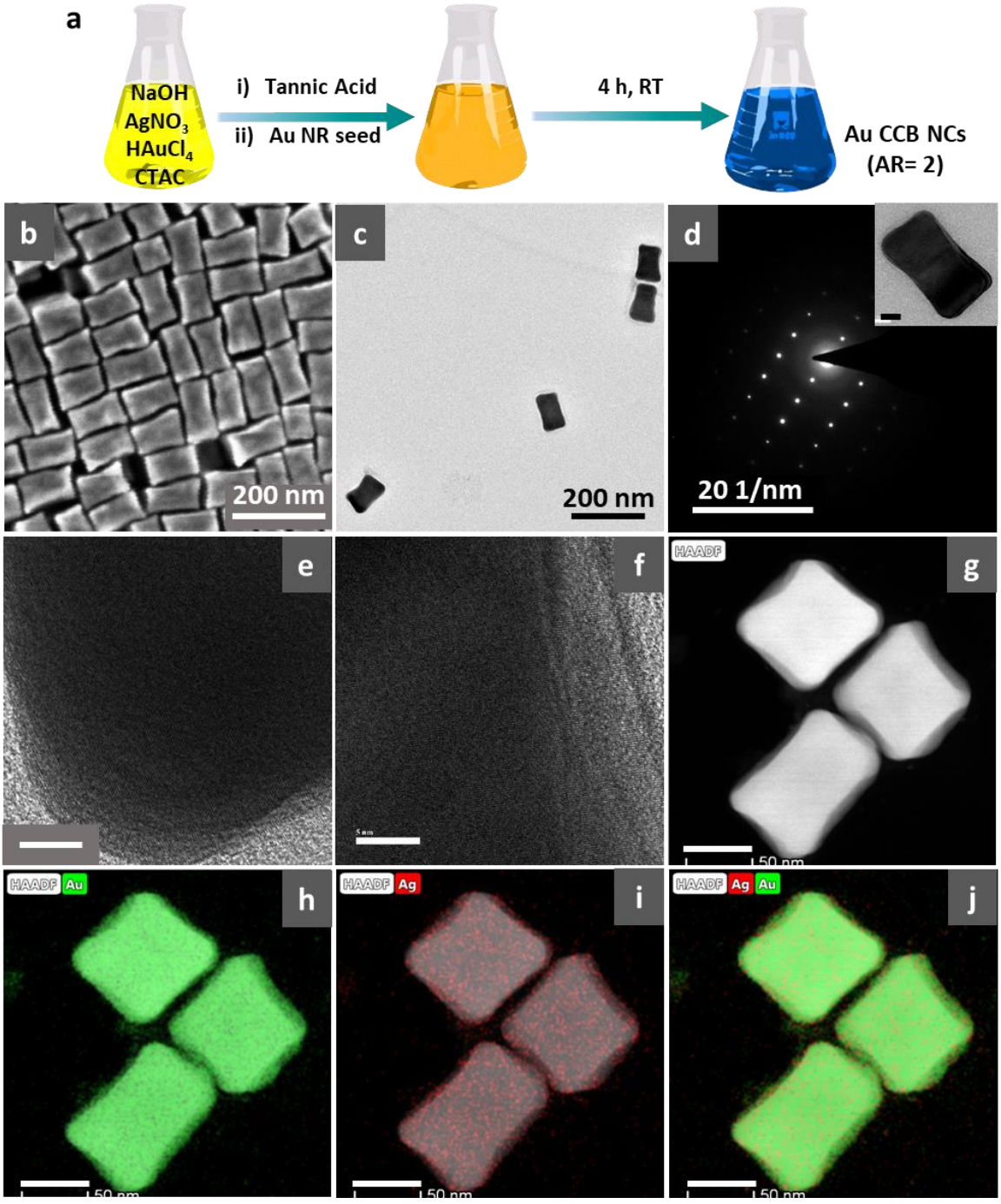

Figure 3.2: (a) Schematic illustration for the synthesis of Au CCB NCs (AR = 2). (b) FE-SEM image; (c) TEM image; (d) SAED pattern (inset: TEM image of an individual Au CCB NC, scale bar is 20 nm); (e,f) HRTEM image (scale bar is 5 nm for all); and (g-j) HAADF-STEM images of Au CCB NCs

in different orientations and the corresponding EDXS elemental mapping of Au (green), Ag (red), and overlay (scale bar is 50 nm for all).

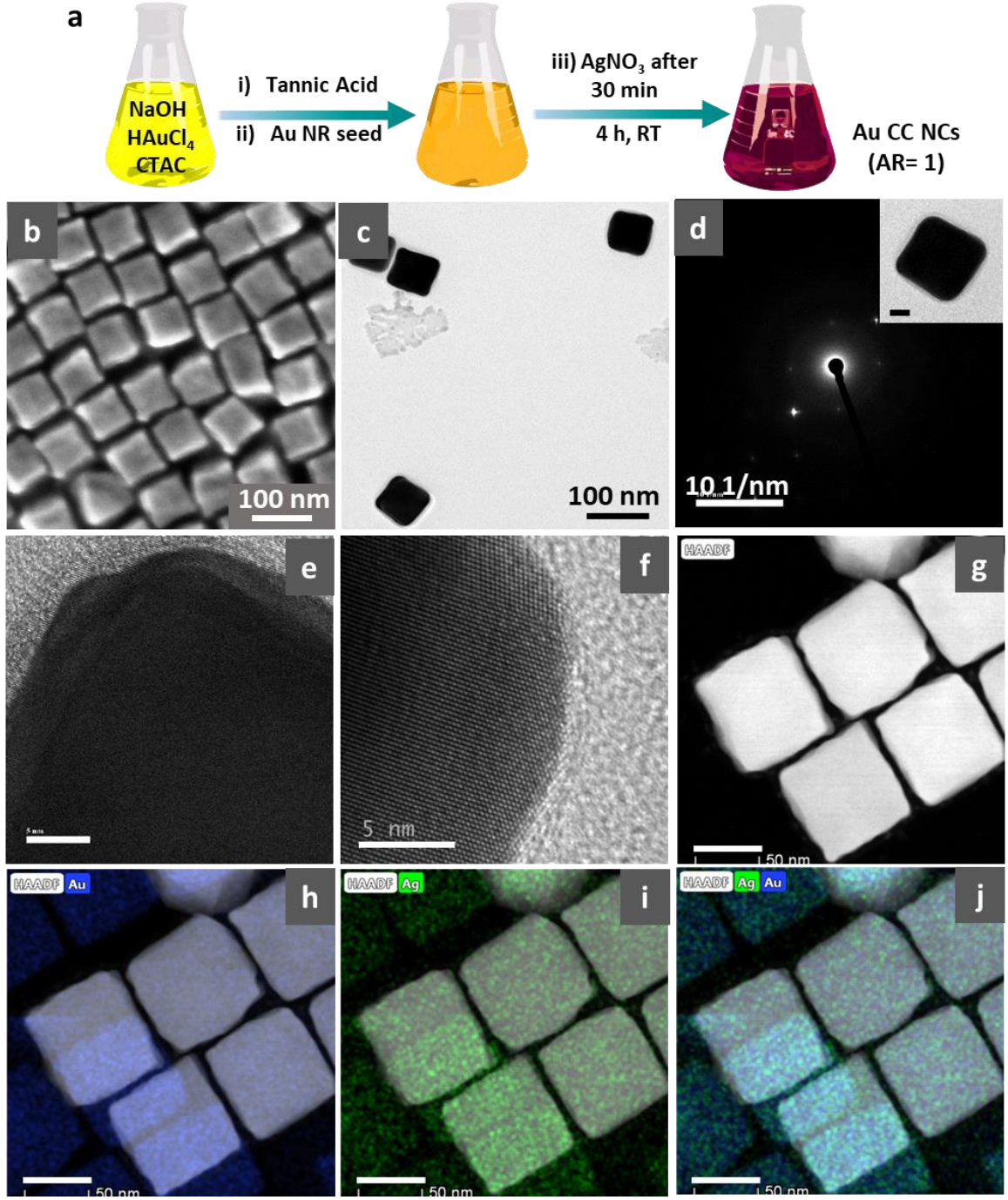

Figure 3.3: (a) Schematic illustration for the synthesis of Au CC NCs (AR = 1). (b) FE-SEM image; (c) TEM image; (d) SAED pattern (inset: TEM image of an individual Au CC NC, scale bar is 20 nm); (e,f) HRTEM image (scale bar is 5 nm for all); and (g-j) HAADF-STEM images of Au CC NCs in

different orientations and the corresponding EDXS elemental mapping of Au (blue), Ag (green), and overlay (scale bar is 50 nm for all).

On the other hand, when $AgNO_3$ was introduced 30 min after the initiation of the reaction, schematically displayed in Figure 3.3a, the FE-SEM and transmission electron microscopy (TEM) images reveal that the resultant Au NCs show a visibly reduced AR (Figure 3.3b, c). From the SAED pattern (Figure 3.3d), it can be noted that the Au CC NCs are single crystalline, corroborated by the HRTEM images (Figure 3.3e, f). The HAADF-STEM image and the corresponding EDXS elemental mapping analysis show the uniform distribution of Au (blue) and Ag (green) (Figure 3.3g-j).

One interesting observation apart from the formation of CC Au NCs from Au NR seeds due to the delayed introduction of Ag^+ is that the volume of the CCB Au NCs (AR = 2.1 ± 0.2) and that of CC Au NCs (AR = 1.0 ± 0.1) remain comparable (Table 3.1). This observation hints at the similar conversion yield of gold, which is not disrupted by the time of addition of Ag^+. This is reasonable considering the fact that the ratio of gold salt to number of seed particles remain the same for all the systems, and hence, a decrease in length is bound to be accompanied by an increase in the width, while maintaining a comparable volume for the Au NCs with different ARs. Table 3.1 summarizes the dimensions, ARs, and LSPR peak maxima of the Au NCs produced by varying the addition time of Ag^+.

Table 3.1: Aspect Ratios (ARs) and LSPR peak positions of various Au NCs obtained with varying the time of addition of $AgNO_3$ in the overgrowth of Au NRs in the presence of CTAC.

Time of Ag addition	Length (L) (nm)	Width (W) (nm)	Aspect Ratio (AR) (L/W)	Longitudinal LSPR (nm)
0 min	111.8 ± 8	54.6 ± 5	2.1 ± 0.2	751
1.5 min	104.5 ± 8	52.4 ± 5	2.0 ± 0.2	720
5 min	100.8 ± 8	54.6 ± 5	1.8 ± 0.2	652
15 min	85.1 ± 7	57.9 ± 4	1.4 ± 0.2	613
30 min	67.6 ± 5	65.5 ± 4	1.0 ± 0.1	580

To understand the mechanism involved in the present observations, aliquots were withdrawn from the growth solutions just before the addition of $AgNO_3$ at different times (5, 15, and 30 min) following the initiation of the growth and monitored by UV-vis spectroscopy and FE-

SEM analysis (Figure 3.4). The UV-vis spectra exhibit a single plasmon peak complementing the corresponding field-emission electron microscopy (FE-SEM) image showing the presence of octahedral (Oct) Au NCs. Drawing upon wider literature on the crystal structure of Au NRs,[6] we assume that in the absence of Ag^+, the unstable {110} planes present at the endcaps grow out more quickly, leading them to disappear while simultaneously resulting in the enlargement of the 4 {111} planes of the endcap. The reasonable outcome of which is the formation of the apex bound by four {111} planes. Thus, to reduce the surface energy, a thermodynamically driven process ensues in the evolution of Au NRs to Au Oct in the absence of Ag^+. The evolution of Au NRs to Au Oct NCs has been observed by various research groups, where the apparently different mechanisms seem to be bound by the difference in growth rates and the minimization of surface energy.[6,23]

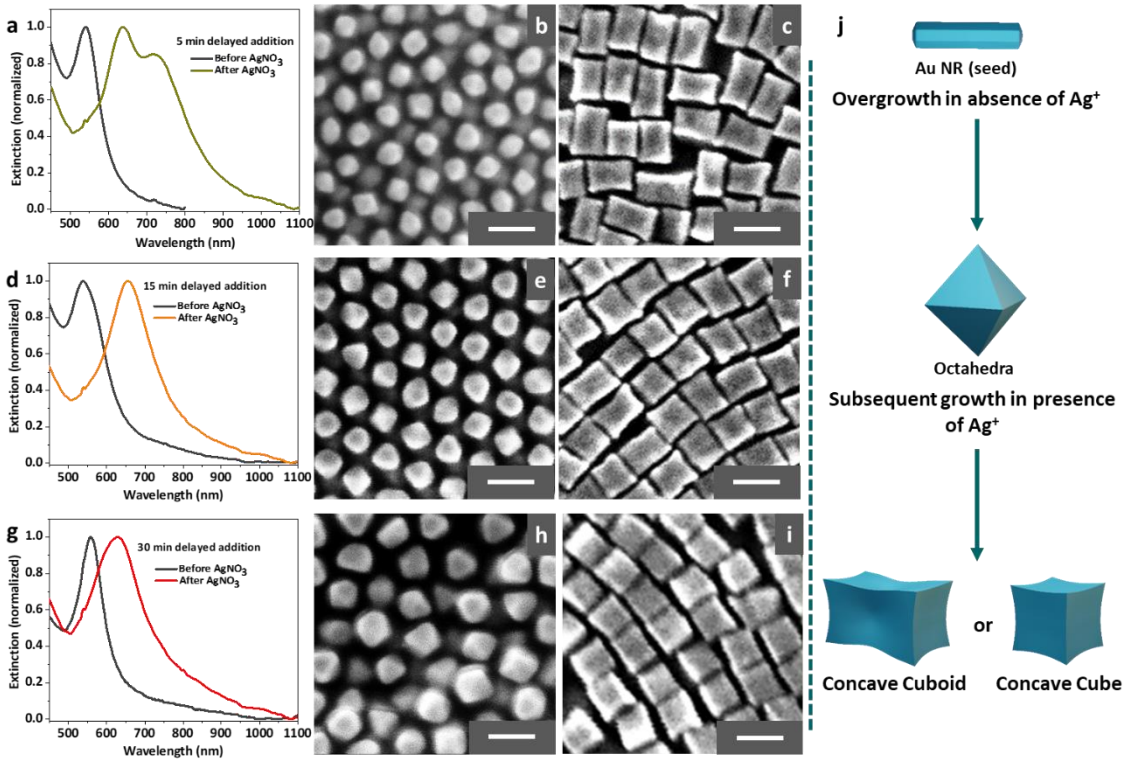

Figure 3.4: (a) UV-vis spectra of Au NRs overgrown in the absence of Ag^+ (grey) for 5 min and the final product obtained after the introduction of Ag^+ 5 min after the initiation of growth (dark yellow); (b,c) corresponding FE-SEM images respectively. (d) UV-vis spectra of Au NRs overgrown in the absence of Ag^+ (grey) for 15 min and the final product obtained after the introduction of Ag^+ 15 min after the initiation of growth (orange); (e,f) corresponding FE-SEM images respectively. (g) UV-vis spectra of Au NRs overgrown in the absence of Ag^+ (grey) for 30 min and the final product obtained

after the introduction of Ag^+ 30 min after the initiation of growth (red); (h,i) corresponding FE-SEM images respectively. Scale bar is 100 nm for all. (j) Schematic outlining the transformation of Au NR to Au Oct NCs in the absence of Ag^+, followed by transformation to Au CCB or CC NC.

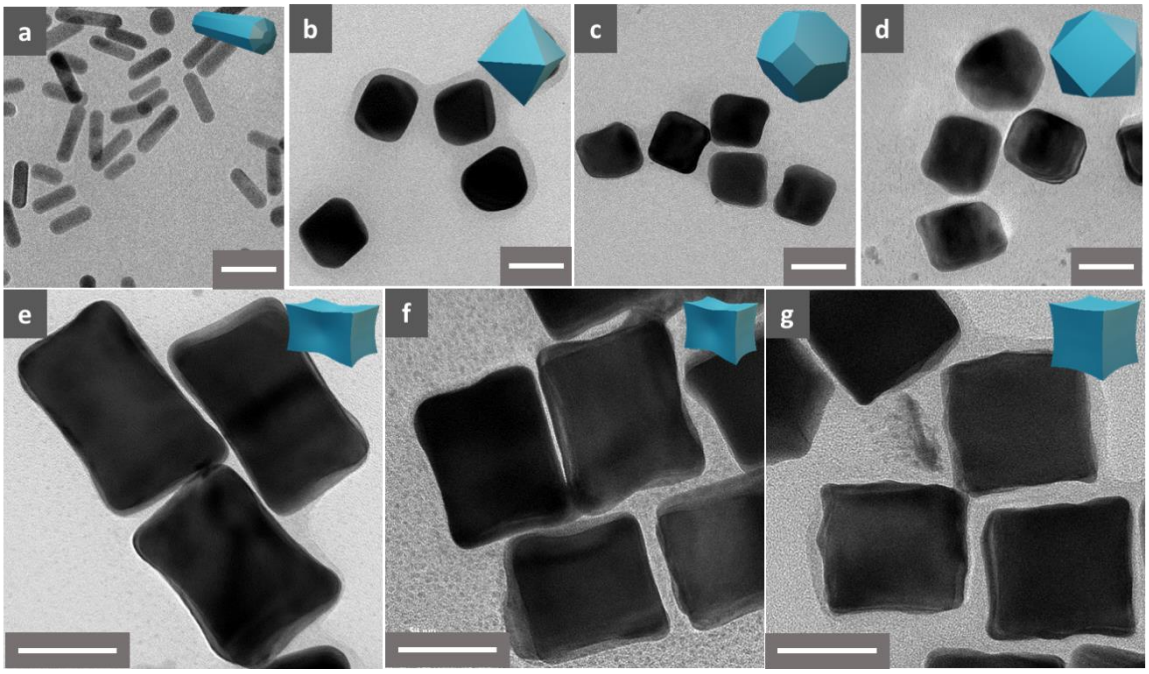

Figure 3.5: TEM images of the morphological evolution of nanoparticles from (a) NR (seeds) to (b) octahedra in the absence of Ag^+ followed by (c) elongation of the octahedral along the corners, 10 min after the addition of Ag^+ to truncated octahedral (d) to result in cuboctahedra 30 min after the addition of Ag^+ to finally result in either (e, f) CCB with reduced ARs or (g) concave cube as the final product. Scale bar is 50 nm for all.

To address how the shape transformation from the Au Oct NCs to the final Au CCB or CC NCs took place, TEM analysis of the aliquots were withdrawn at different time intervals after the addition of Ag^+ into the growth solution (Figure 3.5). From aliquots drawn 10 and 30 min after the addition of Ag^+, the observable shape evolution includes initial elongation along the vertex followed by truncations along the corners to a cuboctahedron-like intermediate. These observations hint at the creation of new surfaces along the corners of the Au Oct NCs, which are then stabilized by Ag^+ present in the solution by virtue of being a more open surface structure. This allows the {111} planes present in the Au Oct NC to grow, resulting in the elongation of the newly created surface to generate the cuboctahedron-like intermediate. The stabilization and restriction of growth of open surfaces in the presence of Ag^+ thus controls the transformation of the Au Oct NCs. As the silver to gold ratio in the reaction mixture determines

the relative growth rate of {100} to {111},[24,25] the introduction of Ag^+ at a later part of the reaction thus tilts the growth direction in favour of {111}, resulting in the gradual transformation from a thermodynamically favoured shape with low-index facets, {111}-faceted Oct Au NCs (having a growth rate along [100] greater than [111]), to a kinetic product (with growth rate along [111] greater than [100]) such as the high-index faceted CCB and CC Au NCs.[15] While the [$AgNO_3$]/ [$HAuCl_4$] ratio controls the growth rate, the length of the final products depends solely on the available amount of Au^+ left in the solution to be reduced. As the introduction of Ag^+ is delayed, the growth rate along [100] dominates in the absence of silver, leading to the formation of Au Oct NCs with progressively increasing dimensions. Thus, when the addition of Ag^+ is gradually delayed into the reaction mixture, there is a progressive decrease in Au^+ for reduction. However, with the high silver to gold ratio now, the growth rate along [111] leads to the transformation of the Au Oct NCs to CCB Au NCs with reduced ARs or CC Au NCs, thereby illustrating how the AR tuning takes place.

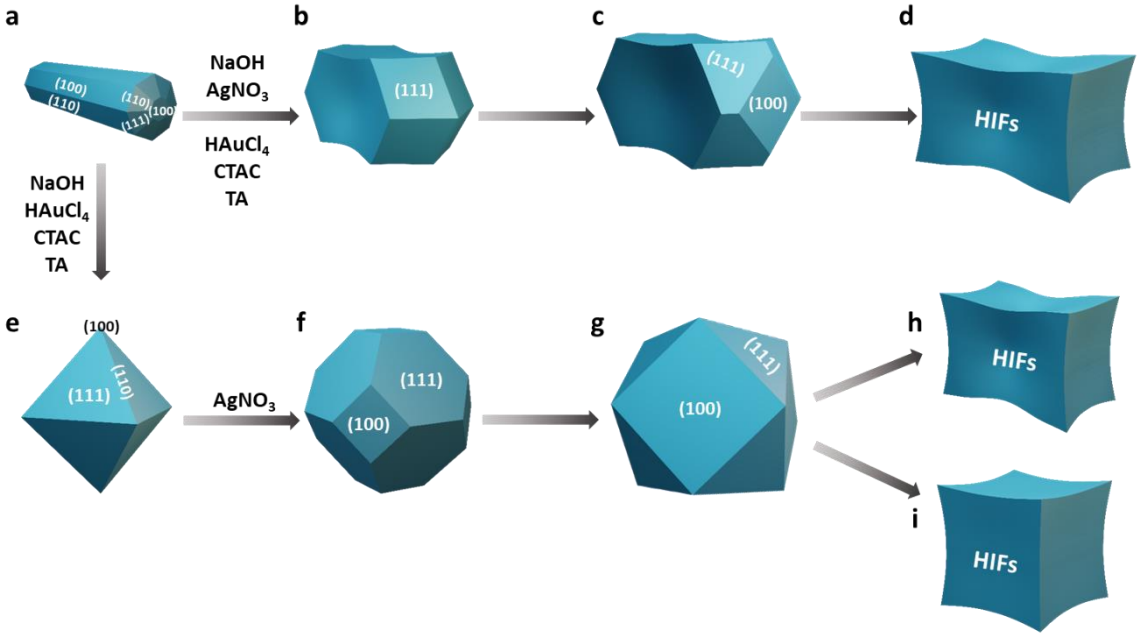

Figure 3.6: (a-d) Schematic of the transformation of Au NRs to Au CCB NCs when Ag^+ is introduced early into the growth solution (0 and 1.5 min); (a, e) schematic representation of the transformation of Au NRs to Au Oct NCs in the absence of Ag^+; and (e-i) subsequent transformation to CCB Au NCs with reduced ARs or CC Au NC via different intermediates.

Based on this proposed mechanism, we have outlined a schematic describing the transformation to the final morphology (Figure 3.6). This mechanism of transformation from

Au Oct to CCB Au NCs with reduced ARs or CC Au NCs complements well the transformation of Au NRs to CCB Au NC reported in our earlier work.[21] When Ag^+ is introduced early into the growth solution (0 or 1.5 min), it is able to stabilize the more open {110} lateral facets of the Au NR, while the low packing density due to the curvature at the ends leads to the deposition of Au^0 resulting in the {111} facets growing at the expense of {110} facets to generate the arrow-headed (AH) intermediate. This intermediate maybe considered as elongated Oct Au NC. The subsequent transformation of the AH intermediate to the truncated CCB Au NCs is analogous to the conversion of the Au Oct NC to the cuboctahedron-like intermediate. This goes on to explain the AR of the final Au NC morphology (Figure 3.6a-d).

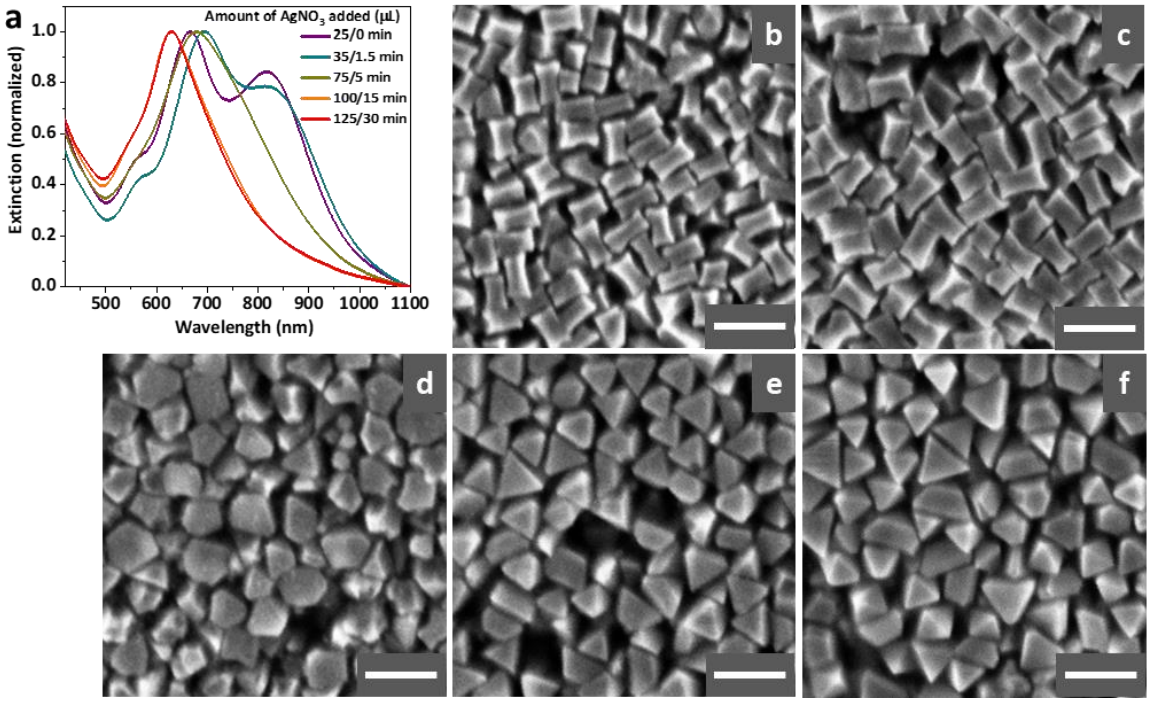

Figure 3.7: (a) UV-vis spectra of Au NRs overgrown in the presence of CTAC under delayed addition of excess Ag^+ in growth solution leading to a gradual blue shift of the spectra. (b-f) FE-SEM images of final products obtained at different delayed addition of excess Ag^+ as 25, 35, 75, 100, 125 μL in the overgrowth of Au NRs in the presence of CTAC as 0 min (CCB control), 1.5, 5, 15, and 30 min respectively. Scale bar is 200 nm for all.

To further highlight the critical role of Ag^+ addition time in the ARs of the resultant Au NC morphology, control experiments were contrived, where the amount of Ag^+ introduced into the growth solution was increased proportionately with the delay in addition. It was observed from the FE-SEM images that introducing higher amounts of Ag^+ to compensate for its delayed

addition gradually resulted in the formation of platelike morphology along with Au Oct NCs (Figure 3.7). The formation of {111}-faceted Au Oct and platelike morphology is due to the ability of {111} facets to support the densest Ag coverage, which makes the stabilization of such planes at high Ag^+ concentration highly favourable. Thus, when high Ag^+ is introduced into the growth solution, Ag UPD stabilizes the {111} facets resulting in the observed morphologies. These data provide evidence that delaying the addition of Ag^+ into the growth solution cannot be counterbalanced by adding excess amounts of Ag^+.

Additionally, because the same amount of Ag^+ at different time intervals was added to the respective growth solutions, X-ray photoelectron spectroscopy (XPS), a surface-sensitive quantification technique, was used to determine the distribution of Ag present in the resultant Au NCs. Following a reported method for determining the ratio of Ag/Au for the Au NCs from XPS data,[14] we observe, in accordance with the literature, that higher energy surface facets are indeed stabilized by a higher Ag coverage (Figure 3.8). The Ag/Au ratio for the high-index faceted Au CCB and CC NCs was markedly higher than that of Au NRs used as seeds and matched well with the reported data. It can thus be inferred that Ag UPD stabilized the resulting Au NCs bound by high-index facets. The addition time of Ag^+, notwithstanding, the final Au NC morphologies are a product of Ag UPD. The lowering of the Ag/Au ratio with the lowering of ARs can be attributed to the gradual decrease of the edge dimensions of the resultant Au NCs.

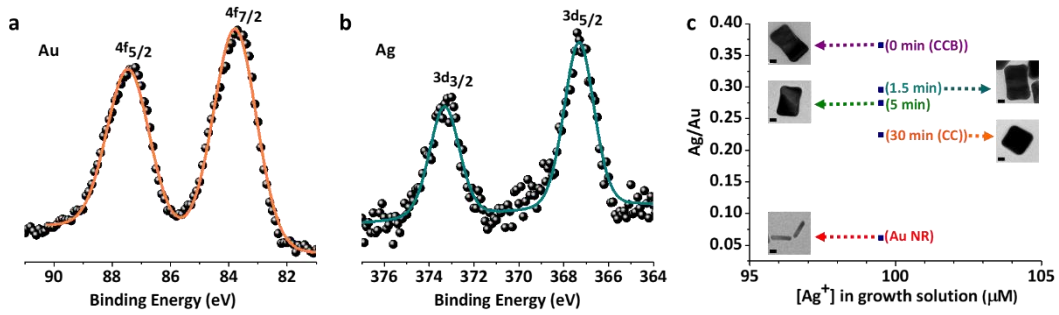

Figure 3.8: (a, b) Representative Au 4f and Ag 3d XPS spectra (0 min sample). (c) Ag/Au ratio extracted from XPS spectra for the final Au NC morphologies obtained by delaying the addition of Ag^+ into the growth solution along with Au NRs used as seeds.

In order to validate that the findings are not exclusive to Au CCB, we have successfully extended the study to the convex counterpart of CCB-ETHH (refer to Materials/Method

for details).[26] Compared to CCB Au NCs, ETHH Au NCs exhibit a slower growth kinetics. To study the effect, thus, the delay in the addition of Ag^+ to the growth solution was extended till 90 min. As was expected, the variation of the AR with the delay in adding Ag^+ to the growth solution of ETHH Au NCs was consistent to what was observed earlier for the case of CCB Au NCs. Similar trends are apparent in the continuous blue shift of the longitudinal LSPR of ETHH Au NCs in their UV-vis spectra (Figure 3.9). Thus, the LSPR at 732 nm finally culminates into a single SPR peak centered at 576 nm, with the delayed addition of Ag^+, indicative of the decreasing AR (Figure 3.9). The corresponding FE-SEM images (Figure 3.9c-j) display a progressive decrease along the length of the ETHH Au NCs, which is reflected in the decreased AR to finally result in THH Au NCs, agreeing well with the UV-vis data. TEM analysis-supported UV-vis and FE-SEM data and respective TEM images of individual ETHH and THH Au NCs are provided in Figure 3.9 insets. Additionally, Table 3.2 summarizes the statistical data of the products synthesized by varying the time of addition of Ag^+ in the growth solution of ETHH Au NCs.

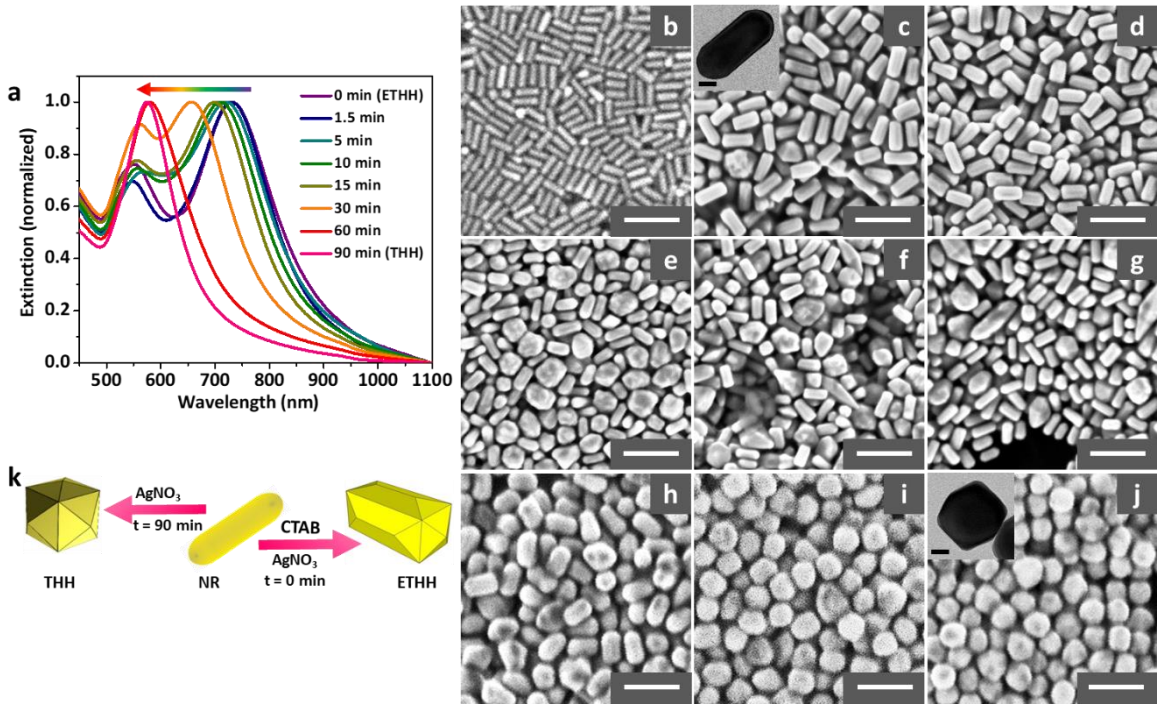

Figure 3.9: (a) UV-vis spectra of Au NRs overgrown in the presence of CTAB under delayed addition of Ag^+ in growth solution leading to a gradual blue shift of the spectra as indicated by the arrow. FE-SEM images of (b) Au NRs used as seeds and (c-j) the final products obtained at different delayed addition of Ag^+ in the overgrowth of Au NRs in the presence of CTAB as 0 min (ETHH

control), 1.5 min, 5, 10, 15, 30, 60 and 90 min respectively. Scale bar is 200 nm for all. Inset (c, j): TEM images of ETHH and THH respectively; scale bar is 20 nm. (k) Schematic representation outlining the structure of Au NR and the subsequent effect of timed addition of Ag^+.

Table 3.2: Aspect Ratios (ARs) and LSPR peak positions of various Au NCs obtained with varying the time of addition of $AgNO_3$ in the overgrowth of Au NRs in the presence of CTAB.

Time of Ag addition	Length (L) (nm)	Width (W) (nm)	Aspect Ratio (AR) (L/W)	Longitudinal LSPR (nm)
Control	100.9 ± 4.8	39.6 ± 4.4	2.6 ± 0.1	716
1.5 min	94.3 ± 6.7	38.2 ± 4.3	2.5 ± 0.4	690
5 min	83.2 ± 7.3	33.8 ± 5.1	2.4 ± 0.4	660
10 min	82.9 ± 7.3	34.3 ± 3.2	2.4 ± 0.3	646
15 min	78.3 ± 9.6	35.3 ± 4.4	2.2 ± 0.4	633
30 min	88.2 ± 4.2	57.7 ± 7.2	1.5 ± 0.2	589
60 min	59.4 ± 7.4	49.0 ± 6.2	1.2 ± 0.2	583
90 min	74.4 ± 4.8	69.1 ± 6.5	1.1 ± 0.1	579

These findings thus emphasize the importance of timing of the addition of Ag^+ to the growth solution of Au NCs to tune their ARs. The plot shown in Figure 3.10 clearly shows how the change in the AR occurs with the time of addition of Ag^+ for both the Au NC systems and the gradual lowering of ARs with delayed addition of Ag^+ is evident. Because ARs of Au NCs are an important parameter controlling their optical property, this route helps to precisely tune them, while maintaining the uniformity and high yield of the products.

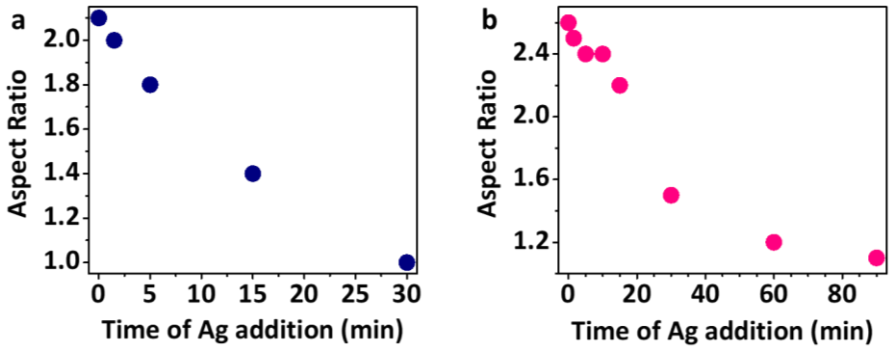

Figure 3.10: Plot of aspect ratio vs time of addition of Ag^+ in the growth solution since the initiation of reaction for (a) CCB Au NCs and (b) ETHH Au NCs.

The Au NCs obtained by varying the time of addition of Ag^+ in the growth solution, viz, Au CCB NCs (AR = 2) and Au CC NCs (AR = 1), were further exploited as the SERS substrate due to the presence of high-index facets, sharp corners, and edges, which can significantly enhance the magnetic field in these areas. [27] To realize the same, Nile Blue dye was used as the probe molecule. The comparative Raman spectra shown in Figure 3.11 exhibit a prominent peak at ~594 cm^{-1} (marked with asterisks) ascribed to C-C-C and C-N-C deformations,[28] used to estimate the signal enhancement. The analytical enhancement factors (AEFs) of NB on CCB and CC Au NCs were calculated to be 3.79×10^5 and 4.24×10^5, respectively, with 633 nm excitation (refer to Table 3.3 for quantitative analysis). The electromagnetic mechanism was predominantly responsible for the large AEF values, and the enhanced signals can be attributed to the generation of a higher number of hotspots near the sharp particle tips and curvature associated with both the morphologies.[29]

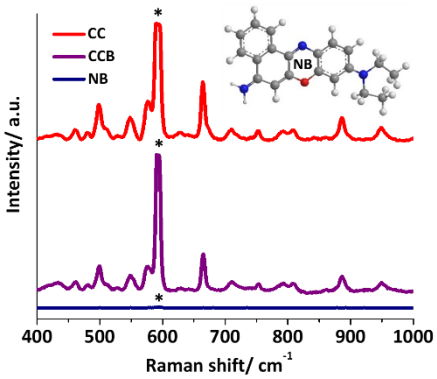

Figure 3.11: Raman spectra of NB (blue) and of NB on CCB (purple) and CC (red) Au NCs. Enhancement factors have been estimated with respect to peak ~594 cm^{-1} denoted by asterisks; inset: molecular scheme of NB.

Table 3.3: Quantitative analysis and calculation of AEF of NB on Au NCs of varying ARs.

Sample	I_{SERS} of 594 cm^{-1}	C_{SERS} (M)	I_{RS} (NB)	C_{RS} (M)	I_{SERS}/I_{RS}	AEF= $I_{SERS}/I_{RS}*C_{RS}/C_{SERS}$
CCB	4.059×10^5	5×10^{-6}	2141	10^{-2}	189.58	3.79×10^5
CC	4.539×10^5	5×10^{-6}	2141	10^{-2}	212.00	4.24×10^5

C_{RS} is the concentration of the probe molecule producing Raman signal I_{RS} under non-SERS conditions, and C_{SERS} is the concentration of the same probe molecule on a SERS substrate at a different concentration giving SERS signal I_{SERS} under similar experimental conditions.[30]

3.4 Summary and Conclusions

In summary, we have shown how the timing of the addition of Ag^+ to the growth solution is a key factor in controlling the ARs of Au NCs apart from the concentration of Ag^+. Starting with identical precursor concentrations, Au NCs with widely tunable ARs could be achieved simply by varying the time of addition of identical concentrations of Ag^+. In doing so, we have also shown the generation of isotropic CC Au NCs and THH Au NCs from anisotropic Au NRs used as seeds in the presence of CTAC and CTAB, respectively, a remarkable observation in the field. A detailed study of the growth process, before and after the addition of Ag^+, has been implemented, where we proposed that the difference in the AR of the resultant Au NCs was not due to the different intermediates from which they were growing, rather, it depended on the Au ion available in the solution for reduction. The introduction of Ag^+ modulated the Ag/Au ratio, thereby controlling the growth direction and thus the final morphology. Moreover, we have verified that the delay in adding Ag^+ into the growth solution cannot be compensated by introducing excess Ag^+. While reinforcing the principles of the seed-mediated growth method in practice, the current work also puts forward a new mechanistic understanding to explain how the same concentration of Ag^+ can be used to tune the ARs of Au NCs. We have demonstrated the findings on two Au NC systems (CCB to CC and ETHH to THH) as a proof of the generality of our concept, and we expect that the same knowledge will provide the rational basis for further work to be done in the field. Additionally, Au NCs with different ARs, generated because of the delayed Ag^+ addition in the growth solution, having sharp edges and corners bound by high-index facets giving rise to large hotspots, are promising SERS substrates as evidenced from the enhancement factor ($\sim 10^5$).

3.5 References

(1) Jana, N. R.; Gearheart, L.; Murphy, C. J. Wet Chemical Synthesis of High Aspect Ratio Cylindrical Gold Nanorods. *J. Phys. Chem. B* **2001**, *105*, 4065.

(2) Nikoobakht, B.; El-Sayed, M. A. Preparation and Growth Mechanism of Gold Nanorods (NRs) Using Seed-Mediated Growth Method. *Chem. Mater.* **2003**, *15*, 1957.

(3) Wu, H.-L.; Chen, C.-H.; Huang, M. H. Seed-Mediated Synthesis of Branched Gold Nanocrystals Derived from the Side Growth of Pentagonal Bipyramids and the Formation of Gold Nanostars. *Chem. Mater.* **2009**, *21*, 110.

(4) Wu, H.-L.; Kuo, C.-H.; Huang, M. H. Seed-Mediated Synthesis of Gold Nanocrystals with Systematic Shape Evolution from Cubic to Trisoctahedral and Rhombic Dodecahedral Structures. *Langmuir* **2010**, *26*, 12307.

(5) Yu, Y.; Zhang, Q.; Lu, X.; Lee, J. Y. Seed-Mediated Synthesis of Monodisperse Concave Trisoctahedral Gold Nanocrystals with Controllable Sizes. *J. Phys. Chem. C* **2010**, *114*, 11119.

(6) Xiang, Y.; Wu, X.; Liu, D.; Feng, L.; Zhang, K.; Chu, W.; Zhou, W.; Xie, S. Tuning the Morphology of Gold Nanocrystals by Switching the Growth of {110} Facets from Restriction to Preference. *J. Phys. Chem. C* **2008**, *112*, 3203.

(7) Walsh, M. J.; Barrow, S. J.; Tong, W.; Funston, A. M.; Etheridge, J. Symmetry Breaking and Silver in Gold Nanorod Growth. *ACS Nano* **2015**, *9*, 715.

(8) Zhang, Q.; Jing, H.; Li, G. G.; Lin, Y.; Blom, D. A.; Wang, H. Intertwining Roles of Silver Ions, Surfactants, and Reducing Agents in Gold Nanorod Overgrowth: Pathway Switch between Silver Underpotential Deposition and Gold−Silver Codeposition. *Chem. Mater.* **2016**, *28*, 2728.

(9) Moreau, L. M.; Jones, M. R.; Roth, E. W.; Wu, J.; Kewalramani, S.; O'Brien, M. N.; Chen, B.-R.; Mirkin, C. A.; Bedzyk, M. J. The Role of Trace Ag in the Synthesis of Au Nanorods. *Nanoscale* **2019**, *11*, 11744.

(10) Almora-Barrios, N.; Novell-Leruth, G.; Whiting, P.; LizMarzán, L. M.; López, N. Theoretical Description of the Role of Halides, Silver, and Surfactants on the Structure of Gold Nanorods. *Nano Lett.* **2014**, *14*, 871.

(11) Personick, M. L.; Mirkin, C. A. Making Sense of the Mayhem behind Shape Control in the Synthesis of Gold Nanoparticles. *J. Am. Chem. Soc.* **2013**, *135*, 18238.

(12) Padmos, J. D.; Personick, M. L.; Tang, Q.; Duchesne, P. N.; Jiang, D.-e.; Mirkin, C. A.; Zhang, P. The Surface Structure of Silver Coated Gold Nanocrystals and its Influence on Shape Control. *Nat. Commun.* **2015**, *6*, 7664.

(13) Liu, M.; Guyot-Sionnest, P. Mechanism of Silver(I)-Assisted Growth of Gold Nanorods and Bipyramids. *J. Phys. Chem. B* **2005**, *109*, 22192.

(14) Personick, M. L.; Langille, M. R.; Zhang, J.; Mirkin, C. A. Shape Control of Gold Nanoparticles by Silver Underpotential Deposition. *Nano Lett.* **2011**, *11*, 3394.

(15) Langille, M. R.; Personick, M. L.; Zhang, J.; Mirkin, C. A. Defining Rules for the Shape Evolution of Gold Nanoparticles. *J. Am. Chem. Soc.* **2012**, *134*, 14542.

(16) Walsh, M. J.; Tong, W.; Katz-Boon, H.; Mulvaney, P.; Etheridge, J.; Funston, A. M. A Mechanism for Symmetry Breaking and Shape Control in Single-Crystal Gold Nanorods. *Acc. Chem. Res.* **2017**, *50*, 2925.

(17) Tong, W.; Walsh, M. J.; Mulvaney, P.; Etheridge, J.; Funston, A. M. Control of Symmetry Breaking Size and Aspect Ratio in Gold Nanorods: Underlying Role of Silver Nitrate. *J. Phys. Chem. C* **2017**, *121*, 3549.

(18) Ming, T.; Feng, W.; Tang, Q.; Wang, F.; Sun, L.; Wang, J.; Yan, C. Growth of Tetrahexahedral Gold Nanocrystals with High-Index Facets. *J. Am. Chem. Soc.* **2009**, *131*, 16350.

(19) Li, J.; Wang, L.; Liu, L.; Guo, L.; Han, X.; Zhang, Z. Synthesis of Tetrahexahedral Au Nanocrystals with Exposed High-Index Surfaces. *Chem. Commun.* **2010**, *46*, 5109.

(20) Zhang, J.; Langille, M. R.; Personick, M. L.; Zhang, K.; Li, S.; Mirkin, C. A. Concave Cubic Gold Nanocrystals with High-Index Facets. *J. Am. Chem. Soc.* **2010**, *132*, 14012.

(21) Rajendra, R.; Roy, D.; Tripathi, S.; Ballav, N. Facile Synthesis of Concave Cuboid Au NCs with Precisely Tunable Dimensions and Mechanistic Insight. *Langmuir* **2019**, *35*, 9456.

(22) Huang, Y.; Wu, L.; Chen, X.; Bai, P.; Kim, D.-H. Synthesis of Anisotropic Concave Gold Nanocuboids with Distinctive Plasmonic Properties. *Chem. Mater.* **2013**, *25*, 2470.

(23) Carbó-Argibay, E.; Rodríguez-González, B.; Pacifico, J.; Pastoriza-Santos, I.; Pérez-Juste, J.; Liz-Marzán, L. M. Chemical Sharpening of Gold Nanorods: The Rod-to-Octahedron Transition. *Angew. Chem., Int. Ed.* **2007**, *46*, 8983.

(24) Wang, Z. L. Transmission Electron Microscopy of Shape Controlled Nanocrystals and Their Assemblies. *J. Phys. Chem. B* **2000**, *104*, 1153.

(25) Seo, D.; Park, J. C.; Song, H. Polyhedral Gold Nanocrystals with Oh Symmetry: From Octahedra to Cubes. *J. Am. Chem. Soc.* **2006**, *128*, 14863.

(26) Rajendra, R.; Gangadharan, P. K.; Tripathi, S.; Kurungot, S.; Ballav, N. High-Index Faceted Au Nanocrystals with Highly Controllable Optical Properties and Electro-Catalytic Activity. *Nanoscale* **2016**, *8*, 19224.

(27) Romo-Herrera, J. M.; González, A. L.; Guerrini, L.; Castiello, F. R.; Alonso-Nuñez, G.; Contreras, O. E.; Alvarez-Puebla, R. A. A Study of the Depth and Size of Concave Cube Au Nanoparticles as Highly Sensitive SERS Probes. *Nanoscale* **2016**, *8*, 7326.

(28) Moram, S. S. B.; Byram, C.; Soma, V. R. Gold-Nanoparticle- and Nanostar-Loaded Paper-Based SERS Substrates for Sensing Nanogram Level Picric Acid with a Portable Raman Spectrometer. *Bull. Mater. Sci.* **2020**, *43*, 53.

(29) Shvalya, V.; Filipic, G.; Zavasˇnik, J.; Abdulhalim, I.; Cvelbar, U.ˇ Surface-Enhanced Raman Spectroscopy for Chemical and Biological Sensing Using Nanoplasmonics: The Relevance of Interparticle Spacing and Surface Morphology. *Appl. Phys. Rev.* **2020**, *7*, 031307.

(30) Patra, P. P.; Kumar, G. V. P. Single-Molecule Surface-Enhanced Raman Scattering Sensitivity of Ag-Core Au-Shell Nanoparticles: Revealed by Bi-Analyte Method *J. Phys. Chem. Lett.* **2013**, *4*, 1167.

Wet-Chemical Deposition of Pt on Au NCs: The Ag Lining

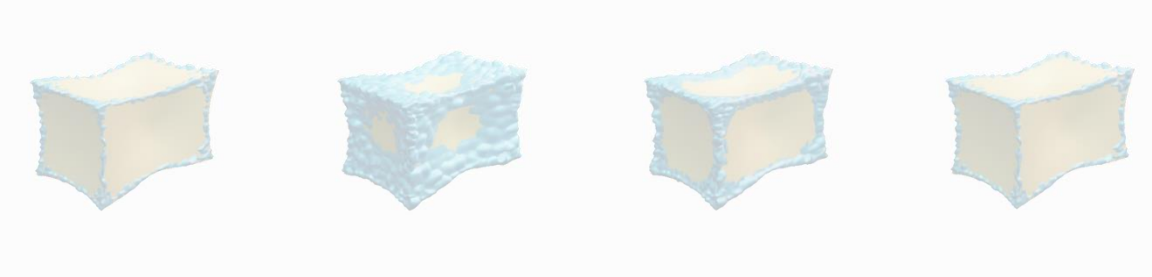

4.1 Introduction

The size-, shape-, and composition-dependent physicochemical properties of bimetallic nanocrystals (NCs) have shown great potential in recent years.[1-5] This has led to extensive research to engineer bimetallic NCs with tailor-made properties for various applications.[6-10] Part of this interest arises from the superior properties over their monometallic counterparts resulting in diversified hybrid materials.[11,12] To this end, a wide range of bimetallic NCs have been reported via different synthetic routes, namely, co-reduction, thermal decomposition, seed-mediated growth, and galvanic replacement, as summarized in detail by Xia and co-workers.[13] Among the abovementioned synthetic routes, seed-mediated methodology, initially reported by Murphy and co-workers for the synthesis of monometallic Au nanorods (NRs) and later extended to bimetallic systems by Xia and co-workers, remains one of the popular routes for the synthesis of bimetallic nanostructures.[14,15] The seed-mediated route offers size control by either preserving the initial seed morphology or transforming to a different morphology besides precise control of shell thickness, giving rise to core-shell, dendritic, and heterostructured NCs.

Compared to other bimetallic core-shell NCs, Au@Pt systems offer the amalgamation of the plasmonic properties of the core (Au) with the catalytic properties of the shell (Pt), resulting in improved catalytic activity and stability compared to the monometallic counterparts, along with the tunability of the optical properties.[16-25] To realize these advantages, the versatile seed-mediated method has been employed to generate simpler bimetallic structures using spherical, rod, cube, octahedral, prism, and star-shaped Au NCs as the core.[26-30] In recent years, Au NCs with high-index facets (HIFs), viz., high density of undercoordinated atoms on the surface, at steps and kinks, were realized as potential seeds for the subsequent deposition of Pt via the seed-mediated growth method. This has resulted in Au@Pt core-shell concave cube, concave cuboid (CCB), and hexoctahedral and tetrahexahedral NCs.[31-34] While the seed-mediated method is a facile route for the precise generation of bimetallic Au@Pt nanostructures, it is, however, always accompanied by tedious multi-step processes. Reducing the time involved in one of these multistep processes offers a promising step in that direction. Also, the mechanistic understanding in view of the role of Ag in the seed-mediated deposition of Pt on Au NCs is intriguing.

In the present study, systematic investigation of the key chemical parameters revealed that the concentration of $AgNO_3$ was an important knob regulating the extent of Pt deposition on Au NCs. While the literature is replete with instances of Ag-assisted Pt deposition where Ag is reported to either direct the preferential site for Pt deposition or simply act as a template for galvanic replacement with Pt,[31,34–36] we however find in the present study that the absence or higher amounts of Ag^+ retarded the deposition of Pt. It is worth to mention that in all these cases, the addition of Ag^+ and Pt precursors was decoupled from one another in the seed-mediated growth method. Although Pt deposition on Au NCs, both in the absence and presence of Ag^+,[33,35,37,38] is well documented, in our work, the effective deposition could be facilitated only in an optimum range of Ag^+. We anticipate that at lower amounts of Ag^+, facile galvanic replacement reaction (GRR) of Ag by Pt leads to a substantial deposition. At higher amounts of Ag^+, faster underpotential deposition (UPD) of Ag than the Pt nucleation on the Au surface leads to insignificant Pt deposition. This brings to fore the mechanistic complexity underlying such reactions involving multiple components. Leveraging on the unique role of Ag, we have devised a new facile synthetic methodology for the controlled deposition of Pt on the edges and corners of Au NCs, whose universality has been demonstrated on two different shaped Au NCs with HIFs-CCB and elongated tetrahexahedra (ETHH). Additionally, to overcome the tediousness associated with multistep seed-mediated methods, we have devised a synthetic route requiring only 7 min for the Pt deposition at an elevated temperature, the lowest time-consuming method among the reported methods[30,35,39–43] which renders the reaction facileness along with a glimpse into the unusual behavior of Ag^+ in directing the deposition of Pt. The Au@Pt NCs with varying Pt deposition were additionally investigated for their activity toward the oxygen reduction reaction (ORR), where the system with highest Pt loading exhibited good activity and enhanced durability when compared to the commercial Pt/C catalyst.

4.2 Materials/Methods

Gold(III) chloride trihydrate ($HAuCl_4 \cdot 3H_2O$), silver nitrate ($AgNO_3$), potassium tetrachloroplatinate(II) (K_2PtCl_4), CTAB, cetyltrimethylammonium chloride (CTAC), tannic acid (TA), and sodium borohydride ($NaBH_4$) were purchased from Sigma-Aldrich. Sodium hydroxide (NaOH; analytical reagent) was bought from RANKEM. All chemicals were used as such. Milli-Q (MQ) water (18.2 MΩ·cm) was used for all experiments.

Deposition of Pt on Au CCB and ETHH NCs. The deposition of Pt on Au CCB and ETHH NCs was carried out by preparing a growth solution containing 440 μL of 0.2 M CTAC, 40 μL of 100 mM NaOH, 10 μL of 4 mM $AgNO_3$, 250 μL of Au CCB NC (Au ETHH NC) seeds, 4 mM K_2PtCl_4 (0-30 μL), and 20 μL of 100 mM TA and a requisite amount of MQ water to make the volume to 1 mL and kept in a water bath maintained at 75 °C for 7 min. To study the effect of $AgNO_3$, the amount was varied from 0 to 30 μL, keeping the amount of K_2PtCl_4 at 30 μL and all other parameters the same.

Measurements on Electrocatalysis. The electrochemical measurements were carried out in a BioLogic electrochemical workstation (SP-300) by using a standard three-electrode setup. A glassy carbon (GC) RDE coated with the catalyst (Pine Instruments Inc.) was used as the working electrode. The ORR activity was evaluated in 0.1 M KOH electrolyte using Hg/HgO as a reference electrode and graphite rod as a counter electrode. The applied potentials were normalized with respect to RHE and the obtained current response was converted to current density by dividing with the geometrical surface area of the working electrode. The catalyst ink was prepared by adding carbon black (Vulcan carbon XC-72) to the catalyst metal alloy solution by fixing the metal:carbon ratio as 40:60 with continued bath sonication for 1 h to get a uniform physical mixture. The catalyst slurry was drop-cast on the GC electrode surface and dried under an IR lamp. Subsequently, 2 μL of 0.01 wt % fumion solution in ethanol was applied to the catalyst, which acts as a binder as well as an ionomer. Platinum, nominally 40% on carbon black was purchased from Alfa Aesar and used as such for comparative studies involving standard Pt/C.

Characterizations. UV-vis spectra were recorded using a Chemito SPECTRASCAN UV 2600. FE-SEM images were captured through a ZEISS Ultra Plus field-emission scanning electron microscope. TEM images and EDXS mapping were captured using a JEOL JEM-2200FS transmission electron microscope. XRD data were recorded at room temperature using a Bruker D8 Advance diffractometer using Cu Kα radiation (λ = 1.5406 Å). The element content in the samples were measured by a Thermo Fisher Scientific, Element XR inductively coupled plasma mass spectrometer.

4.3 Results and Discussion

High-quality CCB and ETHH Au NCs were synthesized according to our earlier synthetic protocols[44,45] and used as seeds in the present study. To induce Pt deposition to a different extent on the surface of the Au NCs, varying amounts of K_2PtCl_4, used as the Pt precursor, were introduced into the growth solution.

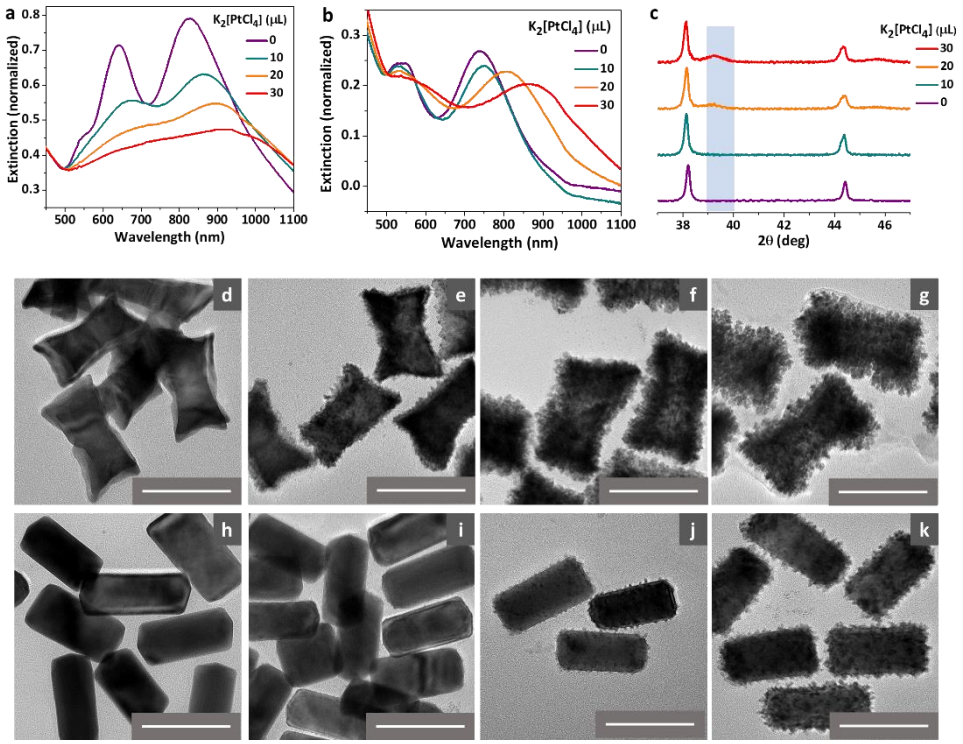

Figure 4.1: (a) UV−vis spectra of Au@Pt CCB NCs synthesized by varying the amount of the Pt precursor K_2PtCl_4 at a constant $AgNO_3$ volume (10 μL). (b) UV−vis spectra of Au@Pt ETHH NCs synthesized by varying the amount of the Pt precursor K_2PtCl_4 at a constant $AgNO_3$ volume (10 μL). (c) XRD patterns of Au@Pt NCs synthesized by varying the amount of K_2PtCl_4. The peak corresponding to Pt(111) has been highlighted in blue shade. (d−g) TEM images of Au@Pt CCB NCs synthesized by varying the amounts of K_2PtCl_4 as 0, 10, 20, and 30 μL, respectively, at a constant $AgNO_3$ volume (10 μL). (h−k) TEM images of Au@Pt ETHH NCs synthesized by varying the amounts of K_2PtCl_4 as 0, 10, 20, and 30 μL, respectively, at a constant $AgNO_3$ volume (10 μL). The scale bar is 100 nm for all.

The three plasmonic peaks are characteristic of Au CCB, attributed to the transverse edge mode, T1, the transverse hybrid mode, T2, and the longitudinal surface plasmon resonance.[46] The synthesized Au CCB NCs exhibit these three distinct plasmonic peaks, and the UV−vis spectra provide evidence to the fact that in the absence of Pt, they remain unchanged. However, the discernible changes on introducing the Pt precursor include the disappearance of the T1

TSPR apart from a slight red shift of the peaks, which indicates preferential deposition of Pt on the edges and corners. The dampened and broader plasmonic peaks observed at higher amount of Pt may be ascribed to the larger absorption via interband transitions.[40,47] The UV−vis spectra thus provide preliminary but strong evidence on the successful deposition of Pt in Au CCB NCs (Figure 4.1a). The UV−vis spectra of Au ETHH NCs, which exhibit two plasmonic peaks, were found to exhibit a trend analogous to that of Au@Pt CCB NCs on increasing the amount of Pt introduced in the growth solution (Figure 4.1b). Further, the powder X-ray diffraction (PXRD) technique was employed to extract detailed structural information of the synthesized Au@Pt NCs. From the X-ray diffraction, apart from (111) and (200) reflections of Au face-centered cubic (fcc) structure at 38.1 and 44.3°, 2θ values at 39.2 and 45.6° could also be indexed into (111) and (200) reflections of Pt fcc structure, respectively, at higher amounts of Pt (20, 30 μL) (Figure 4.1c).[32] The increasing peak intensity of Pt reflects an increase in the shell thickness, corroborating with the UV−vis analyses.

Corroborating the initial observations from the UV−vis spectra, the corresponding transmission electron microscopy (TEM) images of CCB NCs obtained at varying amounts of Pt show the preferential deposition of Pt along the corners and edges (Figure 4.1d−g). The corners and edges of CCB Au NCs with less density of surfactants due to the curved surfaces are associated with high energy, which explains the preference for Pt deposition on them. This explains why we observe denser Pt deposition on Au CCB NCs compared to Au ETHH NCs under similar reaction conditions.

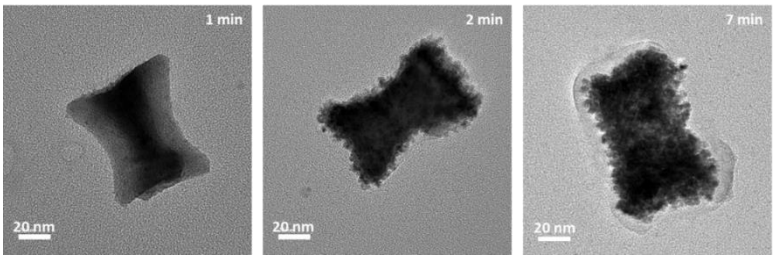

Figure 4.2: (a-c) TEM images of Pt deposition on Au CCB NC to various extent according to the progress of the reaction. Scale bar is 20 nm for all.

With an increasing amount of Pt, the deposition becomes more compact owing to the dense Pt layer. The smooth edges and sharp corners of the Au NCs are thus transformed into uneven surfaces with rounded corners in the Au@Pt NCs. The formation of Pt islands (Volmer−Weber)

instead of a smooth coverage (Frank−van der Merwe) on the surface of the HIF Au NCs arises due to the large lattice mismatch between Au and Pt (~4%) and a high Pt−Pt bond energy.[13] Thus, controlled deposition of Pt while maintaining the morphological integrity of the seed has been successfully realized. The observations were consistently reproduced across different batches as well as different sizes of both Au CCB and Au ETHH NCs. Introducing even higher amount of Pt^{2+} to the growth solution led to complete surface coverage along with loss of initial seed morphology. The present work aimed to control selective deposition; hence, a higher amount variation of Pt was not pursued.

Furthermore, to study the process by which Pt deposition takes place on the Au NCs, aliquots were withdrawn from the growth solution at different time intervals, centrifuged to quench the reaction, and subjected to TEM analysis (Figure 4.2). From the aliquot isolated 1 min after the initiation of the reaction, the corresponding TEM image reveals discrete Pt clusters interspersed along the edges of the Au CCB NC. However, in the aliquot isolated in the subsequent 1 min, a thicker Pt layer around the edges was observed. A dense Pt layer can be observed from the aliquot withdrawn at 7 min after the initiation of the reaction.

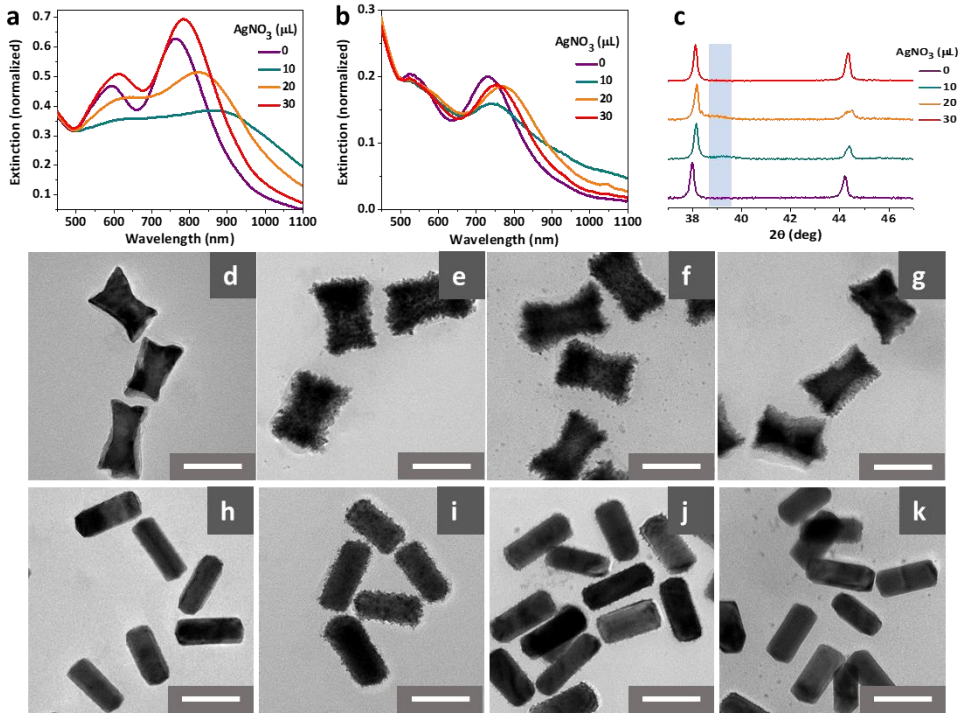

Figure 4.3: (a) UV−vis spectra of Au@Pt CCB NCs synthesized by varying the amount of $AgNO_3$ at a fixed K_2PtCl_4 amount. (b) UV−vis spectra of Au@Pt ETHH NCs synthesized by varying the amount

of $AgNO_3$ at a fixed K_2PtCl_4 amount. (c) XRD patterns of Au@Pt NCs synthesized by varying the amount of $AgNO_3$. The peak corresponding to Pt (111) has been highlighted in blue. (d−g) TEM images of Au@Pt CCB NCs synthesized by varying the amounts of $AgNO_3$ as 0, 10, 20, and 30 μL, respectively, at fixed amounts of K_2PtCl_4 (30 μL). (h−k) TEM images of Au@Pt ETHH NCs synthesized by varying the amounts of $AgNO_3$ as 0, 10, 20, and 30 μL, respectively, at fixed amounts of K_2PtCl_4 (30 μL). The scale bar is 100 nm for all.

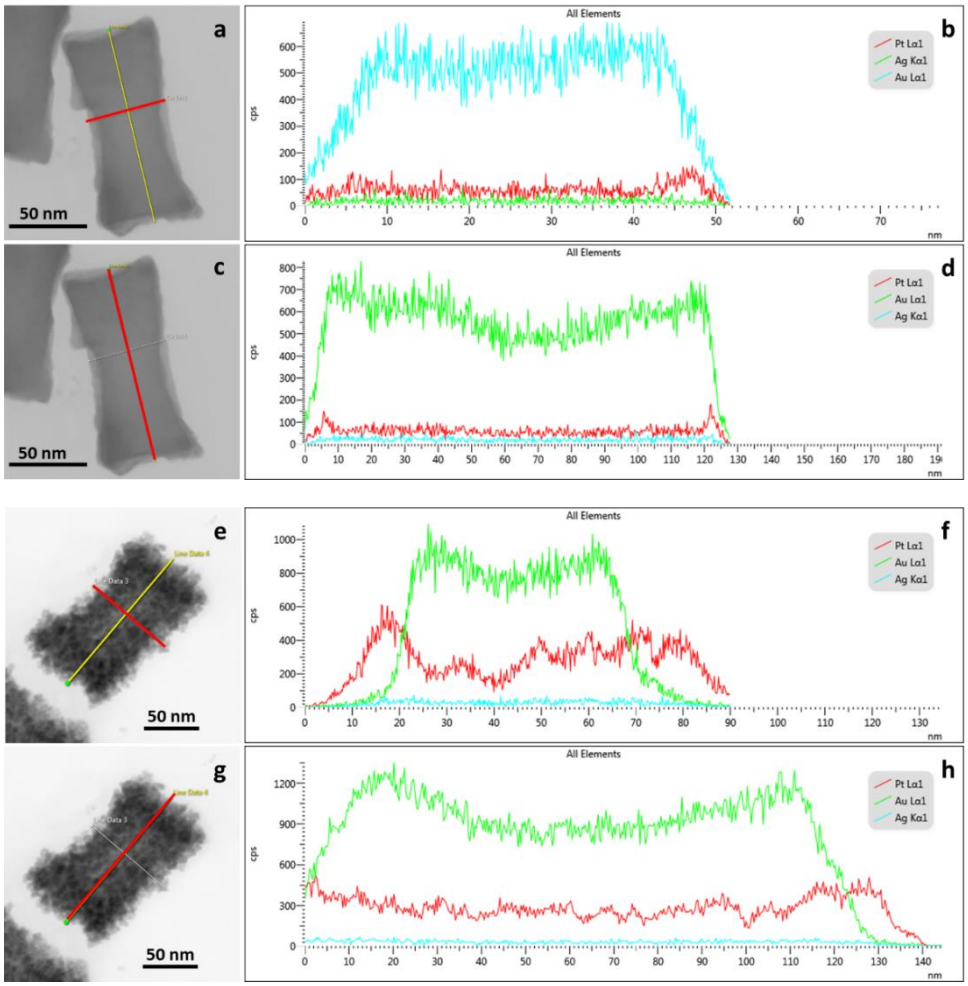

Figure 4.4: (a,c) Scanning transmission electron microscopy (STEM) image of Au@Pt CCB NC (0 μL $AgNO_3$) and (b,d) EDXS line scan profile along the short axis and long axis, respectively. (e,g) STEM image of Au@Pt CCB NC (10 μL $AgNO_3$) and (f,h) EDXS line scan profile along the short axis and long axis, respectively.

Since the Pt−Pt bond energy is higher than the Au−Pt bond energy, the successive Pt deposition on the initial Pt clusters is rapid, giving rise to a compact Pt layer encompassing the Au NC. This results in the desired Au@Pt bimetallic nanostructure without compromising markedly

on the Au seed morphology. The requirement of only 7 min for the successful generation of Au@Pt bimetallic nanostructure happens to be the fastest among the reported seed-mediated methods. Of particular mention is the controlled deposition of Pt on Au nanoprism at room temperature with the time requirement of 1 h, which was attributed to surfactant cetyltrimethylammonium bromide (CTAB) molecules acting as templates for the linear growth pattern.[30] We, therefore, anticipate that under our growth conditions as well, ordered Pt deposition would take place on such Au nanoprism structures in 7 min.

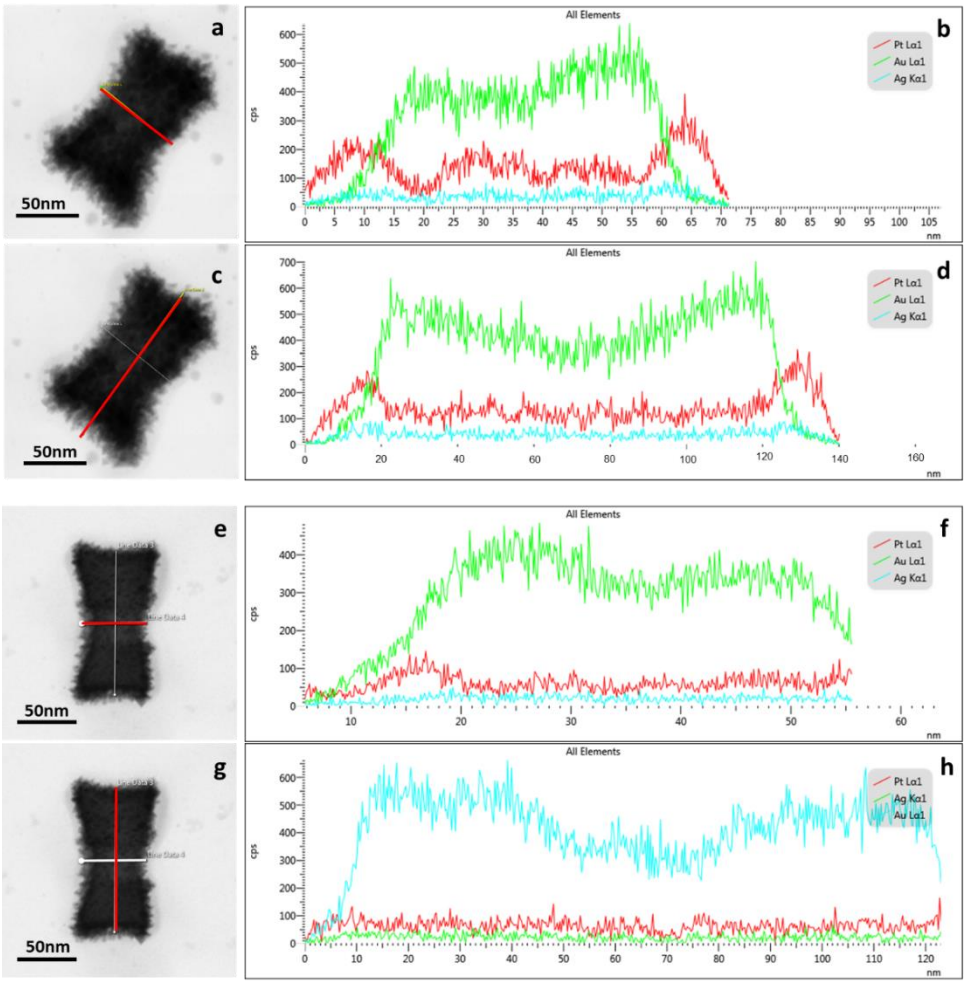

Figure 4.5: (a,c) STEM images of Au@Pt CCB NCs (20 μL $AgNO_3$); (b,d) EDXS line scan profile along the short axis and long axis, respectively. (e,g) STEM image of Au@Pt CCB NC (30 μL $AgNO_3$); and (f,h) EDXS line scan profile along the short axis and long axis, respectively.

On further increasing the amount of $AgNO_3$, an interesting observation was made, whereby the plasmonic peaks not only showed a blue shift but also regained both the plasmonic feature and the peak intensity. This hints at a reduced Pt deposition at higher amounts of Ag^+. While the

literature is replete with the role of Ag^+ in assisting the deposition of Pt on Au surfaces by either acting as a substrate for GRR or guiding the site for Pt deposition,[29,32–34] the current work sheds light on an unlikely behaviour of Ag in Pt deposition on Au NCs, which merits thorough investigation. Although Guo and co-workers mentioned the inhibition to Pt deposition at higher amount of $AgNO_3$ and facile Pt deposition at lower amounts of $AgNO_3$, (i) no experimental proof was presented to attest the same or investigate the extent of Pt deposition and (ii) even under the two aforementioned conditions, the Ag mole ratio was always higher than the Pt ratio.[32] The XRD patterns support the observation where peaks corresponding to Pt are not present at higher amounts and in the absence of Ag^+ (Figure 4.3c). However, the peaks observed at 39.2° 2θ are corresponding to (111) reflections of Pt when a low to moderate amount of Ag^+ was maintained during synthesis. A positive shift in the 2θ value of Au peaks by 0.05 units in cases with more Pt deposition hints at negligible Pt−Au alloying, which had no bearing on the SPR. The corresponding TEM images validate the observations made from the UV−vis spectra where dense coverage of Pt on Au surface was observed at lower amounts of Ag^+ with the coverage of Pt gradually decreasing on further increasing the amount of Ag^+ (Figure 4.3e, i). The TEM images of samples synthesized in the absence and in higher amounts of Ag^+ exhibit a reduced Pt deposition (Figure 4.3d, f–h, j, k). The EDXS line scan profiles show a clear preference for Pt deposition along the edges of the Au core, which decreases as the amount of $AgNO_3$ is increased in the growth solution (Figures 4.4 and 4.5).

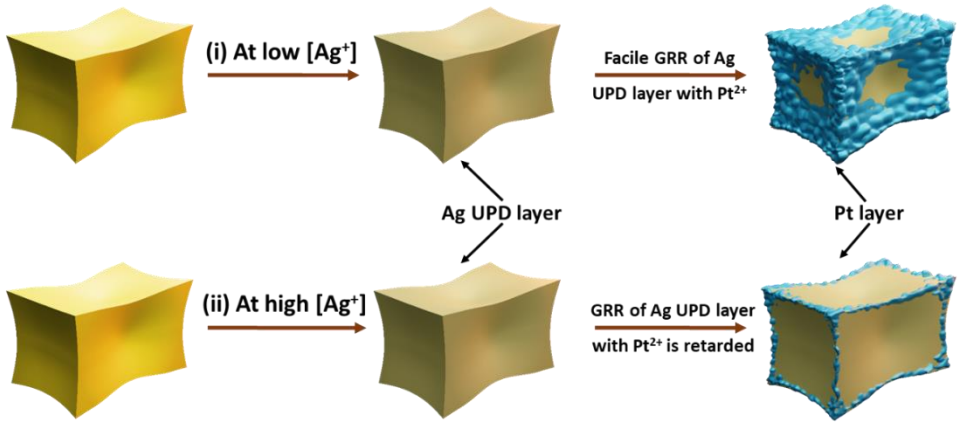

Scheme 4.1: Schematic Representation of the Proposed Mechanism of Pt Deposition under Different Ag^+ Concentrations.

Under the reaction conditions employed, the pH (~6) of the solution is found to be slightly acidic to dissuade the bulk deposition of Ag from taking place. Considering that bulk deposition

of Ag is indeed taking place, the TEM images for the samples synthesized in the absence of Pt should display a contrast likewise an earlier observation[48] -a feature not observed in the present study. Apart from that, the % Ag should be significantly higher as no Pt is present for galvanic exchange reaction to take place, which is not the case realized in the present study. Since the % Ag resulting from UPD on HIF is expected to be higher than that on the low-index facet, it is possible that the corresponding Ag content on Au NCs should be higher. In an earlier observation,[49] the % Ag was found to increase with increased aspect ratios (and hence increased lengths); however, in the present study, the % Ag remains mostly constant, even when higher amounts of Ag^+ are introduced into the solution, indicating that it is the UPD of Ag^+ and not the bulk reduction of Ag^+. Note that the higher % Ag may also arise due to Ag-assisted synthesis of Au NC with HIFs, followed by Ag-assisted Pt deposition. From the results obtained thus, we propose a plausible mechanism to explain our observations (Scheme 4.1).

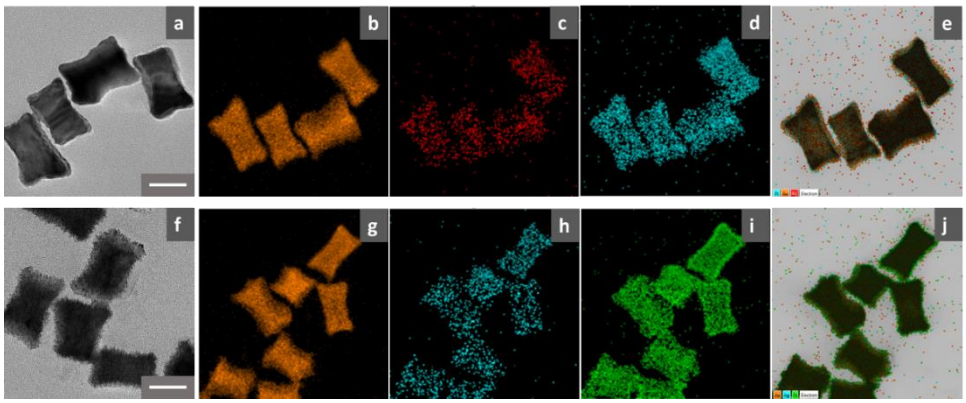

Figure 4.6: (a) TEM image of the Au@Pt CCB NC synthesized using excess Ag^+ (50 μL) under an optimized reaction time (7 min); (b–d) corresponding EDXS maps of Au, Ag, and Pt distributions; (e) overlapped image of Au, Ag, and Pt elements; (f) TEM image of the Au@Pt CCB NC synthesized using excess Ag^+ (50 μL) and subjected to a longer reaction time (20 min); (g–i) corresponding EDXS maps of Au, Ag, and Pt distributions; and (j) overlapped image of Au, Ag, and Pt elements. The scale bar is 50 nm for all images.

The presence of Au core induces the formation of the Ag UPD layer, thereby reversing the order of reduction potentials of Ag and Pt precursors used in the synthesis. Depending on the amount of Ag precursor added during the synthesis, the surface stabilization via Ag UPD varies. At lower Ag^+ concentration, Ag UPD takes place only on corners and edges, which it can sufficiently stabilize. Pt accumulation on the Au NC surface takes place in the following

order: (1) Pt deposition via GRR, (2) diffusion toward higher energy sites, and (3) subsequent nucleation and growth on those sites. The oxidized Ag atoms are further induced to undergo Ag UPD by the exposed Au core and a similar process ensues. However, when higher amounts of Ag^{+} are introduced in the growth solution, the swift and continuous regeneration of the Ag UPD layer before the nucleation of Pt slows down the latter process, thereby accounting for the insignificant Pt deposition on the Au core. To validate the same, control experiments were performed, whereby a higher concentration of Ag^{+} (50 µL) in the growth solution was maintained at a constant Pt^{2+} concentration (30 µL) in two reaction vessels. While the reaction in one vessel was terminated at the optimized time (50 µL Ag; 7 min), it was allowed to continue for an extended time in the other (50 µL Ag; 20 min). From the respective TEM images and the corresponding EDXS mapping, it is observed that Pt deposition is evidently low where the reaction was carried out for optimized duration (Figure 4.6a–e). However, the prominent distribution of the Pt shell is evident when the reaction is extended for a longer time (Figure 4.6f–j).

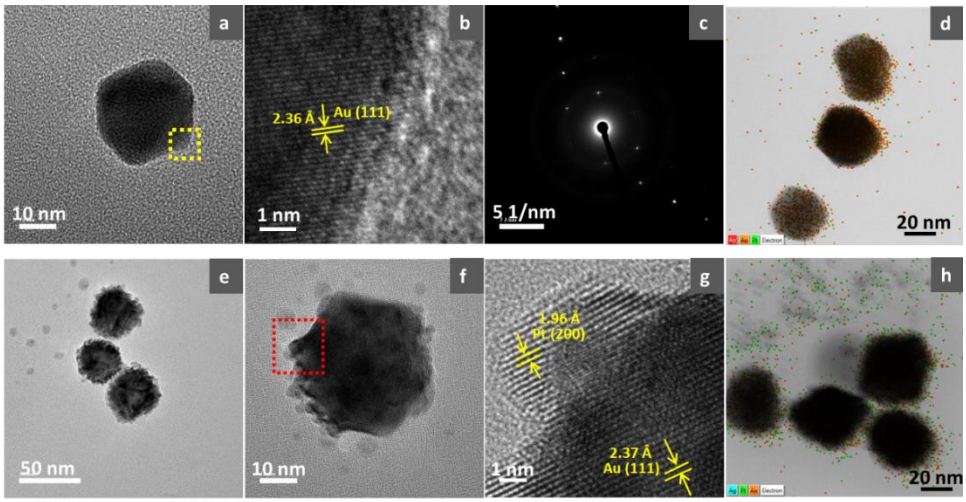

Figure 4.7: (a) TEM images of Au Oct NC subjected to Pt deposition in the absence of Ag^{+}; (b) Magnified High-Resolution-TEM image of the rectangular area marked in (a); (c) Selected-area electron diffraction (SAED) pattern collected from the same particle; (d) Overlapped EDXS mapping image of Au, Ag and Pt elements; (e,f) TEM images of various magnification of Au Oct NC subjected to Pt deposition in the presence of Ag^{+}; (e) Low magnification TEM image showing the distinct deposition of Pt on Au Oct NCs; (g) Magnified High-Resolution-TEM image of the rectangular area marked in (f); (h) Overlapped EDXS mapping image of Au, Ag and Pt elements.

The extent of Pt deposition in the latter case was still lower than that observed when 10 μL of $AgNO_3$ was used for the Pt deposition. This merits our proposed hypothesis that at higher amounts of Ag^+, the continuous regeneration of the Ag UPD is swift, retarding the nucleation and subsequent deposition of Pt. Additionally, to verify that the electrons released due to the oxidation of the Ag layer by GRR facilitated the reduction of the Pt precursor, Ag-free Au octahedral (Oct) NCs were synthesized following a reported protocol.[50] When the Au NCs were subjected to Pt deposition in the absence of Ag^+, no Pt layer formation was found to take place (Figure 4.7a-d). The formation of an inconsequential Pt layer on Au CCB and Au ETHH NCs in the absence of Ag^+ can be explained from the pre-existence of the Ag UPD layer on such HIF nanostructures. However, introducing a small amount of Ag^+ along with the Pt precursor resulted in dense Pt deposition on the Au Oct NCs (Figure 4.7e-h). These two control experiments point to Ag being indispensable for Pt deposition under the current experimental condition. We further attribute our unusual observations to the simultaneous addition of Ag and Pt precursors.

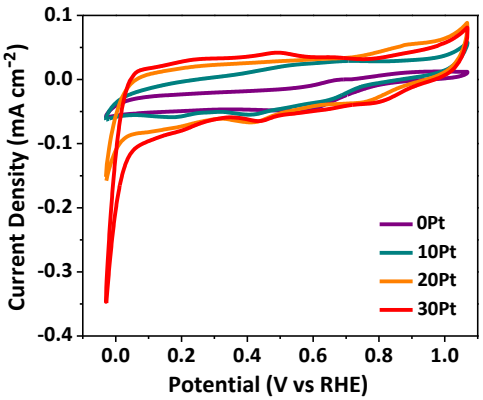

Figure 4.8: CV traces of Au@Pt NCs with variable Pt loading in N_2-saturated 0.1 M KOH at a scan rate of 20 mV/s.

The as-synthesized Au@Pt bimetallic nanostructures with variable Pt loading were further tested for their electrocatalytic activities toward room-temperature ORR by using rotating disc electrode (RDE) and rotating ring disc electrode (RRDE) techniques.[51,52] In a recent review, progress in using advanced Pt-based catalyst systems for ORR activity is nicely summarized given their applications in proton exchange membrane fuel cells.[53] Cyclic voltammogram (CV) traces in N_2-saturated 0.1 M KOH solution for Au@Pt CCB NCs exhibit apparent hydrogen adsorption−desorption in the potential region between 0 and 0.2 V [vs reversible hydrogen electrode (RHE)] for samples having higher Pt loading (20 Pt and 30 Pt), which is absent in the

samples with low/no Pt content (0 Pt and 10 Pt) (Figure 4.8). Figure 4.9a shows the ORR polarization curves in the potential range of 0.0-1.0 V for Au@Pt CCB NCs in oxygen-saturated 0.1 M KOH at a scan rate of 10 mV s^{-1} with an electrode rotation of 1600 rpm at room temperature. The onset potential for the Au@Pt CCB NCs synthesized using 0, 10, 20, and 30 µL of K_2PtCl_4 was observed to be 0.85, 0.88, 0.89, and 0.9 V, respectively. This trend of shifting the onset potential toward higher potential with increased Pt loading indicates better catalytic behaviour for ORR. The higher limiting current density for Au@Pt NCs with the highest Pt loading indicates favourable oxygen adsorption on the stepped surfaces.

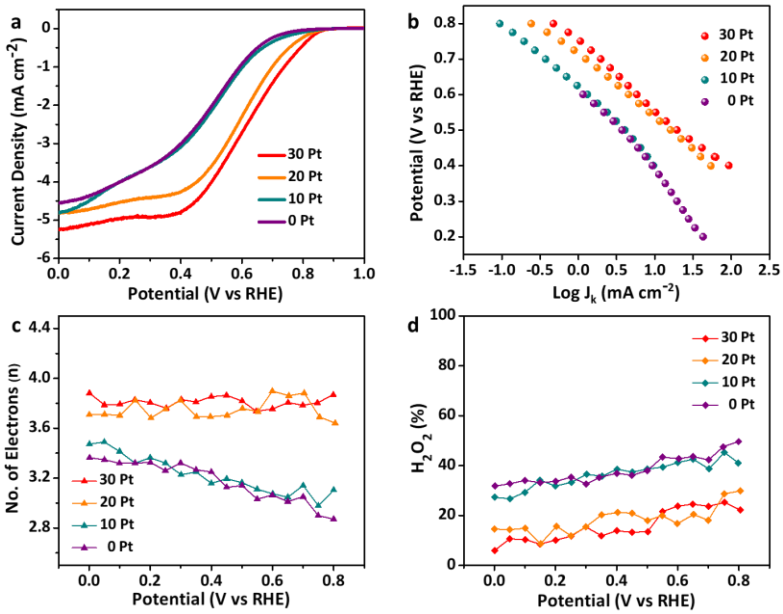

Figure 4.9: (a) LSVs recorded for Au@Pt CCB NCs with variable Pt loading in 0.1 M KOH at an electrode rotation rate of 1600 rpm, (b) Tafel plot comparison of all the catalysts (upon linear fitting of the data points, slopes were estimated to be 354, 292, 244, and 229 mV/decade for the sample synthesized using 0, 10, 20, and 30 µL of K_2PtCl_4), (c) number of electron transfer for ORR calculated from the RRDE analysis, and (d) amount of H_2O_2 calculated as a function of the electrode potential.

Notably, the Au@Pt CCB NCs displayed good stability in the structure during the electrochemical measurements with the structural integrity maintained even after undergoing the ORR (Figure 4.10a). The stability of the catalyst for electrochemical application was investigated by performing an accelerated durability test (ADT). The best performing 30 Pt CCB catalysts are cycled in the oxygen reduction region for 0.60-1.0 V for 5000 potential

cycles with continuous oxygen purging. For comparison, the stability analysis of standardized Pt/C system with commercial composition was also carried out under the same operating conditions. For the 30 Pt CCB catalysts, the linear sweep voltammogram (LSV) recorded before and after ADT cycles displayed a 28 mV shift in the half-wave potential, which is comparatively lower than that obtained in the case of commercial Pt/C (39 mV) (Figure 4.9b-c). Notably, no degradation was observed in the limiting current of 30 Pt CCB after ADT cycles. This points out the high structural integrity achieved in the Au@Pt CCB catalyst by the synergistic electronic interaction between Pt and Au. The Pt/C catalyst could suffer, during potential cycling, from leaching out from the electrode and also agglomeration of Pt particles causing degradation in its performance altogether.

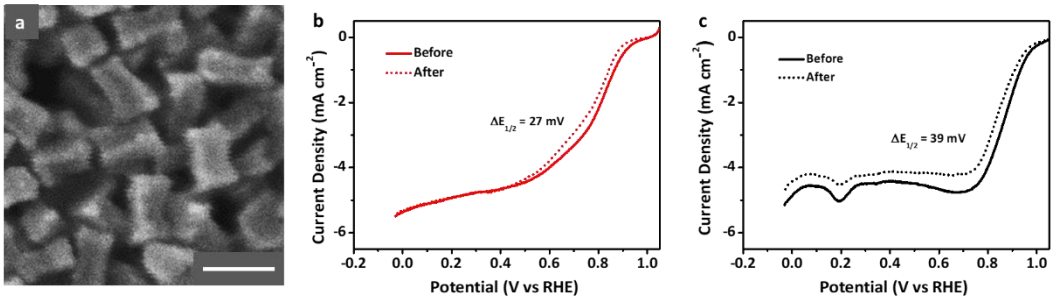

Figure 4.10: (a) FE-SEM image of Au@Pt CCB NC with highest Pt loading (30 μL) having intact structural integrity after undergoing ORR. Scale bar is 100 nm; LSVs of (b) 30 Pt CCB (c) Pt/VC catalysts recorded in 0.1 M KOH at an electrode rotation speed of 1600 rpm before and after the 5000 ADT cycles.

The electrocatalytic performance of our Au@Pt CCB NCs was additionally compared with the standard Pt/C catalyst (Figure 4.11a). While the onset potential for the benchmark catalyst Pt/C was at a higher potential than the best performing Au@Pt CCB NCs, a higher limiting current density was observed for the latter, indicating the greater density of active centers, enabling more oxygen reduction to take place. A lower onset potential for Au@Pt CCB NCs in comparison to the standard Pt/C catalyst may also arise due to the lower loading of Pt in the former. The current output obtained during ORR polarization is normalized with Pt loading to find the influence of Pt in the catalytic performance (Figure 4.11b), and it was observed that the 10 Pt sample with lower Pt content is displaying higher limiting current than 20 Pt and 30

Pt samples. This result validates that, in addition to Pt content, the hybrid Pt−Au electronic structure in the Au@Pt NC systems dictates the overall electrochemical performance.

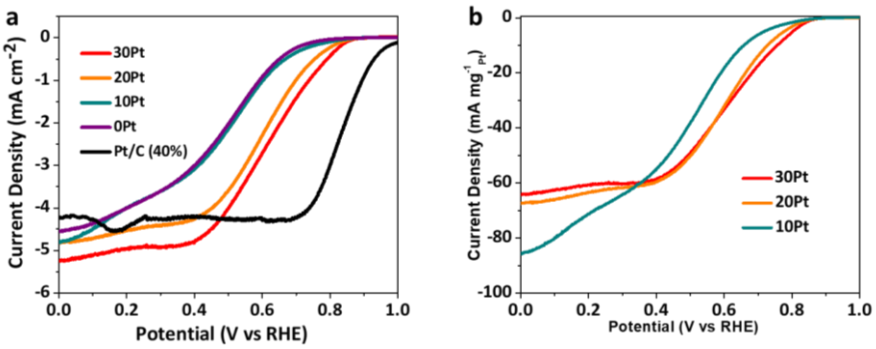

Figure 4.11: (a) LSVs recorded for Au@Pt CCB NCs with variable Pt loading and standard Pt/C in 0.1 M KOH at an electrode rotation rate of 1600 rpm. (b) Pt weight normalized LSVs recorded for Au@Pt CCB NCs with variable Pt loading in 0.1 M KOH at an electrode rotation rate of 1600 rpm.

Au@Pt ETHH NCs varying in their Pt loading when subjected to similar electrochemical measurements also conformed to the trend exhibited by Au@Pt CCB NCs. They, however, showed a superior onset potential of 0.75, 0.94, 0.96, and 0.97 V, respectively, for Au@Pt ETHH NCs synthesized using 0, 10, 20, and 30 µL of K_2PtCl_4 (Figure 4.12a). Further, to compare the intrinsic activity of the NCs with variable Pt loading, the Tafel slope analysis was carried out and the corresponding plots are shown (Figures 4.9b and 4.12b). A low Tafel slope value is associated with faster reaction kinetics with efficient active sites toward ORR.[48] A decrease in Tafel slope value was observed with an increase in Pt loading, indicating the increased feasibility of the reaction for both Au@Pt CCB NCs and Au@ Pt ETHH NCs.

To extract more detailed information on the reaction kinetics of the catalysts, RRDE voltammograms were performed in oxygen-saturated 0.1 M KOH at a scan rate of 10 mVs^{-1} and an electrode rotation rate of 1600 rpm. The percentage of intermediate H_2O_2 generation by the side reaction and the number of electrons (n) transferred during the ORR were derived from the following equations:

$$n = (4I_d) / ((I_d + I_r/N)) \quad (1)$$

$$\% H_2O_2 = (200\ I_r/N)) / ((I_d + I_r/N)) \quad (2)$$

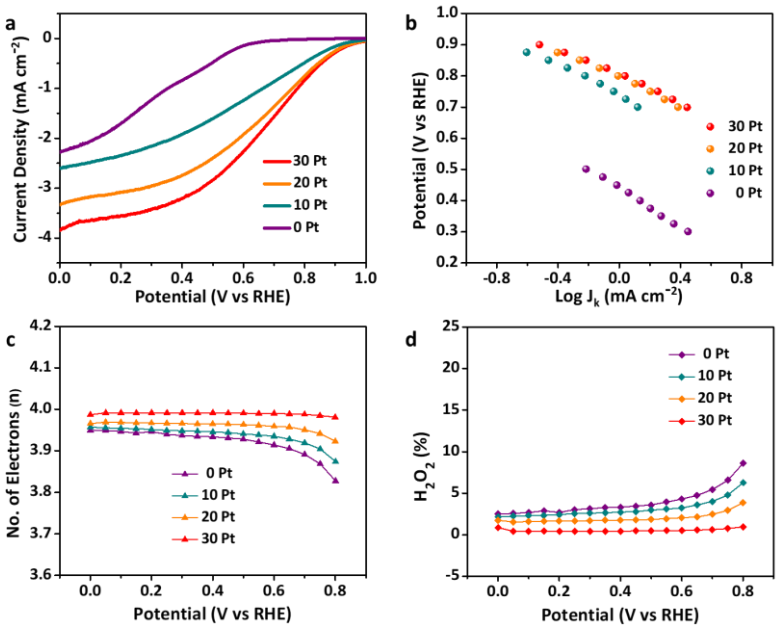

Figure 4.12: (a) LSVs recorded for Au@Pt ETHH NCs with variable Pt loading in 0.1 M KOH at an electrode rotation rate of 1600 rpm, (b) Tafel plot comparison of all the catalysts (upon linear fitting of the data points, slopes were estimated to be 233, 197, 188, and 179 mV/decade for the sample synthesized using 0, 10, 20, and 30 μL of K_2PtCl_4), (c) number of electron transfer for ORR calculated from the RRDE analysis, and (d) amount of H_2O_2 calculated as a function of the electrode potential.

where I_r, I_d, and N are the ring current, disc current, and collection efficiency (0.37), respectively. The number of electrons obtained for Au@Pt CCB NCs are, respectively, 3.81, 3.75, 3.23, and 3.18 while that for Au@Pt ETHH NCs was calculated to be 3.98, 3.96, 3.93, and 3.92, respectively, when the amount of Pt^{2+} was varied as 0, 10, 20, and 30 μL, indicating that the theoretically predicted four-electron pathway was followed (Figures 4.8c and 4.10c). Quantification of the amount of H_2O_2 generated supported the results obtained in the number of electrons calculation where a gradual lowering in the generation of peroxide was observed with increased Pt loading (Figures 4.8d and 4.10d). Thus, the RRDE analysis helped to substantiate the theoretically predicted reduction of the molecular oxygen to water.

The electrochemical active surface area (ECSA) of the best performing 30 Pt CCB catalyst is calculated from CV data and compared with the standard Pt/C catalyst. The CV traces recorded in N_2-saturated 0.1 M KOH showed distinct features of Pt catalytic systems and three regions corresponding to hydrogen adsorption−desorption, oxygen adsorption−desorption, and non-

Faradaic capacitance were identified (Figure 4.11). The ECSA values were calculated using the following equation[54]

$$ECSA = (Q_{H\text{-adsorption}}) / (0.210 \times L_{Pt}) \quad (3)$$

where QH-adsorption is the charge for hydrogen UPD adsorption and L_{Pt} is the mass loading of Pt. The values were found to be ~21.2 and ~39.5 $m^2\ g^{-1}$ for the 30 Pt CCB and the Pt/C catalysts, respectively. The lower ECSA for our catalyst could be due to the blocking of active sites by adhered surfactant molecules on the surface. Based on the overall performance towards ORR in alkaline medium, our Au@Pt CCB and ETHH NC systems appear as promising catalysts for other electrochemical reactions. The use of alkaline medium apart from providing for a less corrosive environment for the catalysts, also enhances the ORR kinetics with respect to the acidic medium.[55]

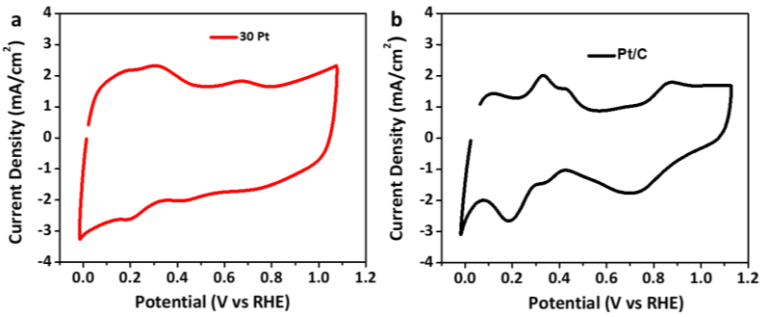

Figure 4.11: CV traces of (a) Au@Pt CCB NCs synthesized using 30 μL K_2PtCl_4 and (b) commercial Pt/C in N_2-saturated 0.1 M KOH at a scan rate of 50 mV/s and electrode rotation rate of 900 rpm.

4.4 Summary and Conclusions

In conclusion, we have demonstrated a facile synthetic route to generate Au@Pt bimetallic nanostructures using CCB and ETHH Au NCs as seeds, which to the best of our knowledge requires the least time for the generation of the Au@Pt bimetallic nanostructure via the seed-mediated route. Optimizing the reaction time to 7 min helped us to unravel an unusual behaviour of Ag^+ in guiding the deposition of Pt. The Pt deposition on the Au surface could be tailored by modulating the Pt or Ag precursor concentration at a fixed reaction duration. A plausible mechanistic explanation has been put forward to explain the unusual observations. The swift regeneration of the Ag UPD layer formed at higher amounts of Ag^+ before the nucleation of Pt on the Au surface slowed down the deposition process, leading to the observed

lower Pt deposition at higher [Ag^+]. The preferential deposition of Pt at the edges and corners of the HIF nanostructures could be attributed to the high surface energy associated with such sites allowing selective Ag coverage, which were further subjected to GRR by Pt. The response to ORR at such low Pt loading circumvents the use of high Pt in monometallic Pt NCs for improved electrocatalytic performance. The generality of the proposed mechanism demonstrated on two Au NCs is expected to be universal for generating other bimetallic nanostructures.

4.5 References

(1) Carbone, L.; Cozzoli, P. D. Colloidal Heterostructured Nanocrystals: Synthesis and Growth Mechanisms. *Nano Today* **2010**, *5*, 449.

aApplications. *Adv. Mater.* **2011**, *23*, 1044.

(3) Chaudhuri, R. G.; Paria, S. Core/Shell Nanoparticles: Classes, Properties, Synthesis Mechanisms, Characterization, and Applications. *Chem. Rev.* **2012**, *112*, 2373.

(4) Liu, X.; Wang, D.; Li, Y. Synthesis and Catalytic Properties of Bimetallic Nanomaterials with Various Architectures. *Nano Today* **2012**, *7*, 448.

(5) Yu, Y.; Zhang, Q.; Yao, Q.; Xie, J.; Lee, J. Y. Architectural Design of Heterogeneous Metallic Nanocrystals−Principles and Processes. *Acc. Chem. Res.* **2014**, *47*, 3530.

(6) Alonso, D. M.; Wettstein, S. G.; Dumesic, J. A. Bimetallic Catalysts for Upgrading of Biomass to Fuels and Chemicals. *Chem. Soc. Rev.* **2012**, *41*, 8075.

(7) Sankar, M.; Dimitratos, N.; Miedziak, P. J.; Wells, P. P.; Kiely, C. J.; Hutchings, G. J. Designing Bimetallic Catalysts for a Green and Sustainable Future. *Chem. Soc. Rev.* **2012**, *41*, 8099.

(8) Wei, Z.; Sun, J.; Li, Y.; Datye, A. K.; Wang, Y. Bimetallic Catalysts for Hydrogen Generation. *Chem. Soc. Rev.* **2012**, *41*, 7994.

(9) Zaera, F. Nanostructured Materials for Applications in Heterogeneous Catalysis. *Chem. Soc. Rev.* **2013**, *42*, 2746.

(10) Zhang, L.; Xie, Z.; Gong, J. Shape-Controlled Synthesis of Au− Pd bimetallic Nanocrystals for Catalytic Applications. *Chem. Soc. Rev.* **2016**, *45*, 3916.

(11) Bracey, C. L.; Ellis, P. R.; Hutchings, G. J. Application of Copper−Gold alloys in Catalysis: Current Status and Future Perspectives. *Chem. Soc. Rev.* **2009**, *38*, 2231.

(12) You, H.; Yang, S.; Ding, B.; Yang, H. Synthesis of Colloidal Metal and Metal Alloy Nanoparticles for Electrochemical Energy Applications. *Chem. Soc. Rev.* **2013**, *42*, 2880.

(13) Gilroy, K. D.; Ruditskiy, A.; Peng, H.-C.; Qin, D.; Xia, Y. Bimetallic Nanocrystals: Syntheses, Properties, and Applications. *Chem. Rev.* **2016**, *116*, 10414.

(14) Jana, N. R.; Gearheart, L.; Murphy, C. J. Wet Chemical Synthesis of High Aspect Ratio Cylindrical Gold Nanorods. *J. Phys. Chem. B* **2001**, *105*, 4065.

(15) Sun, Y.; Yin, Y.; Mayers, B. T.; Herricks, T.; Xia, Y. Uniform Silver Nanowires Synthesis by Reducing $AgNO_3$ with Ethylene Glycol in the Presence of Seeds and Poly (Vinyl Pyrrolidone). *Chem. Mater.* **2002**, *14*, 4736.

(16) Jin, Y.; Shen, Y.; Dong, S. Electrochemical Design of Ultrathin Platinum-Coated Gold Nanoparticle Monolayer Films as a Novel Nanostructured Electrocatalyst for Oxygen Reduction. *J. Phys. Chem. B* **2004**, *108*, 8142.

(17) Zhou, S.; McIlwrath, K.; Jackson, G.; Eichhorn, B. Enhanced CO Tolerance for Hydrogen Activation in Au− Pt Dendritic Heteroaggregate Nanostructures. *J. Am. Chem. Soc.* **2006**, *128*, 1780.

(18) Zhang, J.; Sasaki, K.; Sutter, E.; Adzic, R. R. Stabilization of Platinum Oxygen-Reduction Electrocatalysts using Gold Clusters. *Science* **2007**, *315*, 220.

(19) Kristian, N.; Wang, X. Pt Shell−Au Core/C Electrocatalyst with a Controlled Shell Thickness and Improved Pt Utilization for Fuel Cell Reactions. *Electrochem. Commun.* **2008**, *10*, 12.

(20) Kristian, N.; Yan, Y.; Wang, X. Highly Efficient Submonolayer Pt-decorated Au Nano-Catalysts for Formic Acid Oxidation. *Chem. Commun.* **2008**, 353.

(21) Wang, S.; Kristian, N.; Jiang, S.; Wang, X. Controlled synthesis of Dendritic Au@Pt Core−Shell Nanomaterials for Use as an Effective Fuel Cell Electrocatalyst. *Nanotechnology* **2008**, *20*, 025605.

(22) Kim, Y.; Hong, J. W.; Lee, Y. W.; Kim, M.; Kim, D.; Yun, W. S.; Han, S. W. Synthesis of AuPt Heteronanostructures with Enhanced Electrocatalytic Activity toward Oxygen Reduction. *Angew. Chem., Int. Ed.* **2010**, *49*, 10197.

(23) Wang, L.; Yamauchi, Y. Autoprogrammed Synthesis of Triple Layered Au@ Pd@Pt Core− Shell Nanoparticles Consisting of a Au@Pd Bimetallic Core and Nanoporous Pt shell. *J. Am. Chem. Soc.* **2010**, *132*, 13636.

(24) Yamauchi, Y.; Tonegawa, A.; Komatsu, M.; Wang, H.; Wang, L.; Nemoto, Y.; Suzuki, N.; Kuroda, K. Electrochemical Synthesis of Mesoporous Pt−Au Binary Alloys with Tunable Compositions for Enhancement of Electrochemical Performance. *J. Am. Chem. Soc.* **2012**, *134*, 5100.

(25) Lou, W.; Ali, A.; Shen, P. K. Recent Development of Au arched Pt Nanomaterials as Promising Electrocatalysts for Methanol Oxidation Reaction. *Nano Res.* **2021**, 1−20.

(26) Guo, S.; Li, J.; Dong, S.; Wang, E. Three-dimensional Pt-on-Au Bimetallic Dendritic Nanoparticle: One-Step, High-Yield Synthesis and its Bifunctional Plasmonic and Catalytic Properties. *J. Phys. Chem. C* **2010**, *114*, 15337.

(27) Cui, Q.; Shen, G.; Yan, X.; Li, L.; Möhwald, H.; Bargheer, M. Fabrication of Au@Pt Multibranched Nanoparticles and their Application to In-Situ SERS Monitoring. *ACS Appl. Mater. Interfaces* **2014**, *6*, 17075.

(28) Bian, T.; Zhang, H.; Jiang, Y.; Jin, C.; Wu, J.; Yang, H.; Yang, D. Epitaxial Growth of Twinned Au−Pt Core−Shell Star-Shaped Decahedra as Highly Durable Electrocatalysts. *Nano Lett.* **2015**, *15*, 7808.

(29) Sharma, V.; Sinha, N.; Dutt, S.; Chawla, M.; Siril, P. F. Tuning the Surface Enhanced Raman Scattering and Catalytic Activities of Gold Nanorods by Controlled Coating of Platinum. *J. Colloid Interface Sci.* **2016**, *463*, 180.

(30) Straney, P. J.; Marbella, L. E.; Andolina, C. M.; Nuhfer, N. T.; Millstone, J. E. Decoupling Mechanisms of Platinum Deposition on Colloidal Gold Nanoparticle Substrates. *J. Am. Chem. Soc.* **2014**, *136*, 7873.

(31) Li, H.; Wu, H.; Zhai, Y.; Xu, X.; Jin, Y. Synthesis of Monodisperse Plasmonic Au Core−Pt Shell Concave Nanocubes with Superior Catalytic and Electrocatalytic Activity. *ACS Catal.* **2013**, *3*, 2045.

(32) Tan, L.; Li, L.; Peng, Y.; Guo, L. Synthesis of Au@ Pt Bimetallic Nanoparticles with Concave Au Nanocuboids as Seeds and their Enhanced Electrocatalytic Properties in the Ethanol Oxidation Reaction. *Nanotechnology* **2015**, *26*, 505401.

(33) Joplin, A.; Hosseini Jebeli, S. A.; Sung, E.; Diemler, N.; Straney, P. J.; Yorulmaz, M.; Chang, W.-S.; Millstone, J. E.; Link, S. Correlated Absorption and Scattering Spectroscopy of Individual Platinum Decorated Gold Nanorods Reveals Strong Excitation Enhancement in the Non-Plasmonic Metal. *ACS Nano* **2017**, *11*, 12346.

(34) Song, C.; Sun, Y.; Li, J.; Dong, C.; Zhang, J.; Jiang, X.; Wang, L. Silver-Mediated Temperature-Controlled Selective Deposition of Pt on Hexoctahedral Au Nanoparticles and the High Performance of Au@AgPt NPs in Catalysis and SERS. *Nanoscale* **2019**, *11*, 18881.

(35) Grzelczak, M.; Pérez-Juste, J.; Rodríguez-González, B.; LizMarzán, L. M. Influence of Silver Ions on the Growth Mode of Platinum on Gold Nanorods. *J. Mater. Chem.* **2006**, *16*, 3946.

(36) Jang, H.-J.; Hong, S.; Ham, S.; Shuford, K. L.; Park, S. Site Specific Growth of a Pt shell on Au Nanoplates: Tailoring their Surface Plasmonic Behavior. *Nanoscale* **2014**, *6*, 7339.

(37) Aslam, U.; Linic, S. Addressing Challenges and Scalability in the Synthesis of Thin Uniform Metal Shells on Large Metal Nanoparticle Cores: Case Study of Ag−Pt Core−Shell Nanocubes. *ACS Appl. Mater. Interfaces* **2017**, *9*, 43127.

(38) Straney, P. J.; Diemler, N. A.; Smith, A. M.; Eddinger, Z. E.; Gilliam, M. S.; Millstone, J. E. Ligand-Mediated Deposition of Noble Metals at Nanoparticle Plasmonic Hotspots. *Langmuir* **2018**, *34*, 1084.

(39) Guo, S.; Wang, L.; Wang, Y.; Fang, Y.; Wang, E. Bifunctional Au@ Pt Hybrid Nanorods. *J. Colloid Interface Sci.* **2007**, *315*, 363.

(40) Feng, L.; Wu, X.; Ren, L.; Xiang, Y.; He, W.; Zhang, K.; Zhou, W.; Xie, S. Well-Controlled Synthesis of Au@ Pt Nanostructures by Gold-Nanorod-Seeded Growth. *Chem.-Eur. J.* **2008**, *14*, 9764.

(41) Bao, Z. Y.; Lei, D. Y.; Jiang, R.; Liu, X.; Dai, J.; Wang, J.; Chan, H. L. W.; Tsang, Y. H. Bifunctional Au@Pt Core−Shell Nanostructures for In-Situ Monitoring of Catalytic Reactions by Surface-Enhanced Raman Scattering Spectroscopy. *Nanoscale* **2014**, *6*, 9063.

(42) Du, C.; Gao, X.; Zhuang, Z.; Cheng, C.; Zheng, F.; Li, X.; Chen, W. Epitaxial Growth of Zigzag PtAu Alloy Surface on Au Nanopentagrams with Enhanced Pt Utilization and Electrocatalytic Performance toward Ethanol Oxidation Reaction. *Electrochim. Acta* **2017**, *238*, 263.

(43) Zheng, Z.; Tachikawa, T.; Majima, T. Single-Particle Study of Pt-Modified Au Nanorods for Plasmon-Enhanced Hydrogen Generation in Visible to Near-Infrared Region. *J. Am. Chem. Soc.* **2014**, *136*, 6870.

(44) Rajendra, R.; Gangadharan, P. K.; Tripathi, S.; Kurungot, S.; Ballav, N. High-Index Faceted Au Nanocrystals with Highly Controllable Optical Properties and Electro-Catalytic Activity. *Nanoscale* **2016**, *8*, 19224.

(45) Rajendra, R.; Roy, D.; Tripathi, S.; Ballav, N. Facile Synthesis of Concave Cuboid Au NCs with Precisely Tunable Dimensions and Mechanistic Insight. *Langmuir* **2019**, *35*, 9456.

(46) Huang, Y.; Wu, L.; Chen, X.; Bai, P.; Kim, D.-H. Synthesis of Anisotropic Concave Gold Nanocuboids with Distinctive Plasmonic Properties. *Chem. Mater.* **2013**, *25*, 2470.

(47) Grzelczak, M.; Pérez-Juste, J.; García de Abajo, F. J.; Liz Marzán, L. M. Optical Properties of Platinum-Coated Gold Nanorods. *J. Phys. Chem. C* **2007**, *111*, 6183.

(48) Liu; Guyot-Sionnest, P. Synthesis and Optical Characterization of Au/Ag Core/Shell Nanorods. *J. Phys. Chem. B* **2004**, *108*, 5882.

(49) Orendorff, C. J.; Murphy, C. J. Quantitation of Metal Content in the Silver-Assisted Growth of Gold Nanorods. *J. Phys. Chem. B* **2006**, *110*, 3990.

(50) Fan, F.-R.; Liu, D.-Y.; Wu, Y.-F.; Duan, S.; Xie, Z.-X.; Jiang, Z.- Y.; Tian, Z.-Q. Epitaxial Growth of Heterogeneous Metal Nanocrystals: From Gold Nano-octahedra to Palladium and Silver Nanocubes. *J. Am. Chem. Soc.* **2008**, *130*, 6949.

(51) Jha, P. K.; Kashyap, V.; Gupta, K.; Kumar, V.; Debnath, A. K.; Roy, D.; Rana, S.; Kurungot, S.; Ballav, N. In-situ Generated Mn_3O_4- Reduced Graphene Oxide Nanocomposite for Oxygen Reduction Reaction and Isolated Reduced Graphene Oxide for Supercapacitor Applications. *Carbon* **2019**, *154*, 285.

(52) Gangadharan, P. K.; Pandikassala, A.; Kurungot, S. Toward pH Independent Oxygen Reduction Reaction by Polydopamine Derived 3D Interconnected, Iron Carbide Embedded Graphitic Carbon. *ACS Appl. Mater. Interfaces* **2021**, *13*, 8147.

(53) Wang, Y.; Wang, D.; Li, Y. A Fundamental Comprehension and Recent Progress in Advanced Pt-Based ORR Nanocatalysts. *SmartMat* **2021**, *2*, 56.

(54) Gowthaman, N. S. K.; Sinduja, B.; Shankar, S.; John, S. A. Displacement Reduction Routed Au−Pt Bimetallic Nanoparticles: A Highly Durable Electrocatalyst for Methanol Oxidation and Oxygen Reduction. *Sustain. Energy Fuels* **2018**, *2*, 1588.

(55) Ge, X.; Sumboja, A.; Wuu, D.; An, T.; Li, B.; Goh, F. W. T.; Hor, T. S. A.; Zong, Y.; Liu, Z. Oxygen Reduction in Alkaline Media: From Mechanisms to Recent Advances of Catalysts. *ACS Catal.* **2015**, *5*, 4643

Gold Nano-Earbuds: Seed-Mediated Synthesis and the Emergence of Three Plasmonic Peaks

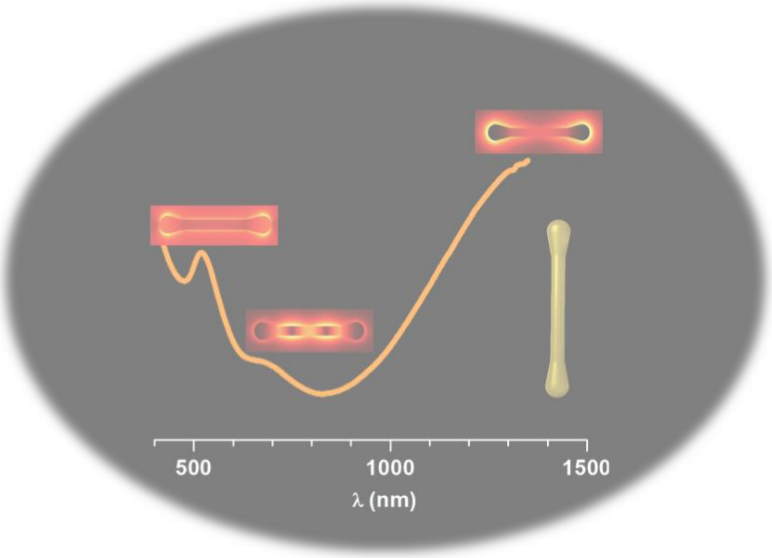

5.1 Introduction

Recent years have witnessed a surge in the interest in shape-specific noble metal nanostructures for various applications.[1] Particular attention has been placed on anisotropic Au nanostructures because of the ability to tailor their electronic, optoelectronic, optical, and plasmonic properties.[2-4] Of the myriad kinds of anisotropic Au nanostructures, 1D nanostructures are of fundamental interest and are promising for practical applications.[5-8] 1D nanostructures refer to those structures having one of the three dimensions (1 to 100 nm) greater than the other two,[9] usually characterized by two surface plasmon resonance (SPR) peaks arising because of the short and long axes of these systems.[10] Among the various 1D nanostructures, Au nanorods (NRs) remain the most investigated and studied because of their well-defined shape anisotropy giving rise to aspect ratio (AR)-dependent and widely tunable LSPR.[11] Substantial efforts have been put forward in recent times to develop synthetic protocols to extend the tunability of their LSPR into the near-infrared (NIR) regime emphasizing their applicability in biological imaging among a host of other applications. These synthetic protocols were marred by either tedious multistep processes,[12,13] long reaction duration,[14,15] or low yield,[16,17] apart from the inability to maintain the dimension under 100 nm for the Au NRs to be useful for biological imaging.[18]

In this Letter, we introduce a new morphology to the existing library of anisotropic 1D Au nanostructures, Au nano-earbud (NEB), by employing a binary surfactant mixture of CTAC and BDAC and using tannic acid (TA) as a mild reducing agent. These as-synthesized Au NEBs (widths, 4-6 nm; lengths, 37-77 nm) were reasonably monodisperse, structurally uniform, and single-crystalline with high ARs resulting in broadly tunable plasmon resonance peaks (LSPR tuned beyond 1200 nm). The role of the key chemical parameters has also been studied to investigate the growth and formation of this unique morphology. Additionally, the Au NEBs exhibit three distinct plasmonic peaks, rather uncommon for 1D nanostructures, attributed to the bulbous ends as well as the high AR of the structure from theoretical calculations solving Maxwell's equations with the finite element method.

5.2 Materials/Method

Gold(III) chloride trihydrate ($HAuCl_4.3H_2O$), silver nitrate ($AgNO_3$), cetyltrimethylammonium bromide (CTAB), cetyltrimethylammonium chloride (CTAC),

benzyldimethylhexadecylammonium chloride (BDAC), tannic acid (TA), and sodium borohydride ($NaBH_4$) were purchased from Sigma-Aldrich. Sodium hydroxide (NaOH; analytical reagent) was bought from Rankem. All chemicals were used as such. Milli-Q water (18.2 MΩ·cm) was used for all experiments.

Synthesis. A typical synthesis of Au NEBs is as follows: rapid addition of $NaBH_4$ (45 µL, 20 mM) to a mixture of Milli-Q water (0.5 mL), CTAB (0.625 mL, 0.2 M) and $HAuCl_4$ (78 µL, 4 mM) resulted in a brownish colour solution, which indicated the formation of seeds. The growth solution was made by sequential addition of water (0.630 mL), NaOH (20 µL, 0.1 M), $HAuCl_4$ (0.25 mL, 4 mM), CTAC (750 µL, 0.2 M), BDAC (250 µL, 0.2 M) and $AgNO_3$ (50 µL, 4 mM). The subsequent introduction of TA (10 µL, 100 mM) turned the colour of the solution from yellow to pale brownish-yellow in 10 min due to Au (III) → Au (I) reduction. Finally, to the growth solution, seed solution (varying from 5-500 µL) was added and the Au NEBs were allowed to grow for 2 h at room temperature.

To study the effect of $AgNO_3$, the amount was varied from 0-200 µL keeping the amount of seed at 50 µL and all other parameters same. When the amount of $HAuCl_4$ was modulated from 50-400 µL, other precursor quantities were kept unchanged. While varying the surfactant ratio, the total volume of the surfactant was always maintained at 1 mL with various ratios of the binary surfactants and keeping the other parameters constant.

Characterization. UV-vis spectra were recorded from g SHIMADZU UV- 3600 plus UV-VIS-NIR spectrophotometer. FE-SEM images were captured through ZEISS Ultra Plus and TEM images were captured using a JEOL JEM-2200FS transmission electron. microscope. The average length, width and aspect ratios of NEBs of varying sizes were determined using ImageJ software.

Modeling Method. A single Au NEB is considered in our modeling, and the scattering problem of the Au NEB was solved with the 3D finite element method using the Wave optics module of COMSOL Multiphysics 5.3. In the simulation, Au is chosen as "Au (Johnson)" from the COMSOL material library, in which the wavelength-dependent refractive index of Au is given. The investigated Au NEB is embedded in water with a refractive index of 1.33. The length of the Au NEB is 54 nm, and the central diameter is 4.5 nm, which are extracted from the average of 50 NEBs (L = 54.3 ± 9.1 nm; W = 4.6 ± 0.6 nm). More details about the

dimensions of the simulated Au NEB can be found in the insets of corresponding figures. The incident light wave travels along the z direction with both x and y components or only x (y) component electric fields. Perfectly matched layers are used in the modeling to absorb the outgoing wave energy radiation. The scattered field formulation was also used. The spectrum of scattering and absorption cross-sections for the Au NEB can be calculated with the model. Specifically, the scattering cross-section was calculated by integrating the outgoing Poynting vector over the closed surface of the Au NEB, and then divided by the incident intensity. For absorption cross-section was computed by integrating the power loss density in the Au NEB over its volume and divided by the incident intensity. With the obtained scattering and absorption cross-sections, we can get the extinction cross-section which is the sum of scattering and absorption cross-sections. In addition, the charge density distributions at resonant wavelength can also be obtained with the model. Similarly, the spectrum of extinction cross-section and the charge density distribution for Au cylindrical nanorod can also be obtained.

5.3 Results and Discussion

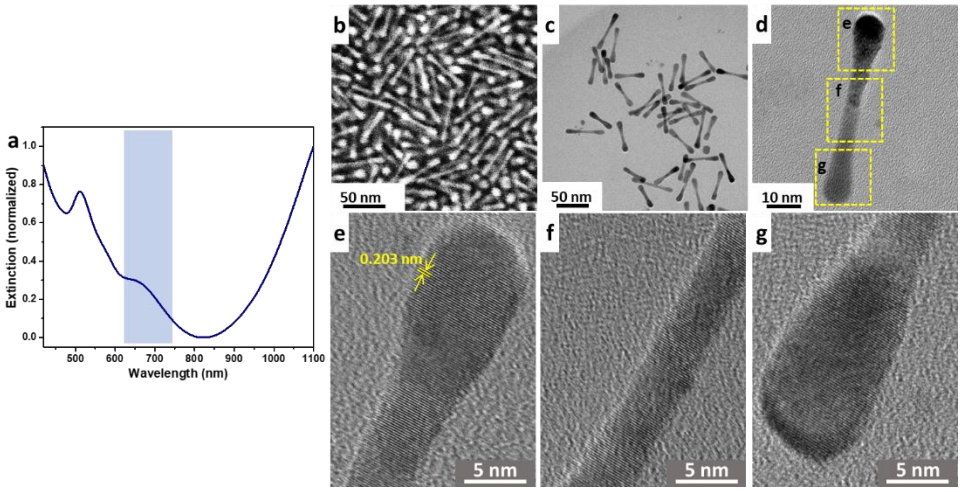

Figure 5.1: (a) UV-vis spectra; (b) FE-SEM image of Au NEB synthesized using 50 µL of seed. (c) Corresponding TEM image showing the monodispersity of the Au NEBs. (d) HR-TEM image of a single Au NEB with three regions boxed as e, f, and g. (e–g) HR-TEM images of the three regions (two bulbous ends and middle part) of Au NEB showing the single-crystalline nature throughout the morphology. Scale bar is 5 nm for all.

The as-synthesized Au NEBs were characterized by UV-vis spectroscopy which showed the appearance of three SPR peaks, two in the visible spectrum and the third in the NIR regime

(Figure 5.1a). Further, the field emission scanning electron microscopy (FE-SEM) images showed the dense presence of the NEB morphology (Figure 5.1b). These Au NEBs synthesized using seed amount of 50 μL (L = 54.3 ± 9.1 nm; W = 4.6 ± 0.6 nm) have been used as a representative model for all control experiments and were further characterized using transmission electron microscopy (TEM). Figure 5.1c shows the distribution of Au NEBs having uniform morphology with negligible spherical impurity. The TEM image of a single Au NEB (Figure 5.1d) and zoomed in high-resolution TEM images taken from the three regions (two bulbous ends and middle part) of Au NEB were found to be highly crystalline throughout with no observable stacking faults and/or twin defects (Figure 5.1e-g).

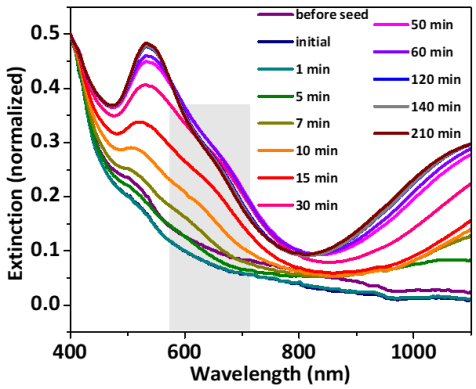

Figure 5.2: UV-vis spectra showing the evolution of Au NEB with time. The emergence of new peak has been highlighted in grey.

The growth progress of Au NEBs was monitored in real time using UV-vis spectroscopy (Figure 5.2). At 5 min into the reaction, the spectra revealed the appearance of three bands that were reasonably resolved though weak in intensity. The first band, typically referred to as transverse SPR (TSPR), was initially observed at ~510 nm and gradually red-shifted over the course of the reaction to finally stagnate at ~530 nm. The LSPR on the other hand underwent an initial red-shift (until 30 min) followed by a gradual blue-shift (subsequent 90 min). Similar behaviour was observed earlier in the case of Au NRs, implying that the seed particles had broken the symmetry to achieve the initially highest AR followed by its decrease.[21] The third band which came to existence at ~610 nm, red-shifted over time to finally culminate at ~640 nm. After 120 min, the completion of the reaction was indicated by the saturation of spectral intensity.

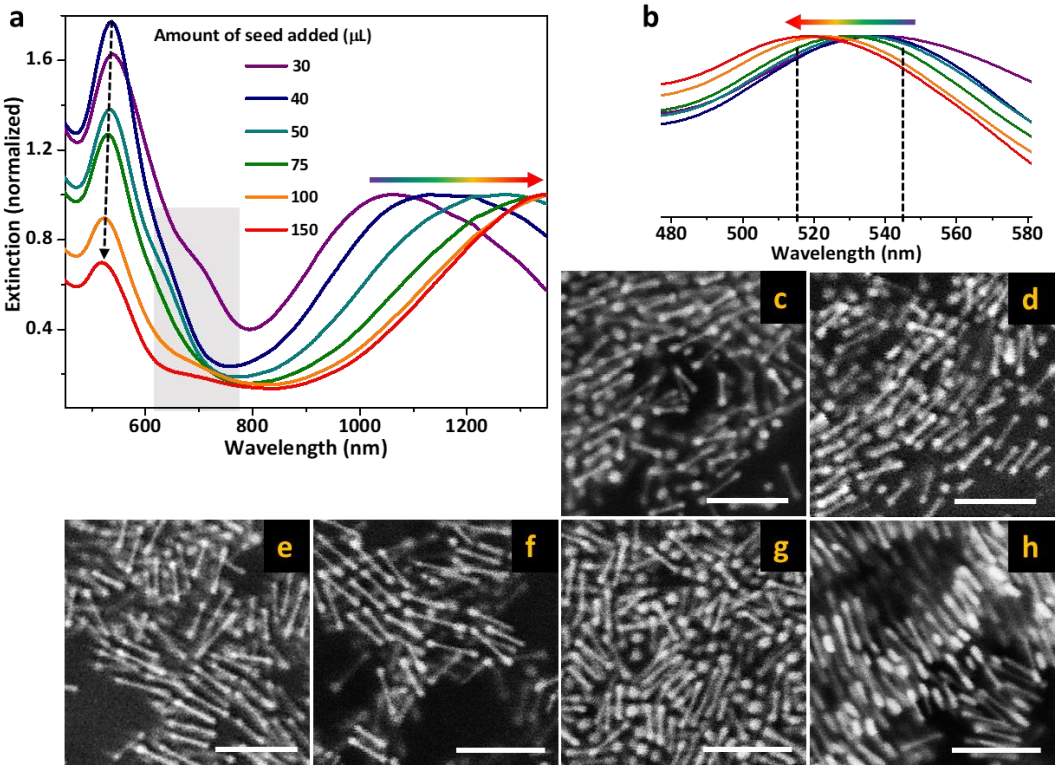

Figure 5.3: (a) UV−vis spectra of Au NEBs synthesized with varying amounts of seed as 30−200 μL. (b) Zoomed in UV−vis spectra of the transverse plasmon resonance showing the blue shift as the seed amount was varied from 30 to 150 μL. (c−h) Corresponding FE-SEM images of Au NEB synthesized by varying the amounts of seed as 30 (AR ≈ 10), 40 (AR ≈ 12), 50 (AR ≈ 14), 75 (AR ≈ 15), 100 (AR ≈ 16), and 150 μL (AR ≈ 17), respectively. Scale bar is 100 nm.

Because the amount of seed is known to play an important role in tuning the dimension of Au nanocrystals,[19,20] various amounts of seed ranging from 5 to 500 μL were added in the growth solution. Increasing the amount of seed added in the growth solution from 5 to 200 μL resulted in a gradual and remarkable red-shift of ~500 nm (from ~850 nm to ~1350 nm) (Figures 5.3a and 5.4a, e). It has been noticed for the seed-mediated growth of Au NCs that although reducing the amount of seed particles is often known to result in increased length and width of Au NCs,[16,19,20] irregular dumbbell-shaped structures dominated when the syntheses were carried out with seed volumes less than 30 μL (Figure 5.4b-d). On progressively increasing the seed amount from 30 to 150 μL, NEB-like structures with increasing length from ~49 to ~70 nm and gradual thinning of the bulbous ends (Figure 5.3c-h), reflected in the blue shift of ~20 nm (from ~538 to ~518 nm), were observed (Figure 5.3b). The AR simultaneously increased from 10 to 17. Because the LSPR features depend not only on the length of the nanostructure but

also on the AR (length/width), such a huge red-shift could be attributed to an exceptionally high AR pushing the LSPR to the NIR region (Figure 5.3a).

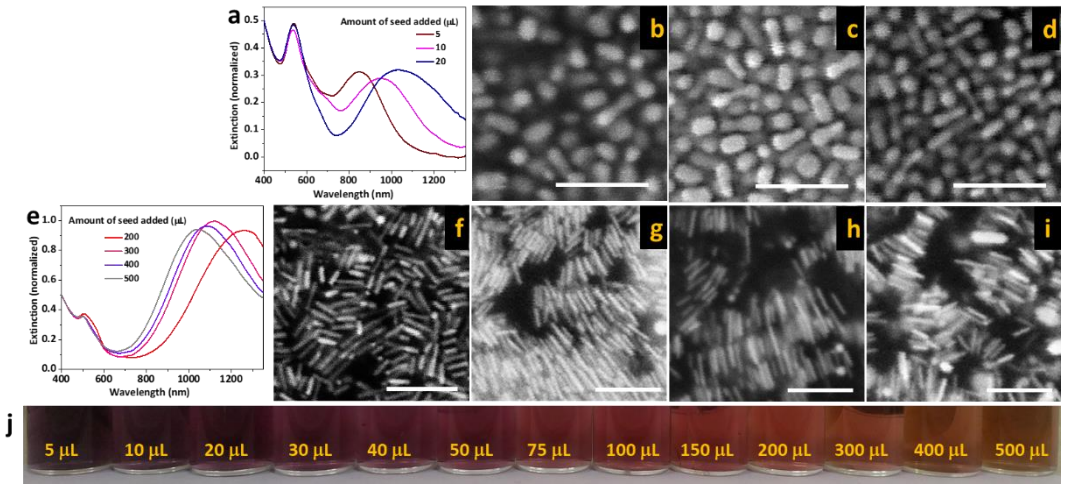

Figure 5.4: (a) UV-vis spectra obtained at a lower seed amount (5-20 μL); (b-d) Corresponding FE-SEM images of the samples synthesized with 5, 10 and 20 μL seed respectively; (e) UV-vis spectra obtained at a higher seed amount (200-500 μL); (f-i) Corresponding FE-SEM images of the samples synthesized with 200, 300, 400 and 500 μL seed. (j) Optical image of the solutions obtained by varying the amount of seed from 5-500 μL Scale bar is 100 nm for all.

A subsequent blue-shift of ~350 nm along with a change in the plasmon band features was observed as the seed amount was further increased from 200 to 500 μL because of the formation of Au NRs having lower AR as well as decreased length (Figure 5.4f-i). The UV-vis spectra (Figure 5.4e) corroborated well with the FE-SEM images. The transverse surface plasmon resonance (TSPR) band underwent a minute yet non-negligible change in the form of a blue-shift as the amount of seed was increased from 5 to 500 μL. The third plasmon peak at ~640 nm (highlighted in gray) gained intensity as well as underwent a red-shift as the amount of seed was increased from 5 to 100 μL (Figures 5.3a and 5.4a). Upon further increasing the amount of seed, the peak intensity gradually decreased and finally disappeared, resembling spectral features of Au NR with two plasmonic bands (Figure 5.4e). Thus, a moderate seed amount (30-200 μL) was desirable for obtaining a decent yield of Au NEBs.

To check the influence of the concentration of $HAuCl_4$ on the formation of Au NEBs, a set of experiments were carried out where the amount of $HAuCl_4$ was varied from 50 to 400 μL and monitored by analysing the FE-SEM and TEM images as well as UV-vis spectra (Figure 5.5).

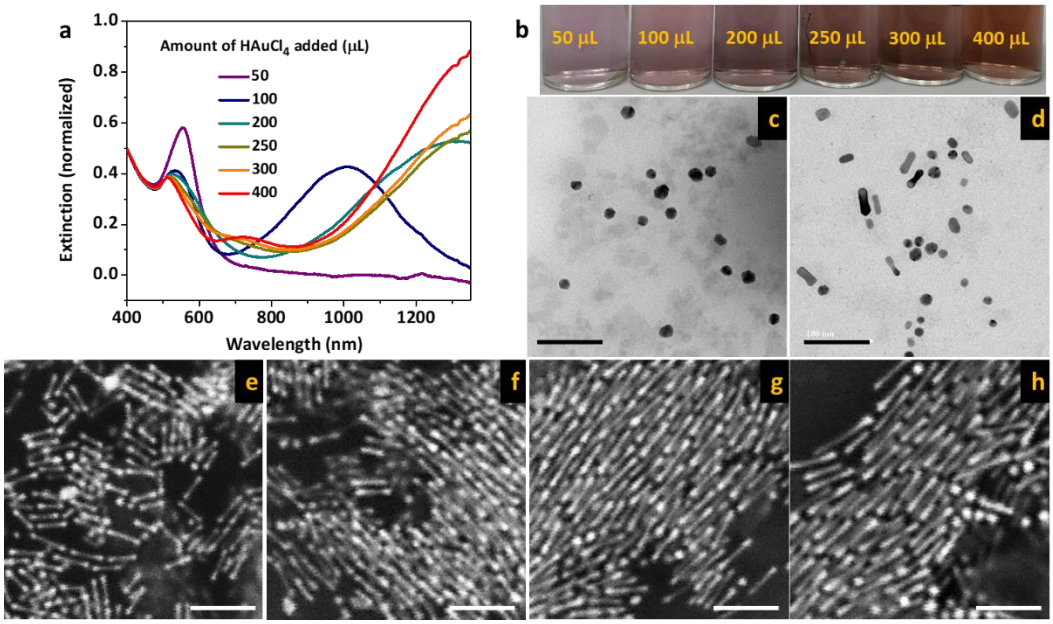

Figure 5.5: (a) UV-vis spectra recorded for NEB Au NCs synthesized with varying the amount of $HAuCl_4$ as 50, 100, 200, 250, 300, and 400 µL at 50 µL seed; (b) Corresponding optical image; TEM images (c-d) and FE-SEM images (e-h) of Au NCs synthesized using 50, 100, 200, 250, 300 and 400 µL $HAuCl_4$ respectively. Scale bar is 100 nm for all.

The control solution containing 50 µL (4 mM) of $HAuCl_4$ showed one SPR peak at ~550 nm (Figure 5.5a), matching well with the corresponding TEM image showing the presence of spherical particles only (Figure 5.5c). With the addition of more $HAuCl_4$ (100 µL), two prominent SPR peaks appeared evidenced from the TEM image by the formation of a rodlike morphology along with the presence of spherical particles (Figure 5.5a, d). Upon further increasing the amount of $HAuCl_4$ (200 µL), three SPR peaks came into the picture which gained more prominence at even higher amounts of $HAuCl_4$ (250-400 µL) (Figure 5.5a). This was corroborated by the FE-SEM images, which showed the formation of Au NEBs with increasing length and more prominent ends (Figure 5.5e-h). The higher amounts of $HAuCl_4$ were not only instrumental in increasing the length of the NEBs but also helped in tuning the ARs from ~13 to ~19, pointing toward an increased intensity and red-shift of the LSPR. This is impressive in the sense that pushing the LSPR spectra well into the NIR-II range could be achieved even by keeping the length below 100 nm. Previous studies have emphasized the critical size limit for nanoparticles is ~100 nm for them to be able to penetrate into tumors.[18] This makes our Au NEBs potential candidates for in vivo biological imaging. Because of the improved photothermal stability of smaller Au NRs (W = 8 ± 2 nm and L = 49 ± 8 nm) with respect to

the larger Au NRs (W = 18 ± 4 nm and L= 120 ± 17 nm), we anticipate that these Au NEBs will be useful for photothermal applications as well.[18]

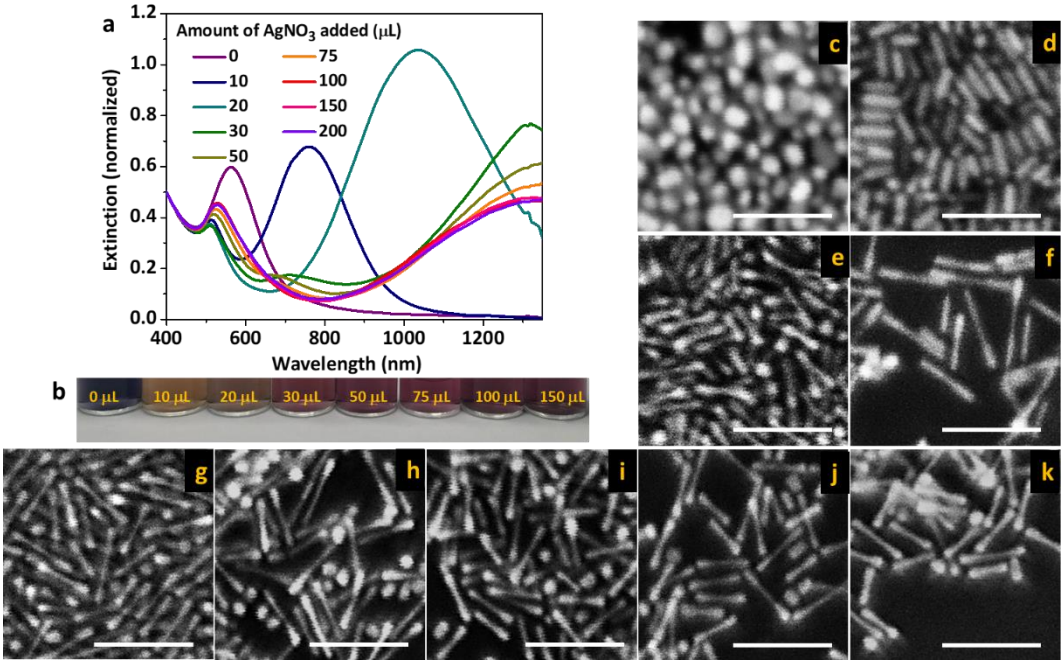

Figure 5.6: (a) UV−vis spectra recorded for NEB Au NCs synthesized with varying the amount of $AgNO_3$ as 0, 10, 20, 30, 50, 75, 100, 150, and 200 μL at 50 μL seed; (b) Corresponding optical image of the as synthesized solutions; (c−k) Corresponding FE−SEM images in the same order. Scale bar is 100 nm for all.

$AgNO_3$, which is known to control the AR of Au NRs by controlling the size at which the symmetry breaking event takes place,[22-25] was indeed observed to direct the morphology of our Au NEBs. The absence of $AgNO_3$ was clearly marked by the formation of spherical NPs, while a gradual increase of $AgNO_3$ (10 μL) resulted in Au NRs (Figure 5.6c, d). On further increasing the amount of $AgNO_3$ (20 μL), there was a noticeable red shift of the LSPR along with the appearance of a new peak centered ~650 nm (Figure 5.6a) in the UV-vis spectra which was consistent at even higher amounts of $AgNO_3$ (30-200 μL). These findings were supported by the FE-SEM images showing the uniform presence of Au NEBs. Drawing from the literature,[26,27] we propose that a high $HAuCl_4$:$AgNO_3$ (25:1) ratio although induces anisotropic growth, but are unable to passivate selective facets because of incomplete surface coverage of Ag leading to the formation of Au NRs. However, on lowering the ratio [$HAuCl_4$:$AgNO_3$ = 12.5:1], Ag selectively passivates the side facets thereby guiding the incoming Au atoms at the ends facilitating the formation of Au NEBs. At considerably high amounts of $AgNO_3$ (100-200

μL), there was a slight blue shift of the LSPR and reduced intensity of the peak ~650 nm. This observation is supported by the FE-SEM images of Au NEBs (Figure 5.6i-k) with decreasing length and thus lowered AR. That the role of the silver ion is not always to increase the ARs has been observed earlier in the case of Au NRs as well,[28] and a similar trend is reflected in the current study. Thus, it was found that apart from the amounts of $HAuCl_4$ and $AgNO_3$, the ratio of $HAuCl_4$:$AgNO_3$ also impacted the formation of Au NEBs.

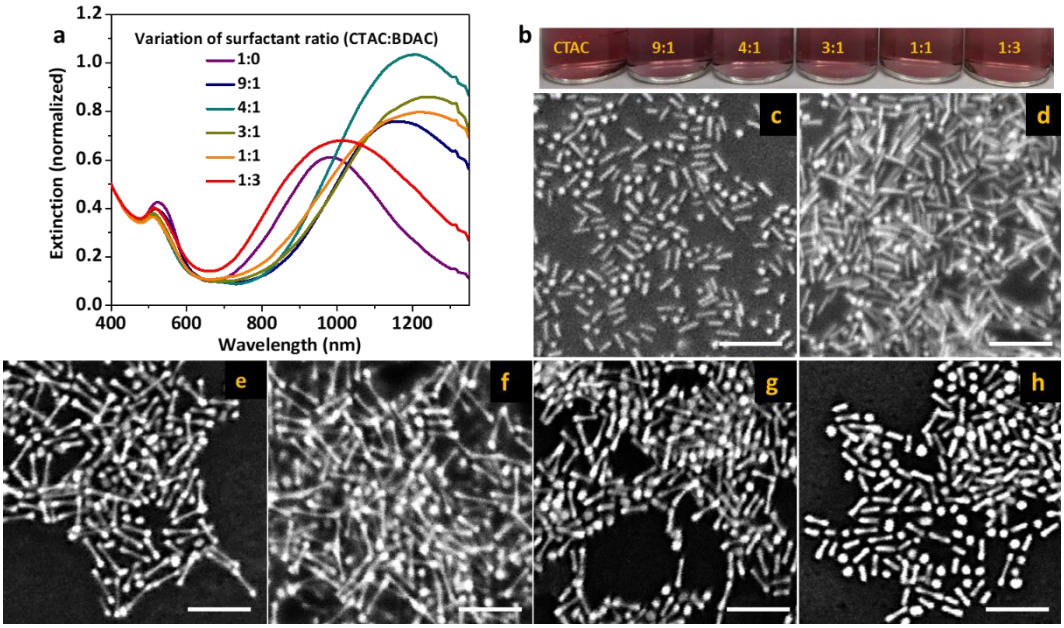

Figure 5.7: (a) UV-vis spectra recorded for NEB Au NCs synthesized by varying the ratio of CTAC:BDAC as 1:0, 9:1, 4:1, 3:1, 1:1, and 1:3 at 50 μL seed; (b) Optical images of the respective solutions; (c-h) Corresponding FE-SEM images in the same order. Scale bar is 100 nm for all.

Here, a binary surfactant mixture of CTAC and BDAC has been used to synthesize Au NEBs. When the synthesis was carried out in the presence of only CTAC, the product was a mixture of Au nanorods and nanospheres, whereas the synthesis in the presence of BDAC yielded nanospheres only. Upon replacing a small proportion of CTAC with an equal amount of BDAC into the growth solution (in a 9:1 ratio; the ratios indicate CTAC:BDAC henceforth), a marked red shift of the LSPR relative to only CTAC was observed. On further increasing the amount of BDAC in the binary surfactant mixture from 9:1 to 3:1, a further red-shift of the LSPR was observed. This initial red-shift (on varying the ratio of CTAC:BDAC from 9:1 to 3:1) was endorsed by the formation and an increase in the length of the Au NEBs with a constant lateral dimension of the middle region. On further increasing the proportion of BDAC to 1:1 and 1:3,

the blue shift of the LSPR corroborates the observation of shorter Au NEBs with thicker lateral dimensions.

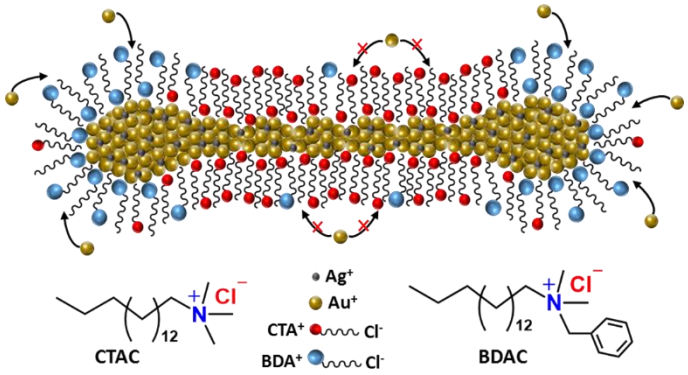

Scheme 5.1: Schematic representation of Au NEB formation in the presence of binary surfactants.

Based on these observations, we anticipate the presence of a larger number of CTAC monomers on the lateral facets of the seed with a tighter packing due to the smaller headgroup, thereby restricting the transverse growth. The BDAC monomers with their bulky polar headgroup[28,29] and larger headgroup surface area cannot enforce a tight packing, thus enabling the deposition of the Au^0 atoms at the much less protected ends[30] giving rise to the NEB structure (Scheme 5.1). However, the increased proportion of BDAC in the binary surfactant mixture leads to the considerable presence of BDAC on the lateral facets along with CTAC. It is thus unable to restrict the lateral growth and facilitate the unidirectional growth, leading to shorter NEBs with thicker widths. In the present study, the optimal ratio of CTAC:BDAC was maintained at 3:1. At this particular ratio of the binary surfactants, the LSPR displayed the maximum red-shift, although the formation of Au NEBs had started taking place even at a 1:1 ratio (Figure 5.7). This can also be understood from the formation of NRs at higher seed amounts. Contrary to conventional wisdom where CTAC alone does not promote the formation of Au NRs[31] and BDAC has been utilized in conjunction with CTAB only to result in higher AR Au NRs,[28] the formation of Au NRs in a chloride bound growth solution is another highlight of the present study (Figure 5.4f-i). While CTAB has been ubiquitously used in seed-mediated growth for the synthesis of single crystalline Au NRs,[16,28] introduction of a small amount of bromide ions into the growth solution from the seed solution in the form of CTAB does not aid the formation of Au NEBs. In fact, when deliberately added to the growth solution, they were found to impede the formation of Au NEBs (Figure 5.8).

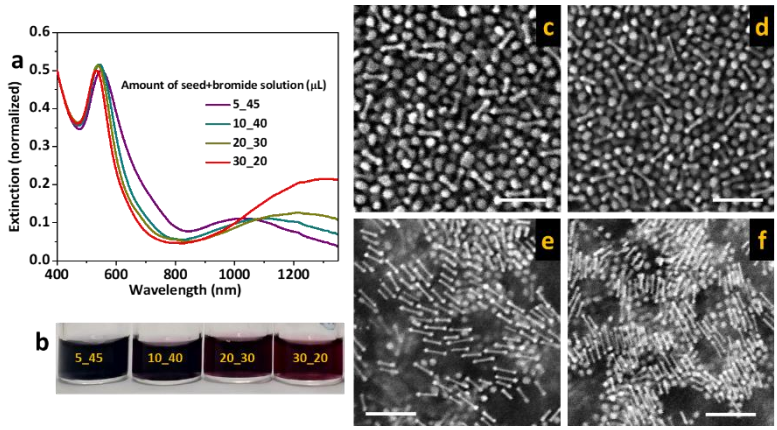

Figure 5.8: (a) UV−vis spectra recorded for NEB Au NCs synthesized with varying the amount of seed solution as 5, 10, 20 and 30 µL along with bromide solutions of 45, 40, 30, 20 µL respectively, to maintain the entire seed volume at 50 µL; (b) Corresponding optical image of the as-synthesized solutions; (c−f) Corresponding FE−SEM images in the same order. Scale bar is 100 nm for all.

After demonstrating the superiority of TA over ascorbic acid (AA) as a milder reducing agent for the synthesis of various anisotropic Au nanocrystals,[19,20] we have extended the potency of TA to synthesize Au NEBs in this work. Because the modulation of the concentration of the reducing agent in the growth solution offers a direct way to manipulate the reaction kinetics and thus the particle shape,[32] the amount of TA added to the growth solution was varied from 2 to 30 µL while keeping all other parameters fixed. At very low amounts of TA (2 µL), the shape yield of NEBs was very low. Increasing the amount from 5 to 10 µL resulted in the red shift of the LSPR accompanied by an increase in dimensions. Further increase of TA (15−30 µL) resulted in the gradual blue shift of LSPR and smaller NEBs accompanied by an increase of spherical particles. In all these cases, however, earbud-like morphology was maintained (Figure 5.9). This points to the fact that increasing the amount of TA in the growth solution results in an increase in the rate of gold ion reduction and thus a preference for the growth of kinetically more favourable spherical particles.

A theoretical study was implemented to understand the nature and origin of the three plasmonic peaks of Au NEBs. On the basis of the synthesized Au NEBs (L = 54.3 ± 9.1 nm; W = 4.6 ± 0.6 nm), we built a simulated NEB structure (AR = 12) with dimensions L = 54 nm and W = 4.5 nm (Figure 5.10, inset). The width of the NEB bulbous ends takes 8.5 nm. The investigated Au NEB is embedded in water with a refractive index of 1.33. The spectrum of extinction cross-section for an Au NEB was calculated by solving Maxwell's equations with the 3D finite

element method (see Materials/Methods for details). When the incident light travels along the z direction with an electric field consisting of both x and y components, the Au NEB with an AR of 12 exhibits three peaks (514, 700, and 1689 nm) in the simulated extinction spectrum, as shown in Figure 5.10a. The extinction spectrum for electric field with only y component (x component) is shown in Figure 5.10b (Figure 5.10c). It is found that the peak at 514 nm originates from the y component electric field. The electric near-field amplitude distribution for the peak 514 nm is shown in Figure 5.10d, which clearly indicates a transverse mode (i.e., TSPR peak). The peaks at 700 and 1689 nm, as shown in Figure 5.10d, are related to the x component electric field (i.e., LSPR peaks). The electric field amplitude distribution at 1689 and 700 nm shows that the LSPR peaks are dipole and sextupole mode, respectively. It is known that Au nanospheres exhibit a single plasmon resonance band in the visible regime at about 520 nm,[33,34] while it splits into two bands for Au NRs, TSPR at short wavelength, and LSPR at longer wavelength.[33-36] The position of the TSPR peak of the Au nanorod is roughly the same as that of the Au nanosphere and slightly depends on the AR.[37,38] For the LSPR, its position is very sensitive to the AR.[28,36,38-41] The synthesized NEB can be considered as a nanorod with flared ends.

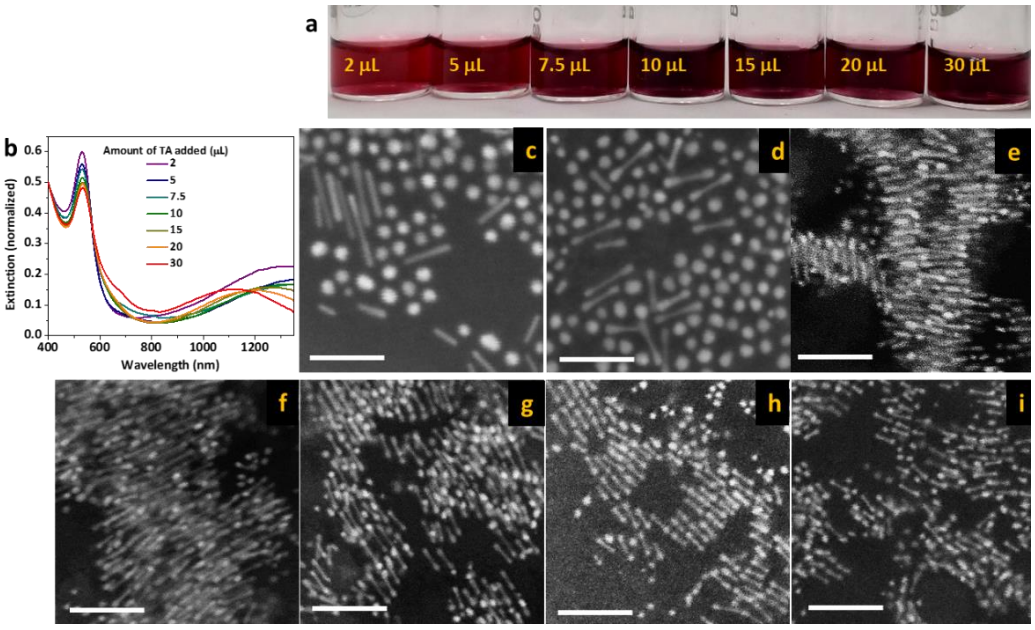

Figure 5.9: (a) Optical image of NEB Au NCs synthesized with varying the amount of TA as 2, 5, 7.5, 10, 15, 20 and 30 µL at 50 µL seed; (b) Corresponding UV−vis spectra recorded for the as-synthesized solutions; (c−i) Corresponding FE−SEM images in the same order. Scale bar is 100 nm for all.

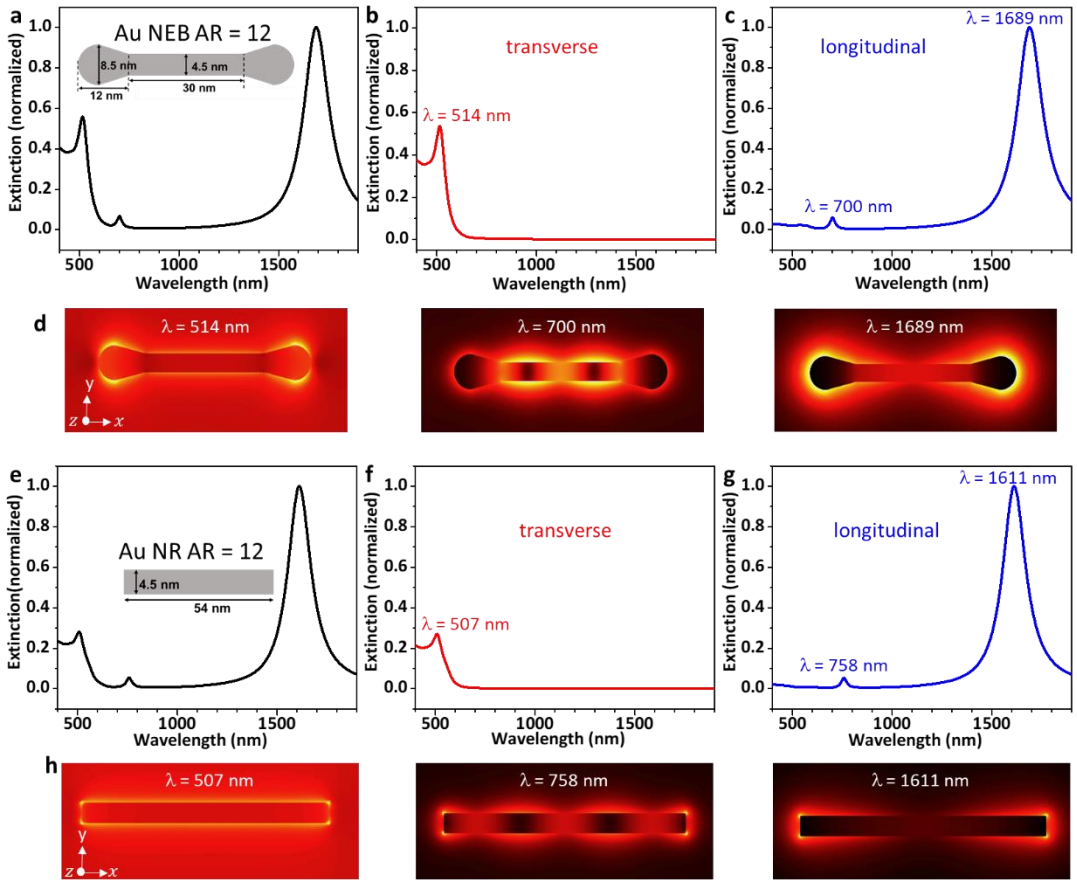

Figure 5.10: NEB and NR with AR = 12. Simulated extinction spectra of a Au NEB for an incident light wave with an electric field consisting of (a) both x and y components, (b) only y component, and (c) only x component; (d) The electric field amplitude distribution corresponding to the three plasmonic peaks. Simulated extinction spectra of an Au NR (AR = 12) for an incident light wave with an electric field consisting of (e) both x and y components; (f) only y component; and (g) only x component; (h) The electric field amplitude distribution corresponding to the three plasmonic peaks. The dimensions of the simulated Au nanoparticles are shown in the insets.

To understand the additional LSPR peak of the Au NEB, the extinction spectrum of cylindrical Au NR with AR = 12 was calculated as a comparison. In the simulation, the cylindrical Au NR has the same dimensions (L = 54 nm, W = 4.5 nm) as those of the Au NEB. It is found that both the Au nanoparticles possess a TSPR peak at the roughly same position: 514 nm for the Au NEB and 507 nm for Au NR (Figure 5.10f). The Au NR with AR = 12 also exhibits two LSPR peaks (758 and 1611 nm) (Figure 5.10g), similar to the Au NEB with AR = 12. Thus, the presence of the additional LSPR of Au NEB could also be induced by the high AR (12) of the synthesized Au NEB. In an earlier work, a hand-to-hand experiment-theory

complementarity showed the appearance of higher-order multipole resonances for NRs with ARs > 4.[42] One report attributed the presence of shape impurity to the manifestation of peaks between the TSPR and LSPR.[43] Other experimental observations on Au NRs with high ARs have not assigned the peaks, creating an ambiguity on the origin of such peaks,[14,15] and in fact, extinction spectra of Au NRs with high ARs and having similar widths like our Au NEBs did not reveal the third peak.[15] The observation of additional bands at higher aspect ratios for Au NRs and bipyramids have been attributed to higher-order plasmon modes.[27] Liz-Marzan and co-workers have demonstrated a robust control over the morphology resulting in AgAuAg bimetallic nanowire with ARs > 100 exhibiting nine distinguishable plasmonic peaks.[44] However, the present work focuses on a monometallic 1D nanostructure having high ARs (7-19) and exhibiting three plasmonic peaks.

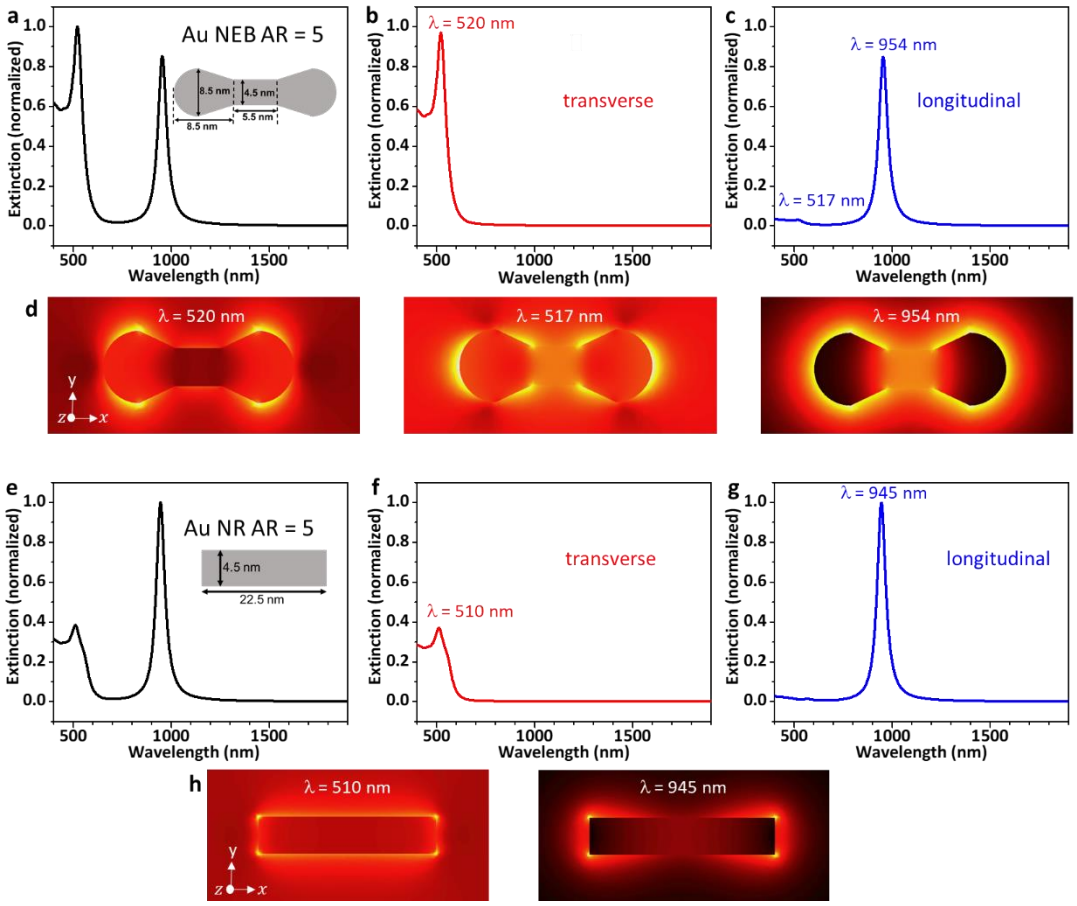

Figure 5.11: NEB and NR with AR = 5. Simulated extinction spectra of the Au NEB for an incident light wave with an electric field consisting of (a) both x and y components, (b) only y component, and (c) only x component. (d) The electric field amplitude distribution corresponding to the plasmonic peaks for the Au NR. Simulated extinction spectra of the Au NR for an incident light wave with an electric

field consisting of (e) both x and y components, (f) only y component, and (g) only x component. (h) The electric field amplitude distribution corresponding to the plasmonic peaks for the Au NR. The dimensions of the simulated Au nanoparticles are shown in the insets.

The LSPR of Au NR is known to depend on the rod shapes, for example, cylindrical, dumbbell, and dog-bone.[38,45-48] Theoretical calculations with the discrete dipole approximation (DDA) method has demonstrated that the Au NR with dog-bone shape exhibits a third peak in the extinction spectrum while only two peaks exist for the cylinder-shaped Au NR.[38] Thus, the special shape of the synthesized Au NEB, nanorod with flared ends, could be another cause of the appearance of the third plasmonic peak in the extinction spectrum in Figure 5.10a. As such, the NEB and NR with smaller AR (AR = 5) are investigated. The extinction spectra of the Au NEB (L = 22.5 nm, W = 4.5 nm, bulbous ends 8.5 nm) and cylindrical Au NR (L = 22.5 nm, W = 4.5 nm) are shown in Figure 5.11. It is shown that with a smaller AR, the Au NEB still exhibits two LSPR peaks: 517 and 954 nm (Figure 5.11c). In contrast, only one LSPR peak at 945 nm was obtained for the Au NR with AR = 5 (Figure 5.11g). Therefore, the bulbous ends of the Au NEB indeed contribute to the existence of three plasmonic peaks, intensified by the high ARs. The theoretical analysis thus not only points at the appearance of the new plasmonic peak to the bulbous ends of Au NEB but also provides conclusive evidence that the synthesized morphology is indeed a new class of morphology.

Difference between Au nano-earbud and Au nano-dumbbell: Here we clarify the major differences between our Au nano-earbud (NEB) and Au nano-dumbbell (ND) reported previously.

Shape. Although at first glance both look similar, the distinctive feature between them is the separation between the bulbous ends. The separation between the bulbous ends for Au NEBs is roughly half the entire length of the structure whereas that of Au NDs is one third of the total length.[49-51] Additionally, the lateral dimension of the middle region for Au NEB does not exceed 7 nm.

Synthesis method. Apart from the different experimental parameters, Au NEBs have been synthesized using CTAB mediated Au nanospheres seeds while wet chemical syntheses of Au NDs pertain to post modifications on Au NR seeds. Thus, several precursor parameters could be played with to further tune the dimensions of Au NEBs and achieve an aspect ratio ~19

(length x width in the middle: 76.9 ± 8.8 nm x 3.9 ± 0.6 nm) while the AR of NDs was found to be ~4 (length x width in the middle: 87.0 ± 5.9 nm x 20.4 ± 2.0 nm).[52]

Optical property. The Au NDs do not exhibit 3 plasmon bands like Au NEBs. The transverse peak observed in our work is much more intense than the transverse peak observed in either Au NRs or Au NDs. Although, it was shown that the transverse peak was quite intense, it was attributed to a thicker lateral dimension;[51] however, in our work the lateral dimension is ~5 nm, too small to bring about such an intense TSPR. Another report on experimental STEM-EELS on Au nano-dumbbells (NDs) with BEM simulations identified three plasmons as two longitudinal modes, one dipolar and one quadrupolar and a third mode of transverse dipolar character, which the authors claimed is hardly measured experimentally.[53] In the present study, we have observed three peaks both experimentally as well as through simulated theoretical studies and the observed third new peak is a sextupole of longitudinal character.

Further from our theoretical simulations it has been shown that even when the aspect ratio is small (AR = 5), Au NEBs still exhibit 3 plasmon peaks.

5.4 Summary and Conclusions

In conclusion, we have demonstrated a new synthetic protocol to generate a novel 1D nanostructure, Au NEB, with reasonable monodispersity, high crystallinity, and tunable Ars (from 7 to 19). More importantly, Au NEBs with widely tunable LSPR can be synthesized using a binary surfactant mixture of CTAC and BDAC in the classical seed-mediated growth method. Among the various precursor parameters investigated to study the influence in generating Au NEBs, apart from the binary mixtures of CTAC and BDAC which guided the NEB structure, $HAuCl_4$ was found to display the most important role as it could simultaneously tune the length as well as the AR (from 13 to 19). Notably, we have tuned the LSPR beyond 1200 nm while retaining the dimension in the sub-100 nm regime. In addition, this new morphology exhibits three plasmonic peaks, rather unusual for 1D Au nanostructure, with theoretical studies attributing the new resonance peak as a higher-order longitudinal mode, arising because of the bulbous ends of the NEB structure and intensified by the high AR. These sub-100 nm Au NEBs with LSPR in the NIR-II window are ideal for studies as contrast agents for biomedical imaging where the choices are limited.

5.5 References

(1) Grzelczak, M.; Perez-Juste, J.; Mulvaney, P.; Liz-Marzan, L. M. Shape Control in Gold Nanoparticle Synthesis. *Chem. Soc. Rev.* **2008**, *37*, 1783.

(2) Eustis, S.; El-Sayed, M. A. Why Gold Nanoparticles are More Precious than Pretty Gold: Noble Metal Surface Plasmon Resonance and its Enhancement of the Radiative and Nonradiative Properties of Nanocrystals of Different Shapes. *Chem. Soc. Rev.* **2006**, *35*, 209.

(3) Dreaden, E. C.; Alkilany, A. M.; Huang, X.; Murphy, C. J.; El Sayed, M. A. The Golden Age: Gold Nanoparticles for Biomedicine. *Chem. Soc. Rev.* **2012**, *41*, 2740.

(4) Reguera, J.; Langer, J.; Jimenez de Aberasturi, D.; Liz-Marza´ n, L.´ M. Anisotropic Metal Nanoparticles for Surface Enhanced Raman Scattering. *Chem. Soc. Rev.* **2017**, *46*, 3866.

(5) Xia, Y.; Yang, P.; Sun, Y.; Wu, Y.; Mayers, B.; Gates, B.; Yin, Y.; Kim, F.; Yan, H. One-Dimensional Nanostructures: Synthesis, Characterization, and Applications. *Adv. Mater.* **2003**, *15*, 353.

(6) Murphy, C. J.; Gole, A. M.; Hunyadi, S. E.; Orendorff, C. J. One Dimensional Colloidal Gold and Silver Nanostructures. *Inorg. Chem.* **2006**, *45*, 7544.

(7) Sau, T. K.; Rogach, A. L. Nonspherical Noble Metal Nanoparticles: Colloid-Chemical Synthesis and Morphology Control. *Adv. Mater.* **2010**, *22*, 1781.

(8) Wu, Z.; Yang, S.; Wu, W. Shape Control of Inorganic Nanoparticles from Solution. *Nanoscale* **2016**, *8*, 1237.

(9) Huo, D.; Kim, M. J.; Lyu, Z.; Shi, Y.; Wiley, B. J.; Xia, Y. One Dimensional Metal Nanostructures: From Colloidal Syntheses to Applications. *Chem. Rev.* **2019**, *119*, 8972.

(10) Chen, Y.; Somsen, C.; Milenkovic, S.; Hassel, A. W. Fabrication of Single Crystalline Gold Nanobelts. *J. Mater. Chem.* **2009**, *19*, 924.

(11) Chen, H.; Shao, L.; Li, Q.; Wang, J. Gold Nanorods and their Plasmonic Properties. *Chem. Soc. Rev.* **2013**, *42*, 2679.

(12) Wu, H.-Y.; Chu, H.-C.; Kuo, T.-J.; Kuo, C.-L.; Huang, M. H. Seed-Mediated Synthesis of High Aspect Ratio Gold Nanorods with Nitric Acid. *Chem. Mater.* **2005**, *17*, 6447.

(13) Khanal, B. P.; Zubarev, E. R. Purification of High Aspect Ratio Gold Nanorods: Complete Removal of Platelets. *J. Am. Chem. Soc.* **2008**, *130*, 12634.

(14) Xu, X.; Zhao, Y.; Xue, X.; Huo, S.; Chen, F.; Zou, G.; Liang, X.- J. Seedless Synthesis of High Aspect Ratio Gold Nanorods with High Yield. *J. Mater. Chem. A* **2014**, *2*, 3528.

(15) Chang, H.-H.; Murphy, C. J. Mini Gold Nanorods with Tunable Plasmonic Peaks beyond 1000 nm. *Chem. Mater.* **2018**, *30*, 1427.

(16) Jana, N. R.; Gearheart, L.; Murphy, C. J. Wet Chemical Synthesis of High Aspect Ratio Cylindrical Gold Nanorods. *J. Phys. Chem. B* **2001**, *105*, 4065.

(17) Altansukh, B.; Yao, J.; Wang, D. Synthesis and Characterization of Gold Nanorods by a Seeding Growth Method. *J. Nanosci. Nanotechnol.* **2009**, *9*, 1300.

(18) Chen, Y. S.; Zhao, Y.; Yoon, S. J.; Gambhir, S. S.; Emelianov, S. Miniature Gold Nanorods for Photoacoustic Molecular Imaging in the Second Near-Infrared Optical Window. *Nat. Nanotechnol.* **2019**, *14*, 465.

(19) Rajendra, R.; Gangadharan, P. K.; Tripathi, S.; Kurungot, S.; Ballav, N. High-Index Faceted Au Nanocrystals with Highly Controllable Optical Properties and Electro-Catalytic Activity. *Nanoscale* **2016**, *8*, 19224.

(20) Rajendra, R.; Roy, D.; Tripathi, S.; Ballav, N. Facile Synthesis of Concave Cuboid Au NCs with Precisely Tunable Dimensions and Mechanistic Insight. *Langmuir* **2019**, *35*, 9456.

(21) Park, K.; Drummy, L. F.; Wadams, R. C.; Koerner, H.; Nepal, D.; Fabris, L.; Vaia, R. A. Growth Mechanism of Gold Nanorods. *Chem. Mater.* **2013**, *25*, 555.

(22) Liu, M.; Guyot-Sionnest, P. Mechanism of Silver(I)-Assisted Growth of Gold Nanorods and Bipyramids. *J. Phys. Chem. B* **2005**, *109*, 22192.

(23) Personick, M. L.; Langille, M. R.; Zhang, J.; Mirkin, C. A. Shape Control of Gold Nanoparticles by Silver Underpotential Deposition. *Nano Lett.* **2011**, *11*, 3394.

(24) Almora-Barrios, N.; Novell-Leruth, G.; Whiting, P.; Liz Marzan, L. M.; Lo´ pez, N. Theoretical Description of the Role of´ Halides, Silver, and Surfactants on the Structure of Gold Nanorods. *Nano Lett.* **2014**, *14*, 871.

(25) Walsh, M. J.; Barrow, S. J.; Tong, W.; Funston, A. M.; Etheridge, J. Symmetry Breaking and Silver in Gold Nanorod Growth. *ACS Nano* **2015**, *9*, 715.

(26) Personick, M. L.; Mirkin, C. A. Making Sense of the Mayhem behind Shape Control in the Synthesis of Gold Nanoparticles. *J. Am. Chem. Soc.* **2013**, *135*, 18238.

(27) Zhang, Q.; Jing, H.; Li, G. G.; Lin, Y.; Blom, D. A.; Wang, H. Intertwining Roles of Silver Ions, Surfactants, and Reducing Agents in Gold Nanorod Overgrowth: Pathway Switch between Silver Underpotential Deposition and Gold−Silver Codeposition. *Chem. Mater.* **2016**, *28*, 2728.

(28) Nikoobakht, B.; El-Sayed, M. A. Preparation and Growth Mechanism of Gold Nanorods (NRs) Using Seed-Mediated Growth Method. *Chem. Mater.* **2003**, *15*, 1957.

(29) Wadams, R. C.; Fabris, L.; Vaia, R. A.; Park, K. Time Dependent Susceptibility of the Growth of Gold Nanorods to the Addition of a Cosurfactant. *Chem. Mater.* **2013**, *25*, 4772.

(30) Lee, J.-H.; Gibson, K. J.; Chen, G.; Weizmann, Y. Bipyramid Templated Synthesis of Monodisperse Anisotropic Gold Nanocrystals. *Nat. Commun.* **2015**, *6*, 7571.

(31) Perez-Juste, J.; Liz-Marzan, L. M.; Carnie, S.; Chan, D. Y. C.;́ Mulvaney, P. Electric-Field-Directed Growth of Gold Nanorods in Aqueous Surfactant Solutions. *Adv. Funct. Mater.* **2004**, *14*, 571.

(32) Langille, M. R.; Personick, M. L.; Zhang, J.; Mirkin, C. A. Defining Rules for the Shape Evolution of Gold Nanoparticles. *J. Am. Chem. Soc.* **2012**, *134*, 14542.

(33) Link, S.; El-Sayed, M. A. Spectral Properties and Relaxation Dynamics of Surface Plasmon Electronic Oscillations in Gold and Silver Nanodots and Nanorods. *J. Phys. Chem. B* **1999**, *103*, 8410.

(34) Link, S.; Mohamed, M. B.; El-Sayed, M. A. Simulation of the Optical Absorption Spectra of Gold Nanorods as a Function of Their Aspect Ratio and the Effect of the Medium Dielectric Constant. *J. Phys. Chem. B* **1999**, *103*, 3073.

(35) van der Zande, B. M. I.; Böhmer, M. R.; Fokkink, L. G. J.; Schönenberger, C. Aqueous Gold Sols of Rod-Shaped Particles. *J. Phys. Chem. B* **1997**, *101*, 852.

(36) Yu; Chang, S.-S.; Lee, C.-L.; Wang, C. R. C. Gold Nanorods: Electrochemical Synthesis and Optical Properties. *J. Phys. Chem. B* **1997**, *101*, 6661.

(37) Zhu, J.; Huang, L.; Zhao, J.; Wang, Y.; Zhao, Y.; Hao, L.; Lu, Y. Shape Dependent Resonance Light Scattering Properties of Gold Nanorods. *Mater. Sci. Eng., B* **2005**, *121*, 199.

(38) Xu, X.; Cortie, M. B. Shape Change and Color Gamut in Gold Nanorods, Dumbbells, and Dog Bones. *Adv. Funct. Mater.* **2006**, *16*, 2170.

(39) Brioude, A.; Jiang, X. C.; Pileni, M. P. Optical Properties of Gold Nanorods: DDA Simulations Supported by Experiments. *J. Phys. Chem. B* **2005**, *109*, 13138.

(40) Ni, W.; Kou, X.; Yang, Z.; Wang, J. Tailoring Longitudinal Surface Plasmon Wavelengths, Scattering and Absorption Cross Sections of Gold Nanorods. *ACS Nano* **2008**, *2*, 677.

(41) Ye, X.; Jin, L.; Caglayan, H.; Chen, J.; Xing, G.; Zheng, C.; Doan-Nguyen, V.; Kang, Y.; Engheta, N.; Kagan, C. R.; Murray, C. B. Improved Size-Tunable Synthesis of Monodisperse Gold Nanorods through the Use of Aromatic Additives. *ACS Nano* **2012**, *6*, 2804.

(42) Payne, E. K.; Shuford, K. L.; Park, S.; Schatz, G. C.; Mirkin, C. A. Multipole Plasmon Resonances in Gold Nanorods. *J. Phys. Chem. B* **2006**, *110*, 2150.

(43) Vigderman, L.; Zubarev, E. R. High-Yield Synthesis of Gold Nanorods with Longitudinal SPR Peak Greater than 1200 nm Using Hydroquinone as a Reducing Agent. *Chem. Mater.* **2013**, *25*, 1450.

(44) Mayer, M.; Scarabelli, L.; March, K.; Altantzis, T.; Tebbe, M.; Kociak, M.; Bals, S.; García de Abajo, F. J.; Fery, A.; Liz-Marzan, L. M.́ Controlled Living Nanowire Growth: Precise Control over the Morphology and Optical Properties of AgAuAg Bimetallic Nanowires. *Nano Lett.* **2015**, *15*, 5427.

(45) Gou, L.; Murphy, C. J. Fine-Tuning the Shape of Gold Nanorods. *Chem. Mater.* **2005**, *17*, 3668.

(46) Song, J. H.; Kim, F.; Kim, D.; Yang, P. Crystal Overgrowth on Gold Nanorods: Tuning the Shape, Facet, Aspect Ratio, and Composition of the Nanorods. *Chem. - Eur. J.* **2005**, *11*, 910.

(47) Wang, C.; Wang, T.; Ma, Z.; Su, Z. pH-tuned Synthesis of Gold Nanostructures from Gold Nanorods with Different Aspect Ratios. *Nanotechnology* **2005**, *16*, 2555.

(48) Zweifel, D. A.; Wei, A. Sulfide-Arrested Growth of Gold Nanorods. *Chem. Mater.* **2005**, *17*, 4256.

(49) Wang, C.; Wang, T.; Ma, Z.; Su, Z. pH-tuned Synthesis of Gold Nanostructures from Gold Nanorods with Different Aspect Ratios. *Nanotechnology* **2005**, *16*, 2555.

(50) Grzelczak, M.; Sánchez-Iglesias, A.; Rodríguez-González, B.; Alvarez-Puebla, R.; Pérez Juste, J.; Liz-Marzán, L. M. Influence of Iodide Ions on the Growth of Gold Nanorods: Tuning Tip Curvature and Surface Plasmon Resonance. *Adv. Func. Mater.* **2008**, *18*, 3780.

(51) Wang, P.; Liu, M.; Gao, G.; Zhang, S.; Shi, H.; Li, Z.; Zhang, L.; Fang, Y. From Gold Nanorods to Nanodumbbells: A Different Way to Tailor Surface Plasmon Resonances by a Chemical Route. *J. Mater. Chem.* **2012**, *22*, 24006.

(52) Grzelczak, M.; Sánchez-Iglesias, A.; Mezerji, H. H.; Bals, S.; Pérez-Juste, J.; Liz-Marzán, L. M. Steric Hindrance Induces crosslike Self-Assembly of Gold Nanodumbbells. *Nano Lett.* **2012**, *12*, 4380.

(53) Rodríguez-González, B.; Attouchi, F.; Cardinal, M. F.; Myroshnychenko, V.; Stéphan, O.; García de Abajo, F. J.; Liz-Marzán, L. M.; Kociak, M. Surface Plasmon Mapping of Dumbbell Shaped Gold Nanorods: The Effect of Silver Coating. *Langmuir* **2012**, *28*, 9063.

ACS Publications
Most Trusted. Most Cited. Most Read.

Facile Synthesis of Concave Cuboid Au NCs with Precisely Tunable Dimensions and Mechanistic Insight

Author: Ranguwar Rajendra, Debashree Roy, Shalini Tripathi, et al

Publication: Langmuir
Publisher: American Chemical Society
Date: Jul 1, 2019

PERMISSION/LICENSE IS GRANTED FOR YOUR ORDER AT NO CHARGE

This type of permission/license, instead of the standard Terms and Conditions, is sent to you because no fee is being charged for your order. Please note the following:

- Permission is granted for your request in both print and electronic formats, and translations.
- If figures and/or tables were requested, they may be adapted or used in part.
- Please print this page for your records and send a copy of it to your publisher/graduate school.
- Appropriate credit for the requested material should be given as follows: "Reprinted (adapted) with permission from {COMPLETE REFERENCE CITATION}. Copyright {YEAR} American Chemical Society." Insert appropriate information in place of the capitalized words.
- One-time permission is granted only for the use specified in your RightsLink request. No additional uses are granted (such as derivative works or other editions). For any uses, please submit a new request.

If credit is given to another source for the material you requested from RightsLink, permission must be obtained from that source.

BACK CLOSE WINDOW

Controlling the Aspect Ratios of Au Nanocrystals with Ag Addition Time in Seed-Mediated Synthesis: Implications for Surface-Enhanced Raman Scattering

Author: Debashree Roy, Ranguwar Rajendra, Shalini Tripathi, et al

Publication: ACS Applied Nano Materials

Publisher: American Chemical Society

Date: Jul 1, 2021

PERMISSION/LICENSE IS GRANTED FOR YOUR ORDER AT NO CHARGE

This type of permission/license, instead of the standard Terms and Conditions, is sent to you because no fee is being charged for your order. Please note the following:

- Permission is granted for your request in both print and electronic formats, and translations.
- If figures and/or tables were requested, they may be adapted or used in part.
- Please print this page for your records and send a copy of it to your publisher/graduate school.
- Appropriate credit for the requested material should be given as follows: "Reprinted (adapted) with permission from {COMPLETE REFERENCE CITATION}. Copyright {YEAR} American Chemical Society." Insert appropriate information in place of the capitalized words.
- One-time permission is granted only for the use specified in your RightsLink request. No additional uses are granted (such as derivative works or other editions). For any uses, please submit a new request.

If credit is given to another source for the material you requested from RightsLink, permission must be obtained from that source.

BACK CLOSE WINDOW

Seed-Mediated Growth of Pt on High-Index Faceted Au Nanocrystals: The Ag Lining and Implications for Electrocatalysis

Author: Debashree Roy, Ranguwar Rajendra, Pranav K. Gangadharan, et al

Publication: ACS Applied Nano Materials

Publisher: American Chemical Society

Date: Sep 1, 2021

PERMISSION/LICENSE IS GRANTED FOR YOUR ORDER AT NO CHARGE

This type of permission/license, instead of the standard Terms and Conditions, is sent to you because no fee is being charged for your order. Please note the following:

- Permission is granted for your request in both print and electronic formats, and translations.
- If figures and/or tables were requested, they may be adapted or used in part.
- Please print this page for your records and send a copy of it to your publisher/graduate school.
- Appropriate credit for the requested material should be given as follows: "Reprinted (adapted) with permission from {COMPLETE REFERENCE CITATION}. Copyright {YEAR} American Chemical Society." Insert appropriate information in place of the capitalized words.
- One-time permission is granted only for the use specified in your RightsLink request. No additional uses are granted (such as derivative works or other editions). For any uses, please submit a new request.

If credit is given to another source for the material you requested from RightsLink, permission must be obtained from that source.

BACK CLOSE WINDOW

Gold Nanoearbuds: Seed-Mediated Synthesis and the Emergence of Three Plasmonic Peaks

Author: Debashree Roy, Yi Xu, Ranguwar Rajendra, et al

Publication: Journal of Physical Chemistry Letters

Publisher: American Chemical Society

Date: May 1, 2020

PERMISSION/LICENSE IS GRANTED FOR YOUR ORDER AT NO CHARGE

This type of permission/license, instead of the standard Terms and Conditions, is sent to you because no fee is being charged for your order. Please note the following:

- Permission is granted for your request in both print and electronic formats, and translations.
- If figures and/or tables were requested, they may be adapted or used in part.
- Please print this page for your records and send a copy of it to your publisher/graduate school.
- Appropriate credit for the requested material should be given as follows: "Reprinted (adapted) with permission from {COMPLETE REFERENCE CITATION}. Copyright {YEAR} American Chemical Society." Insert appropriate information in place of the capitalized words.
- One-time permission is granted only for the use specified in your RightsLink request. No additional uses are granted (such as derivative works or other editions). For any uses, please submit a new request.

If credit is given to another source for the material you requested from RightsLink, permission must be obtained from that source.

BACK CLOSE WINDOW